ISSN 2518-1726 (Online),
ISSN 1991-346X (Print)

ҚАЗАҚСТАН РЕСПУБЛИКАСЫ
ҰЛТТЫҚ ҒЫЛЫМ АКАДЕМИЯСЫНЫҢ

ӘЛЬ-ФАРАБИ АТЫНДАҒЫ
ҚАЗАҚ ҰЛТТЫҚ УНИВЕРСИТЕТІНІҢ

Х А Б А Р Л А Р Ы

ИЗВЕСТИЯ

НАЦИОНАЛЬНОЙ АКАДЕМИИ НАУК
РЕСПУБЛИКИ КАЗАХСТАН

КАЗАХСКИЙ НАЦИОНАЛЬНЫЙ
УНИВЕРСИТЕТ ИМЕНИ АЛЬ-ФАРАБИ

N E W S

OF THE NATIONAL ACADEMY OF SCIENCES
OF THE REPUBLIC OF KAZAKHSTAN

AL-FARABI KAZAKH
NATIONAL UNIVERSITY

ФИЗИКА-МАТЕМАТИКА СЕРИЯСЫ
♦
СЕРИЯ ФИЗИКО-МАТЕМАТИЧЕСКАЯ
♦
PHYSICO-MATHEMATICAL SERIES

4 (320)

ШІЛДЕ – ТАМЫЗ 2018 ж.
ИЮЛЬ – АВГУСТ 2018 г.
JULY-AUGUST 2018

1963 ЖЫЛДЫҢ ҚАҢТАР АЙЫНАН ШЫҒА БАСТАҒАН
ИЗДАЕТСЯ С ЯНВАРЯ 1963 ГОДА
PUBLISHED SINCE JANUARY 1963

ЖЫЛЫНА 6 РЕТ ШЫҒАДЫ
ВЫХОДИТ 6 РАЗ В ГОД
PUBLISHED 6 TIMES A YEAR

АЛМАТЫ, ҚР ҰҒА АЛМАТЫ, НАН РК ALMATY, NAS RK

«ҚР ҰҒА Хабарлары. Физика-математикалық сериясы».

ISSN 2518-1726 (Online), ISSN 1991-346X (Print)

Меншіктенуші: «Қазақстан Республикасының Ұлттық ғылым академиясы» РҚБ (Алматы қ.)
Қазақстан республикасының Мәдениет пен ақпарат министрлігінің Ақпарат және мұрағат комитетінде 01.06.2006 ж. берілген **№5543-Ж** мерзімдік басылым тіркеуіне қойылу туралы куәлік

Мерзімділігі: жылына 6 рет.
Тиражы: 300 дана.

Редакцияның мекенжайы: 050010, Алматы қ., Шевченко көш., 28, 219 бөл., 220, тел.: 272-13-19, 272-13-18,
www:nauka-nanrk.kz / physics-mathematics.kz

Типографияның мекенжайы: «Аруна» ЖК, Алматы қ., Муратбаева көш., 75.

«Известия НАН РК. Серия физико-математическая».

ISSN 2518-1726 (Online), ISSN 1991-346X (Print)

Собственник: РОО «Национальная академия наук Республики Казахстан» (г. Алматы)
Свидетельство о постановке на учет периодического печатного издания в Комитете информации и архивов Министерства культуры и информации Республики Казахстан **№5543-Ж**, выданное 01.06.2006 г.

Периодичность: 6 раз в год.
Тираж: 300 экземпляров.

Адрес редакции: 050010, г. Алматы, ул. Шевченко, 28, ком. 219, 220, тел.: 272-13-19, 272-13-18,
www:nauka-nanrk.kz / physics-mathematics.kz

Адрес типографии: ИП «Аруна», г. Алматы, ул. Муратбаева, 75.

News of the National Academy of Sciences of the Republic of Kazakhstan. Physical-mathematical series.

ISSN 2518-1726 (Online), ISSN 1991-346X (Print)

Owner: RPA "National Academy of Sciences of the Republic of Kazakhstan" (Almaty)
The certificate of registration of a periodic printed publication in the Committee of information and archives of the Ministry of culture and information of the Republic of Kazakhstan N 5543-Ж, issued 01.06.2006

Periodicity: 6 times a year
Circulation: 300 copies

Editorial address: 28, Shevchenko str., of. 219, 220, Almaty, 050010, tel. 272-13-19, 272-13-18,
www:nauka-nanrk.kz / physics-mathematics.kz

Address of printing house: ST "Aruna", 75, Muratbayev str, Almaty

N E W S
OF THE NATIONAL ACADEMY OF SCIENCES OF THE REPUBLIC OF KAZAKHSTAN
PHYSICO-MATHEMATICAL SERIES
ISSN 1991-346X
Volume 4, Number 320 (2018), 5 – 14

UDC 517.927

N. Medeubaev[1] , S. Menlikozhaeva[2], A. Seitmuratov[2],
M. Ramazanov[1], B. Zharmenova[2] , T. Shamilov[3]

[1]The E.A. Buketov Karaganda State University, Karaganda;
[2]The Korkyt Ata Kyzylorda State University, Kyzylorda;
[3]Azerbaijan University of Architecture and Construction, Azerbaijan, Baku
medeubaev65@mail.ru, angisin_@mail.ru, saulesh_menli@mail.ru,
ramamur@mail.ru, 81_bota@mail.ru, invar59@mail.ru

AREA OF APPLICABILITY OF APPROXIMATE EQUATIONS OF VIBRATIONS OF ROD SYSTEMS OF VARIABLE THICKNESS

Abstract: The approximate equations of torsional vibrations of rod systems of variable thickness given in this work allow us to build approximate theories of oscillations depending on the conditions at the ends of the rod, the order of derivatives of the desired in the approximate equations and initial conditions. Approximate equations of oscillations of rod systems above the second order in derivatives of the desired function in the scientific literature are practically not found. On the other hand, approximate equations containing derivatives above the second order need to study the applicability of a theory based on various approximate equations. For simplicity, we consider the area of applicability for a constant radius rod, when the desired function U_θ or rotational displacement depends on the angular coordinate θ, i.e., we investigate the area of applicability of the approximate equations of oscillation based on the general equation of oscillation

Key words: torsional oscillations, rod, system, variable thickness, cylinder, shell, radius, Bessel function.

In the cylindrical coordinate system (r,θ,z) the spatial problem of torsional vibrations of the cylindrical shell is reduced to the solution of the equation

$$\rho M^{-1}\left(\frac{\partial^2\psi_1}{\partial t^2}\right)-\Delta\psi_1=0 \tag{15}$$

under boundary conditions on the inner and outer surface of the cylindrical shell

$$\sigma_{r\theta}+\frac{(-1)^{i+1}}{\Delta_{oi}}F_i^{'}(z)\sigma_{r\theta}=f_{ns_1}^{(i)} \qquad i=(1,2) \tag{16}$$

when $r=F_i(z)$, where $r=F_1(z)$ and $r=F_2(z)$ inner and outer shell radii, respectively, $\Delta_0=\sqrt{1+\left[F_i^{'}\right]^2}$.

Presenting ψ_1 in the form of potentials

$$\psi_1=\int_0^\infty \begin{matrix}\sin(kz)\\ -\cos(kz)\end{matrix}\Big\}dk\int_l\psi_{10}\exp(pt)dp \tag{17}$$

and substituting it into equations (15), we again obtain for ψ_{10} expression

$$\frac{d^2\psi_{10}}{dr^2}+\frac{1}{r}\frac{d\psi_{10}}{dr}-\beta^2\psi_{10}=0; \tag{18}$$

the general solution of which is

$$\psi_{10}=AI_0(\beta r)+BK_0(\beta r) \tag{19}$$

In this case, the integration constant of *B* as opposed to the task for the rod is different from zero.

If the shift displacement u_θ search in the offset u_θ

$$u_\theta=\int_0^\infty \begin{matrix}\sin(kz)\\ -\cos(kz)\end{matrix}\Big\}dk\int_{(l)}u_{\theta,0}\exp(pt)dp \tag{20}$$

then, the decomposing of Bessel's function I_0 and K_0 in a row, for $u_{\theta,0}^{(0)}$ we obtain expression

$$u_{\theta,0}^{(0)}=\frac{1}{r}A-\sum_{n=0}^{\infty}\beta_0^{2(n+1)}\left\{A-B\left[\ln\frac{\beta_0\xi}{2}-\frac{1}{2}\psi(n+1)-\right.\right.$$
$$\left.\left.-\frac{1}{2}\psi(n+2)\right]\right\}\frac{\left(\frac{r}{2}\right)^{2n+1}}{n!(n+1)!}; \tag{21}$$

where $\psi(n)$ - psy-function.

Introducing new values

$$\hat{U}_{\theta,0}=-\frac{1}{2}\beta_0^2\left\{A-B\left[\ln\frac{\beta_0\xi}{2}-\psi(1)-\frac{1}{2}\right]\right\}$$
$$\hat{U}_{\theta,1}=-\frac{A}{\xi} \tag{22}$$

and substituting their expression (21) instead of constants A, B we obtain expression

$$U_{\theta,0}^{(0)}=2\sum_{n=0}^{\infty}\frac{\left(\frac{r}{2}\right)^{2n+1}}{n!(n+1)!}\beta_0^{2n}\hat{U}_{\theta,0}+\xi\left\{\left[\frac{1}{r}+\sum_{n=0}^{\infty}\eta_{1,n}(r)\frac{\left(\frac{r}{2}\right)^{2n+1}}{n!(n+1)!}\beta_0^{2(n+1)}\right]\hat{U}_{\theta,1}\right\} \tag{23}$$

in reference to k and p, for shear displacement, we obtain the final representation

$$U_\theta(r,z,t)=2\sum_{n=0}^{\infty}\frac{\left(\frac{r}{2}\right)^{2n+1}}{n!(n+1)!}\lambda_0^{(n)}U_{\theta,0}+ \\ +\xi\left\{\frac{1}{r}+\sum_{n=0}^{\infty}\eta_{1,n}(r)\frac{\left(\frac{r}{2}\right)^{2n+1}}{n!(n+1)!}\lambda_0^{(n+1)}\right\}U_{\theta,1}; \tag{24}$$

where $U_{\theta,0};U_{\theta,1}$ have a obvious mechanical meaning, functions $\eta_{1,n}$ are equal

$$\eta_{1,n}(r)=\ln\frac{r}{\xi}+\frac{n}{2(n+1)}-\sum_{k=1}^{n}\frac{1}{k} \tag{25}$$

Similarly, for tension $\sigma_{r,\theta};\sigma_{z,\theta}$ we obtain expression

$$M^{-1}\sigma_{r,\theta}=2\sum_{n=0}^{\infty}\frac{\left(\frac{r}{2}\right)^{2n+1}}{n!(n+2)!}\lambda_2^{(n+1)}U_{\theta,1}+\frac{\xi}{2}\left\{\frac{1}{2}\lambda_2^{(1)}-\frac{4}{r^2}+\frac{1}{2}\sum_{n=0}^{\infty}\eta_{2,n}(r)\frac{\left(\frac{r}{2}\right)^{2(n+1)}}{n!(n+2)!}\lambda_2^{(n+2)}\right\}U_{\theta,1} \tag{26}$$

$$M^{-1}\sigma_{z,\theta}=2\sum_{n=0}^{\infty}\frac{\left(\frac{r}{2}\right)^{2n+1}}{n!(n+2)!}\lambda_2^{(n)}\frac{\partial U_{\theta,1}}{\partial z}+\xi\left\{\frac{1}{r}+\sum_{n=0}^{\infty}\eta_{1,n}(r)\frac{\left(\frac{r}{2}\right)^{2n+1}}{n!(n+2)!}\lambda_2^{(n)}\right\}\frac{\partial U_{\theta,1}}{\partial z}$$

where ξ intermediate surface, determined by the formula

$$\xi=\frac{\max\left[F_1(z)\right]}{2}\left\{\chi-\frac{\max\left[F_1(z)\right]}{\min\left[F_2(z)\right]}\right\} \tag{27}$$

herewith
$\max\left[F_1(z)\right]<\min\left[F_2(z)\right]$
coefficient χ satisfies the inequality

$$2+\frac{\max\left[F_1(z)\right]}{\min\left[F_2(z)\right]}\le\chi\le 2\frac{\min\left[F_2(z)\right]}{\max\left[F_1(z)\right]}+\frac{\max\left[F_1(z)\right]}{\min\left[F_2(z)\right]}$$

Substituting (25) into boundary conditions (16) to determine $U_{\theta,0}$ и $U_{\theta,1}$ we obtain a system of integro-differential equations, which is also the general equations of torsional vibrations of a circular cylindrical shell.

We present only a system of approximate equations of torsional vibration

$$F_i(z)\left[\frac{F_i(z)}{8}\lambda_2^{(1)} - F_i'(z)\frac{\partial}{\partial z}\right]U_{\theta,0} + \xi\left\{\frac{1}{2}\lambda_2^{(1)} - \frac{2}{F_i'} - \frac{F_i'(z)}{F_i(z)}\frac{\partial}{\partial z} + \right.$$
$$\left. + \frac{F_i(z)}{8}\lambda_2^{(1)}\left[\eta_{2,0}(F_i)\frac{F_i}{2}\lambda_2^{(1)} - \eta_{1,0}(F_i)\frac{F_i'(z)}{2}\right]\right\}\frac{\partial U_{\theta,1}}{\partial z} = \Delta_{0i}M^{-1}f_{ns_1}^{(i)} \qquad (i=1,2) \qquad (28)$$

Where

$$\eta_{1,0} = \ln\frac{r}{\xi}$$
$$\eta_{2,0}(r) = \ln\frac{r}{\xi} - \frac{1}{2}$$

For a shell of constant thickness with radii r_1 and r_2 accordingly, from (28) we obtain the system

$$\frac{r_i^2}{8}\lambda_2^{(1)}U_{\theta,0} + \xi\left\{\frac{1}{2}\lambda_2^{(1)} - \frac{2}{r_i^2} + \frac{r_i}{2}\lambda_2^{(1)}\left[\frac{\eta_{2,0}(r_i)r_i}{2}\right]\lambda_2^{(1)}\right\}$$
$$\frac{\partial U_{\theta,1}}{\partial z} = M^{-1}\left[f_\theta^{(i)}\right] \qquad (29)$$

The boundary conditions for the end of the shell under torsional vibration are derived as for the rod. We present only the boundary conditions at the end of the shell when $z = const$ there is a normal intensity beat $\sigma_{z\theta} = F(r,t)$. The boundary condition will have the form

$$u_{\theta,0} = M^{-1}\left[F(0,t)\right];$$
$$\frac{\partial u_{\theta,1}}{\partial z} = 0 \qquad (30)$$

General equations of longitudinal-radial oscillations of the cylindrical shell are derived as for the rod of variable radius.

For the formulation of various boundary value problems, we first give approximate equations of longitudinal-radial oscillations

$$\left\{C + \frac{r_i^2}{2}\left[\lambda_2^{(1)} + C\left(\lambda_1^{(1)} + 2\frac{\partial^2}{\partial z^2}\right)\right]\right\}U_{r,0} - \frac{\partial}{\partial z}\left\{(1-C) + \frac{r_i^2}{8}\left[2\lambda_2^{(1)} - C\left(\lambda_1^{(1)} + 2\frac{\partial^2}{\partial z^2}\right)\right]\right\}U_{z,0} -$$
$$- \xi\left\{-\frac{2}{r_i^2} + \left(\frac{1}{2} + D\ln\frac{r_i}{\xi}\right)\lambda_2^{(1)} + \left(\ln\frac{r_i}{\xi} - \frac{1}{4}\right)(1-D)\lambda_2^{(1)} + \right.$$

$$+ D\left(\lambda_1^{(1)} + 2\frac{\partial^2}{\partial z^2}\right)\ln\frac{r_i}{\xi} - D\left(\frac{3}{4}\lambda_1^{(1)} + \frac{\partial^2}{\partial z^2}\right)\frac{r_i^2}{16}\Bigg\}\lambda_2^{(1)}U_{r,1} +$$

$$+ \xi\left\{\frac{1}{2} + (1-D)\ln\frac{r_i}{\xi} + \frac{r_i^2}{8}\left[- D\left(\ln\frac{r_i}{\xi} - \frac{3}{4}\right)\lambda_1^{(1)} + D\left(\ln\frac{r_i}{\xi} - \frac{1}{4}\right)\lambda_2^{(1)} +\right.\right.$$

$$\left.\left. + \left(2\ln\frac{r_i}{\xi} - 1\right)\left(\lambda_2^{(1)} - D\frac{\partial^2}{\partial z^2}\right)\right]\right\}\frac{\partial U_{z,1}}{\partial z} = M^{-1}\left(f_r^{(i)}\right) \qquad (i = 1,2)$$

$$\left\{(1-C) + \frac{r_i^2}{8}\left[(1-C)\lambda_2^{(1)} - 2C\lambda_1^{(1)}\right]\right\}\frac{\partial U_{r,0}}{\partial z} +$$

$$+ \left\{(1+C)\lambda_1^{(1)} + \frac{r_i^2}{8}\lambda_1^{(1)}\left[(1+C)\lambda_2^{(1)} - 2C\frac{\partial^2}{\partial z^2}\right]\right\}U_{z,0} -$$

(31)

$$- \xi\left\{\frac{2}{r_i^2} + (1-D)\ln\frac{r_i}{\xi}\lambda_2^{(1)} + \frac{r_i^2}{8}\left(\ln\frac{r_i}{\xi} - \frac{3}{4}\right)\left[(1-D)\lambda_2^{(1)} - 2D\lambda_1^{(1)}\right]\lambda_2^{(1)}\right\}\times$$

$$\times\frac{\partial U_{r,1}}{\partial z} - \xi\left\{\frac{2}{r_i^2} + \left(\lambda_2^{(1)} - 2D\frac{\partial^2}{\partial z^2}\right)\ln\frac{r_i}{\xi} + \frac{r_i^2}{\xi}\left(\ln\frac{r_i}{\xi} - \frac{1}{2}\right)\times\right.$$

$$\left.\times\left[\left(\lambda_2^{(1)} - D\frac{\partial^2}{\partial z^2}\right)\lambda_2^{(1)} - 2D\lambda_1^{(1)}\frac{\partial^2}{\partial z^2}\right]\right\}U_{z,1} = \frac{2}{r_i^2}M^{-1}\left(f_{rz}^{(i)}\right), \qquad (i = 1,2)$$

where $f_r^{(i)}, f_{rz}^{(i)}$ the loads on the outer and inner surfaces of the shells u_r, u_z are approximately equal

$$u_z = U_{z,0} - \xi\left(\ln\frac{r}{\xi} + \frac{1}{2}\right)U_{z,1}$$

(32)

$$u_r = \frac{r}{2}U_{r,0} - \frac{r\xi}{2}\left[\frac{2}{r^2} + (1-D)\lambda_2^{(1)}\ln\frac{r}{\xi}\right]U_{r,1} + \frac{r\xi}{2}D\ln\frac{r}{\xi}\frac{\partial U_{z,1}}{\partial z}$$

tension

$$M^{-1}\sigma_{zz} = (1+C)\frac{\partial U_{z,0}}{\partial z} - (1-C)U_{r,0} - \xi\left(\frac{1}{2} + \ln\frac{r}{\xi}\right)\left[(1+2D)\frac{\partial U_{z,1}}{\partial z} - (1-2D)\lambda_2^{(1)}U_{r,1}\right] \quad (33)$$

$$M^{-1}\sigma_{r,z} = \frac{r}{2}\left\{(1-C)\frac{\partial U_{r,0}}{\partial z} + (1+C)\lambda_1^{(1)}U_{z,0} - \xi\left[\frac{2}{r^2} + (1-2D)\lambda_2^{(1)}\ln\frac{r}{\xi}\right]\frac{\partial U_{r,1}}{\partial z} -\right.$$

$$\left. - \xi\left[\frac{2}{r^2} + \left(\lambda_2^{(1)} - 2D\frac{\partial^2}{\partial z^2}\right)\ln\frac{r}{\xi}\right]U_{z,1}\right\};$$

$$M^{-1}\sigma_{r,r} = \left\{ CU_{r,0} - (1-C)\frac{\partial U_{z,0}}{\partial z} + \xi\left[\left(D\ln\frac{r}{\xi} - \frac{1}{2}\right)\lambda_2^{(1)} + \frac{2}{r^2}\right]U_{r,1} + \xi\left[(1-D)\ln\frac{r}{\xi} + \frac{1}{2}\right]\frac{\partial U_{z,1}}{\partial z}\right\};$$

$$M^{-1}\sigma_{\theta\theta} = \left\{ CU_{r,0} - (1-C)\frac{\partial U_{z,0}}{\partial z} + \frac{\xi}{2}\left[(1-D)\lambda_2^{(1)} + \frac{2}{r^2}\right]U_{r,1} + \xi\left[1-D+2\ln\frac{r}{\xi}\right]\frac{\partial U_{z,1}}{\partial z}\right\}$$

$$C = 1 - NM^{-1}; \qquad D = 1 - MN^{-1}$$

Here $U_{z,0}$ and $U_{r,1}$ moving intermediate surface points, $U_{z,1}$ and $U_{r,0}$ deformations of these points along the radial coordinate.

At the beginning we formulate three-dimensional boundary conditions for the shell end $z = const$.

Free or loaded by normal tension of the end

$$\sigma_{zz} = -F(t); \qquad \sigma_{rz} = 0 \tag{34}$$

Rigidly fixed end

$$u_r = u_z = 0 \tag{35}$$

Perfectly fixed end

$$u_z = 0; \qquad \sigma_{rz} = 0 \tag{36}$$

On the basis of the approximate expression (33) for tension conditions (34) for unknown U_{rj}, U_{zj} lead to boundary conditions

$$(1+C)\frac{\partial U_{z,0}}{\partial z} - (1-C)U_{r,0} - \frac{\xi}{2}(1+2C)\frac{\partial U_{z,1}}{\partial z} + \frac{\xi}{2}(1-2C)$$

$$\lambda_2^{(1)}U_{r,1} = -M^{-1}(F)(1-C)\frac{\partial U_{z,0}}{\partial z} + (1+C)\lambda_1^{(1)}U_{z,0} = 0$$

$$\frac{\partial U_{r,1}}{\partial z} + U_{z,1} = 0 \tag{37}$$

Similarly, conditions (35) and (36) lead to boundary conditions

$$U_{r,0} = U_{r,1} = 0; \qquad U_{r,0} = \frac{\xi}{2}U_{z,1} \tag{38}$$

And

$$U_{z,0} = \frac{\xi}{2}U_{z,1}; \qquad \frac{\partial U_{r,1}}{\partial z} + U_{z,1} = 0 \tag{39}$$

$$(1-C)\frac{\partial U_{r,0}}{\partial z} + (1-C)\lambda_1^{(1)}U_{z,0} = 0$$

Boundary conditions (37) - (39) differ from those available in the scientific literature, obtained on the basis of certain hypotheses and suggestions of mechanical and geometric nature, the presence of operators $\lambda_j^{(1)}$, reflecting the principle of D'alembert's mechanics.

Consider a more complex sealing of the end of the cylindrical shell.

Let the end of the cylindrical shell is in interaction with another deformable body. In particular, such a deformable body should be a plate-plate perpendicular to the axis of the shell.

We also consider two types of contact in a three-dimensional setting.

Rigid contact.

$$\begin{gathered} W_z^{(1)} = W_z^{(2)}; \qquad \overline{u}_r^{(1)} = u_r^{(2)}; \qquad \overline{u}_r^{(1)} = \frac{1}{\xi}\int_{r_1}^{r_2} u_r^{(1)} dr; \\ \sigma_{zz}^{(1)} = \sigma_{zz}^{(2)}; \qquad \overline{\sigma}_{rz}^{(1)} = \sigma_{rz}^{(2)}; \qquad \overline{\sigma}_{rz}^{(1)} = \frac{1}{\xi}\int_{r_1}^{r_2} \sigma_r^{(1)} dr \end{gathered} \tag{40}$$

Perfect contact

$$W_z^{(1)} = W_z^{(2)}; \quad \sigma_{zz}^{(1)} = \sigma_{zz}^{(2)}; \quad \overline{\sigma}_{rz}^{(1)} = 0; \qquad \sigma_{rz}^{(2)} = 0 \tag{41}$$

Having approximate expressions for displacements and stresses at the end points of the cylindrical shell (32) and (33), the material parameters will be denoted by the index "1", and the plates-by the index "2", while the approximate expressions for the necessary displacements and stresses at the points of the plate have the form

$$\begin{gathered} W_z^{(2)} = W_2 + \left[(1-C_2)\lambda_{222}^{(1)} + C_2\Delta\right]W_2\frac{h^2}{2}; \\ u_r^{(2)} = -\frac{\partial W_2}{\partial z}h + \frac{\partial}{\partial r}\left[C_2\Delta - (1-C_2)\lambda_{22}^{(1)}\right]W_2\frac{h_3}{6}; \\ M_2^{-1}\sigma_{zz}^{(2)} = \left[\left(\lambda_{22}^{(1)} + \Delta\right)W_2\right]h + \left[4C\Delta\lambda_{22}^{(1)} + \lambda_{12}^{(1)}\left(\lambda_{12}^{(1)} + \Delta\right)\right]W_2\frac{h^3}{6}; \\ M_2^{-1}\sigma_{rz}^{(2)} = \left[2\lambda_{12}^{(1)} - C\left(2\lambda_{222}^{(1)} - \Delta\right)\right]\frac{\partial W_2}{\partial z}\frac{h^2}{2}. \end{gathered} \tag{42}$$

Using the approximate expressions (32), (33) and (42), from the conditions (40) we obtain the system

$$\begin{gathered} U_{z,0}^{(1)} - \frac{\xi}{2}U_{r,1}^{(1)} = W_2; \\ \frac{\partial U_{r,1}^{(1)}}{\partial z} + U_{z,1}^{(1)} = 0; \\ (1+C_1)\frac{\partial U_{z,0}^{(1)}}{\partial z} - (1-C_1)U_{r,0}^{(1)} - \frac{\xi}{2}\times \\ \times\left[(1+2C_1)\frac{\partial U_{z,1}^{(1)}}{\partial z} - (1-2C_1)\lambda_{21}^{(1)}U_{r,1}^{(1)}\right] = M_1^{-1}M_2\left[\left(\lambda_{22}^{(1)} + \Delta\right)W_2 h\right]; \end{gathered} \tag{43}$$

$$\left[(1-C_1)\frac{\partial U_{r,0}^{(1)}}{\partial z}+(1+C_1)\lambda_{11}^{(1)}U_{r,0}^{(1)}\right]\frac{r_2^2-r_1^2}{2\xi}=$$

$$M_1^{-1}M_2\left\{\left[2\lambda_{12}^{(1)}-C_1\left(2\lambda_{22}^{(1)}-\Delta\right)\right]\frac{\partial W_2}{\partial z}\right\}\frac{h^2}{2};$$

$$\frac{r_2^2-r_1^2}{4\xi}U_{r,0}^{(1)}-\ln\frac{r_2}{r_1}U_{r,1}^{(1)}=-\frac{\partial W_2}{\partial z}h$$

or, after elimination, we obtain the boundary conditions of the elastic end fitting shells taking into account the influence of plate-plate deformability

$$(1+C_1)\frac{\partial U_{z,0}^{(1)}}{\partial z}-(1-C_1)U_{r,0}^{(1)}-\frac{\xi}{2}\left[(1+2C_1)\frac{\partial U_{z,1}^{(1)}}{\partial z}-(1-2C_1)\lambda_{21}^{(1)}U_{r,1}^{(1)}\right]=M_1^{-1}M_2\left\{\left[\lambda_{22}^{(1)}+\Delta\right]\times\right.$$
$$\left.\times\left(U_{z,0}^{(1)}-\frac{\xi}{2}U_{r,1}^{(1)}\right)h\right\};$$

$$\frac{\partial U_{r,1}^{(1)}}{\partial z}+U_{z,1}^{(1)}=0;$$

$$\left[(1-C_1)\frac{\partial U_{r,0}^{(1)}}{\partial z}+(1+C_1)\lambda_{11}^{(1)}U_{r,0}^{(1)}\right]\frac{r_2^2-r_1^2}{2\xi}=M_1^{-1}M_2\left\{\left[2\lambda_{12}^{(1)}-C_1\left(2\lambda_{22}^{(1)}-\Delta\right)\right]\left[\frac{r_2^2-r_1^2}{4\xi}U_{r,0}^{(1)}-\ln\frac{r_2}{r_1}U_{r,1}^{(1)}\right]\frac{h}{2}\right.$$

Similarly, for an ideal contact (41) we obtain a system

$$U_{z,0}^{(1)}-\frac{\xi}{2}U_{r,1}^{(1)}=W_2;\qquad\frac{\partial U_{r,1}^{(1)}}{\partial z}+U_{z,1}^{(1)}=0;\qquad\frac{\partial W_2}{\partial z}=0;\ (44)$$

$$(1+C_1)\frac{\partial U_{z,0}^{(1)}}{\partial z}-(1-C_1)U_{r,0}^{(1)}-\frac{\xi}{2}\left[(1+2C_1)\frac{\partial U_{z,1}^{(1)}}{\partial z}-(1-2C_1)\times\right.$$
$$\left.\times\lambda_{21}^{(1)}U_{r,1}^{(1)}\right]=M_1^{-1}M_2\left[\left(\lambda_{22}^{(1)}+\Delta\right)W_2h\right];$$

$$\left[(1-C_1)\frac{\partial U_{r,0}^{(1)}}{\partial z}+(1+C_1)\lambda_{11}^{(1)}U_{r,0}^{(1)}\right]=0$$

and for the end of the shell

$$(1+C_1)\frac{\partial U_{z,0}^{(1)}}{\partial z}-(1-C_1)U_{r,0}^{(1)}-\frac{\xi}{2}\left[(1+2C_1)\frac{\partial U_{z,1}^{(1)}}{\partial z}-(1-2C_1)\times\right.$$
$$\left.\times\lambda_{21}^{(1)}U_{r,1}^{(1)}\right]=M_1^{-1}M_2\left\{\left(\lambda_{22}^{(1)}+\Delta\right)\left(U_{z,0}^{(1)}-\frac{\xi}{2}U_{r,1}^{(1)}\right)h\right\}\qquad(45)$$

$$\left[(1-C_1)\frac{\partial U_{r,0}^{(1)}}{\partial z}+(1+C_1)\lambda_{11}^{(1)}U_{r,0}^{(1)}\right]=0;\qquad\frac{\partial U_{r,1}^{(1)}}{\partial z}+U_{z,1}^{(1)}=0;$$

The initial conditions for the variables $U_{z,j}^{(1)},U_{r,j}^{(1)}$ it is easy to obtain three-dimensional initial conditions for the displacements

$$u_r = f_1(r,z); \qquad u_z = f_2(r,z); \qquad (46)$$

$$\frac{\partial u_r}{\partial t} = f_3(r,z); \qquad \frac{\partial u_z}{\partial t} = f_4(r,z) \qquad (t=0)$$

The results obtained allow us to formulate boundary value problems in solving specific problems of the cylindrical shell oscillation under different conditions at the end of the shell.

REFERENCES

[1] Filippovو I.G., S.I. Filippov, **1995**. Dynamic stability theory of rods. Proceedings of the Russian-Polish seminar. Theoretical Foundations of construction. Warsaw, pp.63 -69.

[2] Filippov, I.G., **1979**. An approximate method for solving dynamic viscoelastic media. PMM, 43(1): 133 -137.

[3] Filippov, I.G., S.I Filippov, V.I. Kostin, **1995**. Dynamics of two-dimensional composites. - Proceedings of the International Conference on Mechanics and Materials, USA, Los Angeles, pp.75 -79.

[4] Seytmuratov, A.Zh., **2010**. Determination of natural frequencies of the plate. Bulletin Treasury Series mathematics, mechanics, computer science, 4 (67): 120.

[5] Seytmuratov, A.Zh., **2010**. The impact of the moving load on the surface of a layered elastic half-plane. Herald KazNPU., 3: 112-11

[6] Brunelle, E.J., **1977**. Buckling of transversely isotopic Mindlen plates, AIAA, 9(6): 1018-1022.

[7] Bergman, G.G., **1981**. Elastic waves propagation in fluid saturated porous media G. Asoust. Soc. America., 2: 416-424.

[8] Bowen, P.M., **1980**. Incompressible porous media models by use of the theory mixtures. Int. J. Engng. Sci., 18: 1129-1148.

[9] de Boer, R., **2000**. Theory of porous media. Berlin: Springer.

[10] Ellsiepen, P., **1999**. Zeit- und ortsadaptive Verfahren angewandt auf Mehrphasenprobleme poroser Medien. Bericht Nr. II-3, Universitat Stuttgart, Institute for Mechanik, Lehrstuhl II.

[11] Diebels, S., W. Ehlers, **1996**. Dynamic analysis of a fully saturated porous medium accounting for geometrical and material non-linearities. Int. J. Num. Methods Engng 39: 81-97.

[12] Diebels, S., W. Ehlers, B. Markert, **2001**. Neglect of the fluid-extra stresses in volumetrically coupled solid-fluid problems. ZAMM 81, S521-S522.

[13] Umbetov, U., A.Zh. Seytmuratov, **2012**. Decomposition approach to the modeling of seismic resistance of building structures. M., PAE. Modern high technologies, 6: 43.

Н.Қ.Медеубаев[1], С.Меңліхожаева[2], А.Ж.Сейтмұратов[2], М.И.Рамазанов[1], Б.К.Жарменова[2], Т.Шамилов[3]

[1]Е. Бөкетов атындағы Қарағанды мемлекеттік университеті,
Қазақстан Республикасы. Қарағанды қ.;
[2]Қорқыт Ата атындағы Қызылорда мемлекеттік университеті, Қазақстан Республикасы. Қызылорда қ.;
[3]Азербайджан Архитектура және Құрылыс университеті , Азербайджан Республикасы. Баку қ.

ҚАЛЫҢДЫҒЫ АЙНЫМАЛЫ БОЛАТЫН СЫРЫҚТЫҚ ЖҮЙЕНІҢ АЙНАЛМА ТЕРБЕЛІСІНІҢ ЖУЫҚ ТЕҢДЕУІНІҢ ҚОЛДАНУ АУМАҒЫ

Аннотация: Мақалада қалыңдығы айнымалы болатын сырықтық жүйенің айналмалы тербелісінің жуық теңдеуінің туындысының реті, сырықтың сыртқы шартына тәуелді жағдайындағы тербелісінің жуық теориясын құруға мүмкіндік беретінін қарастырады. Берілген функцияның туындысы екіден жоғары болатын сырықтық жүйенің тербелісінің жуық теңдеулері жайлы ғылыми әдебиеттерде іс-жүзінде мүлдем аз қарастырылған. Дегенмен туындысы екінші реттен жоғары болатын жуық теңдеулер түрі, әр түрлі негізде болатын теңдеулер теориясының жуық есебін зерттеу қажеттілікті тудырады. Сол себептен есепте радиусы тұрақты болатын сырықтар үшін берілген U_θ функциясы немесе θ бұрыштық координатасынан тәуелді болатын ығысу айналымының зерттеу аумағын қарастырады.

Түйін сөз: айналмалы тербеліс, сырық, жүйе, қалыңдығы айнымалы, цилиндр, қабықша, радиус, Бессел функциясы.

Н.К.Медеубаев[1], С.Менлихожаева[2], А.Ж.Сейтмуратов[2],
М.И.Рамазанов[1], Б.К.Жарменова[2], Т.Шамилов[3]

[1]Карагандинский государственный университет им.Букетова, Республиуа Казахстан. г.Караганда;
[2]Кызылординский государственный университет им.Коркыт Ата, Республиуа Казахстан. г.Кызылорда;
[3] Азербайджанский университет Архитектуры и Строительства, Республика Азербайджан. г.Баку

ОБЛАСТЬ ПРИМЕНИМОСТИ ПРИБЛИЖЁННЫХ УРАВНЕНИЙ СТЕРЖНЕВЫХ СИСТЕМ ПЕРЕМЕННОЙ ТОЛЩИНЫ

Аннотация: Приведённые в данной работе приближённые уравнения крутильного колебаний стержневых систем переменной толщины позволяют строить приближённые теории колебания в зависимости от условий на торцах стержня, порядка производных от искомых в приближённых уравнениях и начальных условий.

Приближённые уравнения колебаний стержневых систем выше второго порядка по производным от искомой функции в научной литературе практически не встречаются.

С другой стороны, приближённые уравнения, содержащие производные выше второго порядка, нуждаются в исследовании области применимости той или иной теории на основе различных приближённых уравнений. Для простоты рассмотрим область применимости для стержня постоянного радиуса, когда искомая функция U_θ или вращательное смещение зависит от угловой координаты θ, т.е. исследуем область применимости приближённых уравнений колебания на основе общего уравнения колебания

Ключевые слова: крутильная колебания, стержень, система, переменная толщина, цилиндр, оболочка, радиус, функция Бесселя

Information about authors:

Medeubaev Nurbolat -a senior teacher of department is "Algebra, mate. logic and geometry", Buketov. Karaganda State University.Karaganda.

Seitmuratov Angisin – Doktor of Physical and Matematical Sciences, Professoz, The Korkyt Ata Kyzylorda State University. Kyzylorda.

Menlikozhaeva Sauleh Koilibaevna - kandidate of Pedagogical sciences,associate professor, The Korkyt Ata Kyzylorda State University, Kyzylorda.

Ramazanov Murat- Doktor of Physical and Matematical Scences, Professoz, Buketov. Karaganda State University.Karaganda.

Zharmenova Botagoz Kuanyshevna- Master degree of mathematical sciences, The Korkyt Ata Kyzylorda State University, Kyzylorda.

Shamilov Tefriz- Candidate of Technical Sciences, Professoz, Departament of «Physics»,Azerbaijan University of Architecture and Construction, Azerbaijan, Baku.

N E W S
OF THE NATIONAL ACADEMY OF SCIENCES OF THE REPUBLIC OF KAZAKHSTAN
PHYSICO-MATHEMATICAL SERIES
ISSN 1991-346X
Volume 4, Number 320 (2018), 15 – 21

UDC 523.62

G.S. Minasyants[1], T.M. Minasyants[1], V.M. Tomozov[2]

[1]Fesenkov Astrophysical Institute, Almaty, Kazakhstan;
[2] Institute of Solar-Terrestrial Physics, Irkutsk, Russia
E-mail: gennadii_minasya@mail.ru, gennadii_minasya@mail.ru, tom@iszf.irk.ru

FEATURES OF THE DEVELOPMENT OF GAMMA-RAYS IN A SOLAR FLARE FEBRUARY 25 2014

Abstract. A flare event February 25 2014 was investigated, which was a source of radiation in the gamma range. Photometric processing of the photogeliograms λ1700Å (ultraviolet continuum, SDO spacecraft) is used to plot the temporal profile of the change in the relative intensity of a bright plasma of flare. The coincidence in time of the amplified emission of gamma photons (10keV-50MeV) and the maximum intensity of the flare plasma flowing down to the photosphere, during of the impulsive phase of flare, is established. In this case, the most effective was the increase in the number (up to 10^4 times) of gamma photons with energy (50-300) keV. During the development of the main phase, the priority source of gamma rays is nuclear reaction of high-energy flare protons, which received additional acceleration on the shock front of high-speed coronal mass ejection. Observed on February 25, 2014, the value of the gamma-ray flux in the energy range (100MeV-10GeV) turned out to be one of the highest for the entire FERMI telescope operation in 2009-2017.

Keywords: Solar flares, photometry, gamma rays.

Introduction

Use of the observation data obtained on the modern spacecrafts (SC) allows to investigate development of solar flare processes in various intervals of energy, including also γ-range. Development of flare is connected with allocation of free magnetic energy in active area owing to her dissipation in current layers because of magnetic reconnection with the subsequent action of stochastic acceleration at development of various plasma not stability [1-3]. The most powerful flares belonging to the class of gradual events often are followed by Coronal Mass Ejections (CME). On modern representations, the flare and CME are considered as the uniform process connected with violations of balance of magnetic structure in active area. In the course of flare energy release, at annihilation of a current sheets there is an intensive heating of plasma and acceleration of particles to high energy. Besides, high-speed CME are capable to excite shock waves on which fronts particles effectively accelerate at the movement of flare fluxes of plasma near the Sun and in the interplanetary environment.

During development of a impulse phase of flare from area of primary energy release fluxes of quickly moving currents of plasma, thermal waves and high-energy charged particles which part on magnetic and power tubes extends down are observed. At interaction with denser plasma in the bases of loops, it is generated bremsstrahlung: X-ray, gamma radiation. And also the surrounding plasma is heated. Rapid and considerable heating of plasma in the photosphere and the chromosphere leads to "evaporation" and rise it up and to filling of all volume of magnetic arches. During this period the greatest strengthening of soft x-ray radiation is observed. Further the main phase at which heated plasma in the system of arches radiates a long time in the soft x-ray range follows, gradually losing energy [4]. And at the same time on this background there is an interaction of flare streams to the developing coronal ejection.

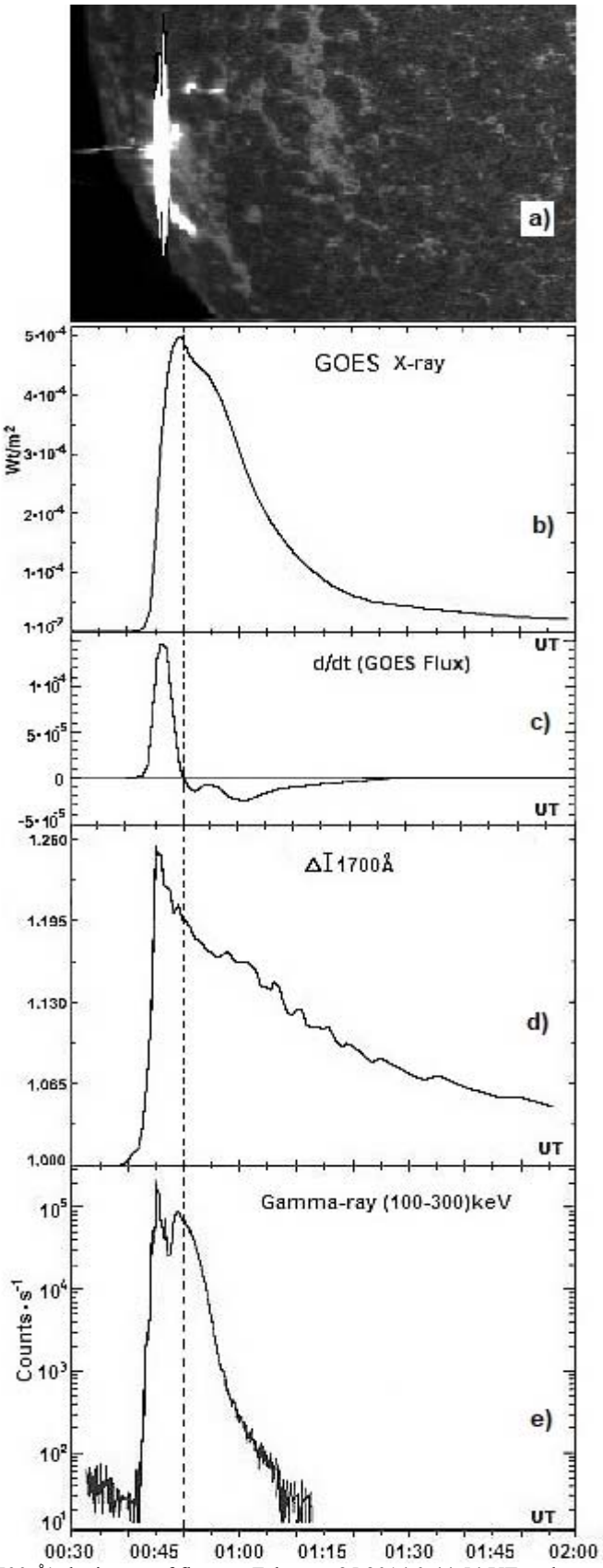

Figure 1 - a) - photospheric (1700 Å) the image of flare on February 25 2014 0:44:54 UT at the moment of its maximum relative intensity; b) - temporary change of a flux of X-ray radiation of flare (1-8) Å, his derivative (c), relative intensity of photospheric flare plasma (d) and counts gamma photons with energy (100-300) keV (e)

Processing of observational data

The intensity of heated plasma in the photosphere is defined by the power of flare process in a corona. For powerful flares in a maximum of an impulse phase sites of hot plasma with an excess brightness of radiation for photo matrix pixels can appear. It leads to overflowing (from pixels with the excess charges on the next pixels which don't have such surplus) charges of pixels of a photo matrix (blooming) and to emergence in pictures of bright moustaches, tool origin, and sent to the opposite sides from sites with the overestimated brightness. For flares of the cells of the photodetector causing overflow it has been established that it occurs during the periods of formation of high energy quanta of radiation.

In article on the example of development of an event on February 25 2014 (X4.9 S12 E82, the beginning of 00:39 UT) by means of the observation data obtained on various spacecrafts have considered properties of process of formation of flare gamma radiation.

On photogeliograms of SC SDO λ1700 Å (the ultra-violet image of the top photosphere, a temperature minimum) with good spatial resolution bright sites of the flare plasma which is flowing down are presented. By means of specially developed program, photometric processing of these pictures is carried out and the time profile of change of relative intensity ΔI λ1700 Å photospheric flare plasma (fig.1d) is received. The intensity of the preflare undisturbed photosphere was accepted for 1.00. Temporary resolution for separate measurements is ~ 50 sec.

Comparing all given parts of the figure 1, it is possible to notice: the flare plasma which is flowing down on photosphere level, had very high brightness that has led to noticeable manifestation on a photogeliogram of effect of a blooming in the form of bright thin moustaches in opposite directions. The impulse phase of flare proceeded 11 minutes from 00:39 till 00:50. The end of impulse phase is noted in the drawing by a vertical dash line. Her situation is defined by the moment when value of a derivative of change of a flux of X-ray radiation (c) becomes equal to zero, upon transition from growth to falling X-ray. Further at negative values of a derivative d/dt (X-ray) development of the main phase of flare radiation begins. Time interval between a maximum of a derivative of radiation X-ray and the beginning of the main phase is considered to be an explosive stage of impulse phase. During this period, it is supposed that the flare plasma which is below at the level of the photosphere and the chromosphere begins to rise promptly upward and to fill all volume of coronal arches, leading them to the maximum luminescence. It is remarkable that on time the moments of maxima of relative photosphere intensity (fig.1d) and derivative d/dt (X-ray) (fig.1c) practically coincide for impulse phase of flare. It is necessary to consider that the time profile of change of counts of photons with energy (100-300) keV (fig.1e) has the form rather close from curve of relative photosphere intensity (fig.1d) at coincidence of maxima of curves.

The most vigorous episode of flare issue in the photosphere in the period of impulse phase of flare (0:44:06 0:44:54 UT) coincides on time with the maximum values of counts of gamma photons not only with energy (100-300) keV (fig.1), but also (50-100) keV, (300-1000) keV, (1000-50000) keV – of SC FERMI the BGM device and also – (300-800) keV and (800-7000) keV of SC RHESSI (fig. 2). But in view of the fact, flare strengthening of the most significant amount of gamma photons with energy (50-100) keV and (100-300) keV (the count has increased by 10^4 times), it is possible to assume that photons of such energy flare plasma during development of impulse phase most effectively made.

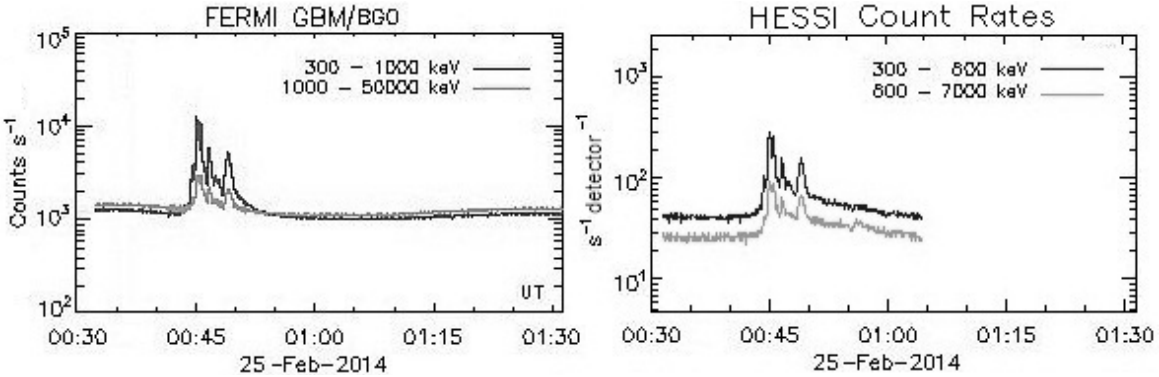

Figure 2 - Changes counts of gamma photons (300–50000) keV during flare development on February 25 2014. Data of observations of SC FERMI and SC RHESSI

At the same time on images of the photosphere the most considerable effect of excess radiation which is shown in the form of extended narrow beams is visible during an interval, with a maximum at 00:44:54 to UT (see fig. 1). That is, there is a coincidence on time of the strengthened radiation of gamma photons to the maximum flare intensity of the photosphere. It is indicated the most probable source by gamma ray - the bremsstrahlung of electrons in the field of highly density photospheric plasma. This indicates the most probable source gamma rays - the bremsstrahlung of electrons in the field of highly density photospheric plasma.

Observations on SC GOES have shown strengthening of streams of electrons from it E_e- >4 MeV and also protons with E_{p+} >100 MeV, at flare development.

During the termination of impulse phase of flare on February 25 at 00:43:00 UT has begun to develop coronal ejection which at 00:55:00 UT already was at distance ~2.0 $R_\odot$ (SC STEREO A). According to data from the LASCO C2 and C3 (telescopes SC SOHO) ejection type Halo had very high linear speeds at development near the Sun: (2069-2147) km/s. At the same time at a body of CME there was a characteristic structure of the forward shock front (fig. 3).

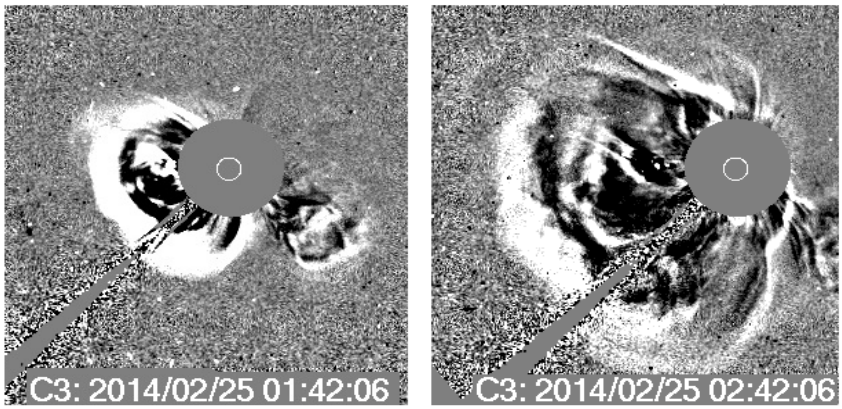

Figure 3 - Development of CME on February 25 2014 according to pictures of SOHO C3

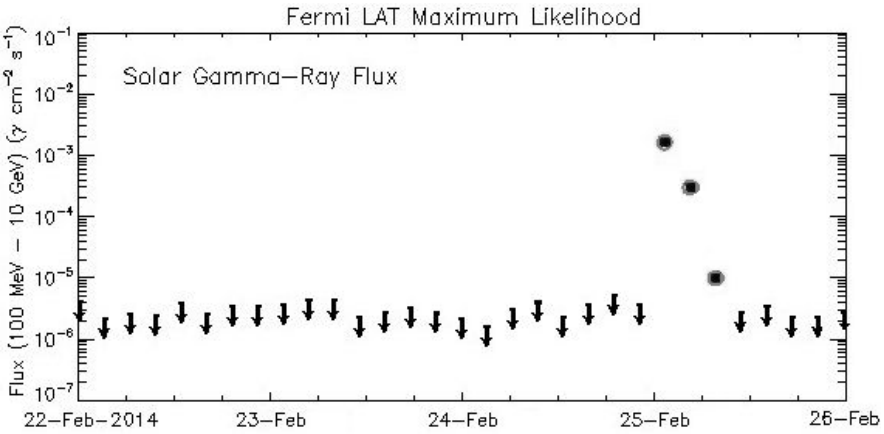

Figure 4 - Values of fluxes of a gamma radiation in the range
of energy (100 MeV-10 GeV) according to SC FERMI on the LAT tool

At development of high-speed CME usually there are shock waves which are an additional source of acceleration of flare protons in the top layers of a corona and in the interplanetary environment. The flare protons accelerated on the shock front of ejection become a source of radiation of gamma photons of highest energy [5]. Collision of high energy protons with protons of low energy is resulted by nuclear reaction with formation of pion-decay (neutral and charged) which in the course of the disintegration form scale gamma photons of high energy. So the SC FERMI on the LAT tool in the range of energy (100 MeV-10 GeV) for three periods of observations (fig. 4) has registered on February 25 2014 the following values of fluxes of gamma radiation:

01:10:30 - 01:30:30 Fγ=1.62·10^{-3}(γ cm^{-2} s^{-1})
04:20:30 - 04:41:30 Fγ=2.45·10^{-4}(γ cm^{-2} s^{-1})
07:30:30 - 07:52:30 Fγ=9.73·10^{-6}(γ cm^{-2} s^{-1})

During flare development on February 25 2014 values of a flux of gamma-photons in the range of energy (100 MeV-10 GeV), the second in value for the entire period of observations of the Sun on the FERMI telescope were registered (2009-2017). Such high of values of fluxes of the accelerated particles and photons of various energies, the bound to development of the active process in the form of direct flare strengthening and shockwaves of ejection, in many respects were defined by influence of efficient structure of a magnetic field of group of spots. The active region AR 11990 during the considered period had the complex configuration of a class δ that is confirmed by the magnetograms received on SC SDO.

The flare developed on February 25 2014 practically on east edge of the Sun (E82). Because of it fluxes of the charged particles, following is magnetic power lines, were recorded near-earth satellite devices with a delay and, the most important, strongly weakened. At the same time, the flare images and CME show a fairly large event power, this is also confirmed by the fluxes of photons having hard gamma energy. SC GOES near Earth fixed only slight increase fluxes of protons with energy >10 MeV and >100 MeV, and the *pfu* index by means of which quantitatively estimate proton events had rather small value (*pfu*=103).

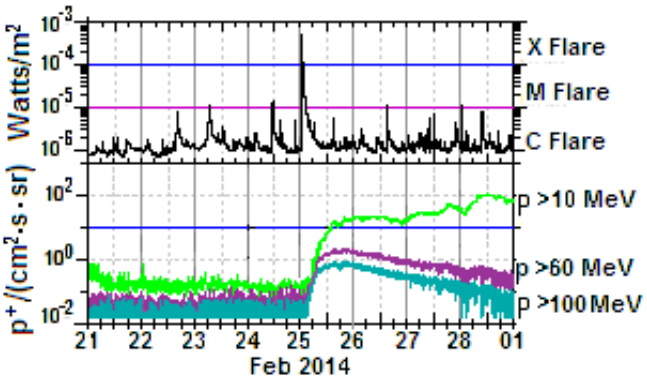

Figure 5 X-ray radiation (1-8) Å and integral fluxes of protons of flare on February 25 2014 according to SC GOES

Data of SOHO indicate arrival of the shock front of CME (Shock4) only on February 27, in 63 hours after its emergence and having a linear velocity V=440 km/s, which the close to the speed of a calm solar wind. At the same time, it is necessary to consider that CME speed at its near the Sun, was ≥2000 km/c. Thus, secondary signs of an event on February 25 the bound to passing of particles through interplanetary space, point to the strong degradation of their quantitative parameters. So the event is on February 25, 2014 also good example of influence of the interplanetary space which is strongly distorting properties of primary signs of flare process on condition of its development near east edge of the Sun.

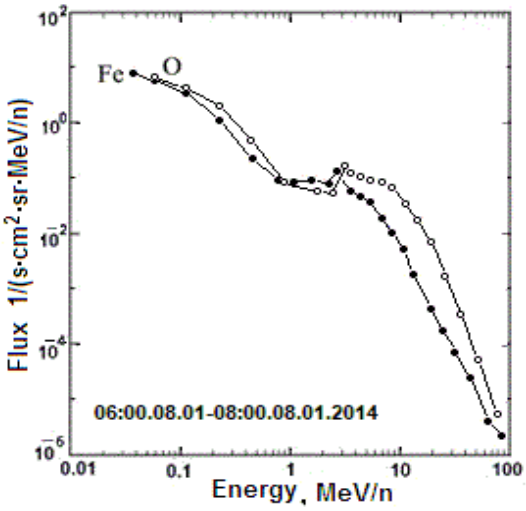

Figure 6 - Fluxes intensity jumps in spectra energy of ions Fe and O at development of a flare event on January 7, 2014

For comparison, consider the development of flare and coronal ejection on January 7 2014 which had quite efficient conditions when driving of the accelerated particles to Earth magnetosphere. The flare January 7 2014: X1.2, coordinates – S12W12, start – 18:04 UT, max - 18:32 UT. The beginning of development of coronal ejection – 18:24 UT, at the speed near the Sun (1714-1830) km/s. Arrival to Earth of the shock front of CME - Shock4 on January 9 at 19:33 UT, after 49.5 hour at a speed of V = 525 km/s. The most important superiority had event on January 7 an in the quantitative assessments of fluxes of high energy protons near Earth. The proton *pfu*=1033 index much surpassed the corresponding value for a February event. Presence of high energy fluxes of protons of E_k >60 MEV with intensity of Fp $>10^2$ $1/(s \cdot cm^2 \cdot sr)$ is confirmed by existence of sharp jumps of intensity in spectra energy of ions in the range of 1.5–2.5 MeV/n in the period of the disturbed phase of development of January flare of 2014 (fig.6) [6].

However, as a result, extent of geomagnetic influence of an event on February 25 nevertheless was higher. First, it is necessary to consider that the impulse phase of flare on February 25, more powerful in the X-ray class, was almost three times shorter, than at flare on January 7 (10 min and 28 min). This enhanced effectiveness of process of acceleration of particles, and undoubtedly the significant role in it was also played by the superiority in the linear speed of CME near the Sun (2147 km/s in comparison with 1830 km/s). Secondly, CME on February 25 had more complex magnetic structure (amplitude of the southern component of an interplanetary magnetic field was Bz=-12 nT) that resulted in value of the Dst=-97 nT index which corresponds to border between a moderate and strong geomagnetic storm. Arrival of January ejection caused only very weak geomagnetic disturbance of Dst=-22 nT at Bz=-5 nT.

The most noticeable superiority of an event on February 25 is shown in generation of gamma-ray fluxes of various energy during the development of impulse phase of flare and especially in the period of the main phase with the most probable powerful acceleration of protons on shockwaves of coronal ejection. For the most vigorous photons in the gamma range (100 MeV-10 GeV) in a February event, we can oppose only photons in the gamma range (1-50) MeV in a January event.

Discussion of the results. Conclusions

Change of intensity of bright plasma at the level of a photosphere λ1700 Å is the good indicator characterizing strengthening direct flare radiation – including fluxes of gamma photons.

Feature of development of flare during impulse phase was process of formation of gamma-photons of high energy in the range of (1-50) MeV as result of impact of the flowing-down flare plasma on a photosphere. In this case, the observed maxima of counts of gamma photons of different energies and the relative intensity of the bright photospheric plasma coincide in time.

For the event under consideration in during the main phase the development, a rather close interaction is characteristic of the flare process and a powerful coronal ejection (the beginning of flare 0:39:00 and of ejection 0:43:00). Accelerated on shockwaves of ejection, protons with energy of E_k >100 MeV, became a source of high intensity of a flux gamma ray photons of range (100 MeV-10 GeV). It was possibly result of a nuclear interaction of additionally accelerated protons with protons of routine energies at which there are formed peonies, decaying up with the emergence of gamma photons. At that, the newly formed gamma photons have the energy of the initial high energy protons.

It is necessary to point out one feature of development of the main phase of an event – larger duration of presence of a gamma ray emission range (100 MeV-10 GeV): not less than 7 hours.

Thus, an event on February 25, 2014 - a good example very efficient at all stages of development of a source of the emergence of gamma ray photons of the widest range of energy.

Acknowledgements

Authors express gratitude to groups of the scientists supervising carrying out observations on SDO, GOES, WIND, SOHO, STEREO, FERMI, RHESSI spacecrafts for providing the experimental data published on the Internet.

Work is supported by the Program of target financing BR05336383 of Space committee of MOAP of the Republic of Kazakhstan and Russian basic financing on Program FSR II.16.

REFERENCES

[1] Altyntsev A.T., Banin V.G., Kuklin, Tomozov V.M. Solar Flares. Moscow: Science, -1982. P.246.

[2] Prist E.R., Forbes T. Magnetic reconnection. Magneto-hydrodynamic theory and applications. M.: Fizmatlit, 2005. P.591.

[3] Somov B.V. Plasma Astrophys.: Reconnection and Flares // Springer: New York. 2013. P.504. DOI: 10.1016/S02731177(97)00968-X.

[4] Livshits M.A. Solar flares: results of observations and gasodynamic processes//Plasma Heliogeophysics. Under the editorship of L.M. Zeleny and I.S. Veselovsky. The collection in 2 t. Volume 1. M of 2008. P. 60-81.

[5] Murphy R.J., Dermer C.D., Ramaty R. High-energy processes in solar flares // Astrophys. J. Suppl. V.63. 1987. P.721-748.

[6] Minasyants G.S., Minasyants T.M., Tomozov V.M. Fe/O ratio behavior as an indicator of solar plasma state at different solar activity manifestations and in periods of their absence. Solar-Terrestrial Physics. 2018, vol. 4, no. 1, P. 29–50. DOI: 10.12737/stp-41201804.

Г. Минасянц[1], Т. Минасянц[1], В. Томозов[2]

[1] В.Г. Фесенков атындағы Астрофизикалық институт, Обсерватория-23, Алматы, Қазақстан;
[2]Күн-Жер Физикасы ннституты, Лермонтов көш. 126-а, Иркутск, Ресей

2014 ЖЫЛДЫҢ 28 АҚПАНЫНДАҒЫ КҮН ЖАРҚЫЛЫНДАҒЫ ГАММА-СӘУЛЕЛЕНУДІҢ ДАМУЫНЫҢ ЕРЕКШЕЛІКТЕРІ

Аннотация. 2014 жылдың 24 ақпанында гамма-диапазонда сәулеленудің көзі болып табылатын жарқыл процессінің зерттеуі жүргізілді. Фотогелиограммдар λ1700Å (ультракүлгін континуум, SDO ғарыш аппараты) фотометрлік өңдеулерінің көмегімен жарық жарқыл плазмасының қарқындылығына қатысты салыстырмалы өзгерістің уақытша кескіні құрылды. Гамма-кванттың (10keV-50MeV) күшейтілген сәулеленуі уақыты және жарқылдың импульстік кезеңінің даму кезінде фотосфераға дейін төмен ағатын жарқыл плазмасының ең жоғары қарқындылығы бойынша сәйкестіктер тағайындалды. Бұл ретте (50-300)keV энергиямен гамма-кванттардың санының артуы (10^4 есеге дейін) айтарлықтай тиімді болып шықты. Массаның жоғары жылдамдықтағы корональ шығарылуы соққысы бағытында қосымша үдету алған жоғары энергиялық жарқыл протондарының ядролық реакциялары басты кезеңнің дамуы кезінде гамма сәулеленудің негізгі көзі болады. 2009-2017 жылдары FERMI телескобының барлық жұмыс уақытында (100MeV-10GeV) диапазонында гамма- кванттардың ағымының бірден бір ең жоғары мәні бақыланды.

Түйін сөздер: күн жарқылы, фотометрия, гамма сәулелену

УДК 523.62

Г. Минасянц[1], Т. Минасянц[1], В. Томозов[2]

[1]Астрофизический институт им. В.Г. Фесенкова, Обсерватория-23, Алматы, Казахстан;
[2]Институт Солнечно-Земной Физики, ул. Лермонтова 126-а, Иркутск, Россия

ОСОБЕННОСТИ РАЗВИТИЯ ГАММА-ИЗЛУЧЕНИЯ В СОЛНЕЧНОЙ ВСПЫШКЕ 25 ФЕВРАЛЯ 2014 ГОДА

Аннотация. Проведено исследование вспышечного процесса 25 февраля 2014 года, который явился источником излучения в гамма-диапазоне. С помощью фотометрической обработки фотогелиограмм λ1700Å (ультрафиолетовый континуум, космический аппарат SDO), построен временной профиль изменения относительной интенсивности яркой вспышечной плазмы. Установлено совпадение по времени усиленного излучения гамма-квантов (10keV-50MeV) и максимальной интенсивности вспышечной плазмы, стекающей вниз до фотосферы, в период развития импульсной фазы вспышки. При этом наиболее эффективным оказалось увеличения количества (до 10^4 раз) гамма-квантов с энергией (50-300)keV. Во время развития главной фазы основным источником гамма излучения становятся ядерные реакции высокоэнергичных вспышечных протонов, получивших дополнительное ускорение на ударном фронте высокоскоростного коронального выброса массы. Наблюдалось одно из самых высоких значений потока гамма-квантов в диапазоне энергии (100MeV-10GeV) за все время работы телескопа FERMI в 2009-2017 годах.

Ключевые слова: солнечные вспышки, фотометрия, гамма излучение

Information about authors:
Minasyants Gennady Sergeevich - Fesenkov Astrophysical Institute, Leading Researcher, gennadii_minasya@mail.ru;
Minasyants Tamara Mihailovna - Fesenkov Astrophysical Institute, Senior Researcher, gennadii_minasya@mail.ru;
Tomozov Vladimir Mihailovich - Institute Solar-Terrestrial Physics, Senior Researcher, tom@iszf.irk.ru.

N E W S
OF THE NATIONAL ACADEMY OF SCIENCES OF THE REPUBLIC OF KAZAKHSTAN
PHYSICO-MATHEMATICAL SERIES
ISSN 1991-346X
Volume 4, Number 320 (2018), 22 – 35

B.K. Kozhakhmet[1], G.G. Kulikov[2], G.S. Nurbakova[1]

[1]Al-Farabi Kazakh National University, Almaty, Kazakhstan;
[2]National Research Nuclear University "MEPHI", Moscow, Russia
E-mail:bauyr.ko@gmail.com

IMPROVEMENT OF NEUTRON-PHYSICAL CHARACTERISTICS OF BN-600 FAST REACTOR BY USING ^{208}Pb BASED NEUTRON REFLECTOR

Abstract. As a rule, materials of small atomic weight (light and heavy water, graphite and so on) are used as neutron moderators and reflectors. A new very heavy atomic weight moderator is proposed – radiogenic lead consisting mainly of isotope ^{208}Pb. It is characterized by extremely small neutron radiative capture cross-section (~0.23 mbarn for thermal neutrons, i.e. less than that for graphite and deuterium) and highest albedo of thermal neutrons.

In previous works it is evaluated that the use of radiogenic lead makes it possible to slow down the chain fission reaction on prompt neutrons in a fast reactor. This can improve safety of fast reactor.

Here studied the effect of this kind of reflector on the neutron physical characteristics of BN-600 fast reactor

It is noteworthy that radiogenic lead with high ^{208}Pb content may be recovered from thorium (as well as thorium-uranium) ores without isotope separation. This has been confirmed experimentally by the investigations performed at San Paulo University, Brazil.

Keywords: improvement of fast reactor safety, increase of prompt neutron lifetime, ^{208}Pb based neutron reflector, BN-600 fast reactor.

I. INTRODUCTION

It is estimated that the use of lead-208 as a reflector makes it possible to slow down the chain fission reaction on prompt neutrons in a fast reactor. The longer lifetime of prompt neutrons can be achieved because ^{208}Pb is an extremely weak neutron absorber and moderator (heavy nuclide with weak elastic and inelastic scattering). Theoretical principles of this effect are presented in Refs.[1,2].

The purpose of this work is to study the neutron physical characteristics of a BN-600 reactor, with a reflector containing 208Pb. In the course of physical calculations, three reactor models were used that did not differ in the main parameters of the core (fuel type, coolant, fuel cladding, contact layer, fuel assembly materials). They differed only in the diameter of the core, in the thickness of blanket, in it content, also to equalizing the radial heat distribution, they have different enrichments.

The following main topics are considered the paper:

- basic neutron-physical properties and advantages of ^{208}Pb (Chapter II)
- demonstration how thick reflector from lead-208 affect on neutron physical characteristics of BN-600 and physical explanation of this effect
- the effects of a graphite layer placed behind the reflector from lead-208 and a fissile nuclide with a small value $\alpha = \sigma c / \sigma f$ located in the core region closed to reflector on the lifetime of the prompt neutrons.
- application of two different neutron kinetics models for analysis of transients in the fast reactor with neutron reflector

It is shown that the three-meter reflector from 208Pb leads to an increase in the asymptotic period of reactor acceleration. Thus, the power of a fast reactor with a thick reflector made of lead-208 with the introduction of large reactivities will not increase so rapidly, and with a certain value of the thermal constant of the fuel element, feedback will be able to work in the reactor on the heat carrier.

II. NEUTRONIC-PHYSICAL PROPERTIES AND ADVANTAGES OF RADIOGENIC LEAD

Its evaluated that thick reflector, mainly consist 208Pb, placed around the core prolong the lifetime of prompt neutrons. How does it work?! In the nature there are two types of elemental lead with substantially different contents of four stable lead isotopes (^{204}Pb, ^{206}Pb, ^{207}Pb and ^{208}Pb). The first type is a natural, or common, lead with a constant isotopic composition (1.4% ^{204}Pb, 24.1% ^{206}Pb, 22.1% ^{207}Pb and 52.4% ^{208}Pb). The second type is a so-called "radiogenic" lead with very variable isotopic composition. Radiogenic lead is a final product of radioactive decay chains in uranium and thorium ores. That is why isotopic compositions of radiogenic lead are defined by the ore age and by elemental compositions of mixed thorium-uranium ores sometimes with admixture of natural (common) lead as an impurity.

The isotopes ^{208}Pb, ^{206}Pb and ^{207}Pb are the final products of the radioactive decay chains starting from ^{232}Th, ^{238}U and ^{235}U, respectively:

$^{232}\text{Th} \rightarrow 6\alpha+4\beta$ ($14.6\cdot10^9$ years) $\rightarrow$ ^{208}Pb ,
$^{238}\text{U} \rightarrow 8\alpha+6\beta$ ($4.6\cdot10^9$ years) $\rightarrow$ ^{206}Pb ,
$^{235}\text{U} \rightarrow 7\alpha+4\beta$ ($0.7\cdot10^9$ years) $\rightarrow$ ^{207}Pb .

Therefore radiogenic lead with large abundance of ^{208}Pb could be extracted from natural thorium and thorium-uranium ores without any isotope separation procedures (Table I. [3-7]).

Table I - Main Deposits of Uranium, Thorium and Mixed Uranium-Thorium Ores. Elemental Compositions of Minerals and Isotope Compositions of Radiogenic Lead

Deposit	U / Th / Pb, (wt. %)	^{204}Pb / ^{206}Pb/ ^{207}Pb / ^{208}Pb, (at. %)	Age, 10^9 years
Monazite (Guarapari,Brazil)	1.3/59.3/1.5	0.005 / 6.03/ 0.46 / 93.5	0.52–0.55
Monazite (Manitoba,Canada)	0.3/15.6/1.5	0.01 / 10.2/ 1.86 / 87.9	1.83–3.18
Monazite (Mt. Isa Mine, Australia)	0.0/5.73/0.3	0.038 / 5.44/ 0.97 / 93.6	1.00–1.19
Monazite (Las Vegas,USA)	0.1/9.39/0.4	0.025 / 9.07/ 1.13 / 89.8	0.77–1.73
Uraninite (Singar Mine, India)	64.3/8.1/8.9	— / 89.4/ 6.44 / 4.18	0.885
Monazite (South Bug, Ukraine)	0.2/8.72/0.9	0.01 / 6.04/ 0.94 / 93.0	1.8–2.0

So, radiogenic lead can be taken as a by-product from the process of uranium and thorium ores mining. Till now, extraction of uranium or thorium from minerals had been followed by throwing radiogenic lead into tail repositories. If further studies will reveal the perspective for application of radiogenic lead in nuclear power industry, then a necessity arises to arrange by-extraction of radiogenic lead from thorium and uranium deposits or tails.

Radiogenic lead consisting mainly of stable lead isotope ^{208}Pb can offer unique advantages, which follow from unique nuclear physics properties of ^{208}Pb. Firstly, this lead isotope is a double-magic nuclide with completely closed neutron and proton shells. The excitation levels of ^{208}Pb nuclei (Fig. 1) are characterized with a high value of energy (the energy of the first level - 2.61 MeV) while the first excitation level of other lead isotopes have lower energy range (0.57–0.90 MeV).

This results in the fact that the threshold in energy dependence of ^{208}Pb inelastic scattering cross-section is at much higher energy compared to other lead isotopes (Fig. 2) [8].

Secondly, neutron radiative capture cross-section of ^{208}Pb in thermal point (~0.23 mb) is smaller by two orders of magnitude than that of natural lead (~174 mb) and even smaller than that of reactor-grade graphite (~3.9 mb). These differences remain be large within sufficiently wide energy range (from thermal energy to some tens of kilo-electron-volts). Energy dependence of neutron absorption cross-sections is presented in Fig. 2 for natural lead, stable lead isotopes, graphite and deuterium[8].

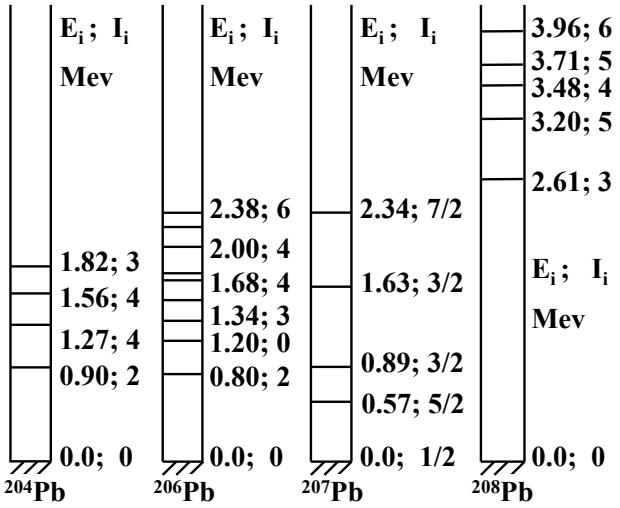

Figure 1 - The excitation levels of lead nuclei

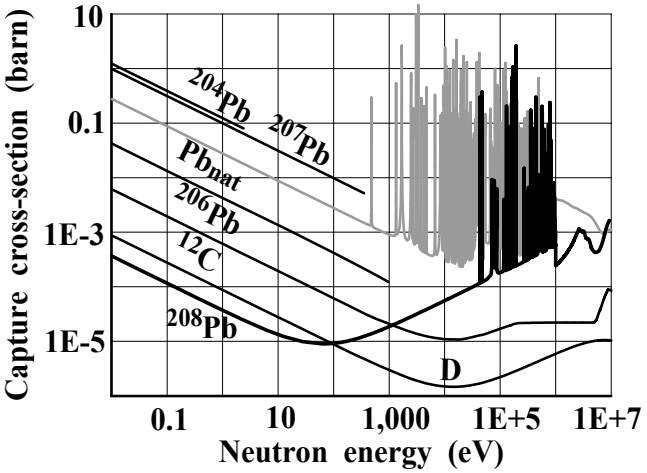

Figure 2 - Capture cross-section of various nuclides as a function of neutron energy (JENDL-4.0).

Thus, on the one hand, ^{208}Pb, being heavy nuclide, is a relatively weak neutron moderator both in elastic scattering reactions within full neutron energy range of nuclear reactors because of heavy atomic mass and in inelastic scattering reactions with fast neutrons because of high energy threshold of these reactions. On the other hand, ^{208}Pb is an extremely weak neutron absorber within wide enough energy range.

Some nuclear characteristics of light neutron moderators (hydrogen, deuterium, beryllium, graphite, oxygen) and heavy materials (natural lead and lead isotope ^{208}Pb) are presented in Table II. [8].

TABLE II - Neutron-Physical Characteristics of Some Materials

Nuc-lide	σ_{el}^{10eV} (barn)	Number of collisions (0.1 MeV→0.5 eV)	$\sigma_{(n,\gamma)}^{th}$ (mbarn)	$RI_{n,\gamma} + 1/V$ (mbarn)
^{1}H	30.1	12	332	149
^{2}D	4.2	17	0.55	0.25
^{9}Be	6.5	59	8.5	3.8
^{12}C	4.9	77	3.9	1.8
^{16}O	4.0	102	0.19	0.16
Pb_{nat}	11.3	1269	174	95
^{208}Pb	11.5	1274	0.23	0.78

One can see that elastic cross-sections of natural lead and ^{208}Pb do not differ significantly from the others nuclides, being between the corresponding values for hydrogen and other light nuclides. Neutron slowing-down from 0.1 MeV to 0.5 eV requires from 12 to 102 elastic collisions with light nuclides while the same neutron slowing-down requires about 1270 elastic collisions with natural lead or ^{208}Pb. The reason is the high atomic mass of lead in comparison with the other light nuclides. From this point of view neither natural lead nor ^{208}Pb are effective neutron moderators.

However, since ^{208}Pb is a double magic nuclide with closed proton and neutron shells, radiative capture cross-section at thermal energy and resonance integral of ^{208}Pb is much smaller than the corresponding values of lighter nuclides. Therefore, it can be expected that even with multiple scattering of neutrons on ^{208}Pb during the process of their slowing-down, they will be slowed down with a high probability and will create high flux of slowed down neutrons.

So, thanks to very small neutron capture cross-section, the moderating ratio (see Table III [8,9,10]), i.e. the average logarithmic energy loss times scattering cross-section divided by thermal absorption cross-section, of ^{208}Pb is much higher than that for light moderators. This means that ^{208}Pb could be a more effective moderator than such well-known light moderators as light water, beryllium oxide and graphite.

TABLE III - Properties of Neutron Moderators at 20ºC

Mode-rator	Average logarithmic energy loss, ξ	Mode-rating ratio, $\xi\Sigma / \Sigma_a^{th}$	Neutron age, τ (cm^2) (0.1 MeV →0.5 eV)	Diffusion length, L (cm)	Mean lifetime of thermal neutrons T_{th} (ms)
H_2O	0.95	70	6	3	0.2
D_2O	0.57	4590	58	147	130
BeO	0.17	247	66	37	8
^{12}C	0.16	242	160	56	13
Pb_{nat}	0.00962	0.6	3033	13	0.8
^{208}Pb	0.00958	477	2979	341	598

It is noteworthy that mean lifetime of thermal neutrons in ^{208}Pb is very large (about 0.6 s). This effect could be used to improve essentially safety of fast reactor by slowing down progression of chain fission reaction on prompt neutrons.[6] This assumes the greater significance under accidental conditions with destruction of the reactor core, when the energy yield is defined by lifetime of prompt neutrons because other kinetic parameters either out of any control (the inserted positive reactivity) or can not go out of the very limited range (Doppler coefficient, effective fraction of delayed neutrons, the reactor power).

As a reflector of thermal neutrons, isotope ^{208}Pb is inferior to light materials on the reflecting ability (albedo) with a thickness below 40 cm, but ^{208}Pb is superior to light materials with an increased thickness thanks to small capture cross-section (Fig. 3). This is one of the most important characteristics because the prolongation of prompt neutron lifetime is caused by the most long-lived slow and thermal neutrons coming back from the reflector into the reactor core.

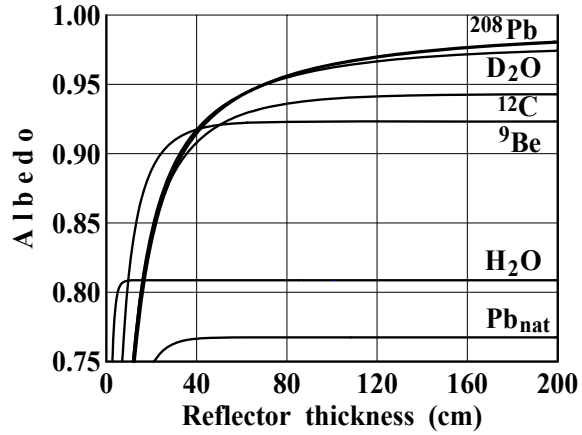

Figure 3 - Comparison of thermal neutron reflectors: dependence of albedo on thickness of reflector

III. SLOWING PROMPT NEUTRON CHAIN REACTION IN FAST REACTOR. PROMPT NEUTRON LIFETIME

Table IV summarizes relevant neutron-physical characteristics of some nuclear materials, including radiogenic lead (R-g Pb). It can be seen that natural lead is able to slow down only 30.4% of fast neutrons (0.1 MeV) into epithermal range (0.5 eV) while the remaining fraction (69.6%) is absorbed by natural lead in the slowing-down process. On the contrary, almost all fast neutrons (99.3%) can be slowed down by ^{208}Pb into epithermal range.

TABLE IV - Neutron-Physical Characteristics of Different Materials

Material /country	Slowing-down probability (0.1 MeV →0.5 eV)	$\sqrt{r_E^2}$ = cm	$\sqrt{r_{th}^2}$ = cm	Neutron lifetime, ms	
				Slowing down	Thermal
Pb_{nat}	0.304	$\sqrt{6\tau}$ 134	$\sqrt{6L}$ 30	0.56	0.8
^{208}Pb	0.993	134	835	0.56	598
D_2O	0.999	19	360	0.01	130
Graphite	0.998	31	138	0.03	13
R-g Pb in different countries*):					
Brazil	0.930	134	186	0.56	29
Australia	0.914	134	142	0.56	17
USA	0.885	134	129	0.56	14
Ukraine	0.915	134	145	0.56	18

It is worthy to note that in both cases, i.e. during the slowing-down process of fast neutrons in natural lead and in ^{208}Pb, mean distance of neutron transport and mean slowing-down time are approximately the same (about 134 cm and 0.56 ms). As for thermal neutrons, mean distances of neutron diffusion till absorption are quite different for two lead types (30 cm in natural lead and 835 cm in ^{208}Pb).

This means that, firstly, very small fraction of neutrons which were slowed down in natural lead reflector can come back into the reactor core. On the contrary, ^{208}Pb reflector gives them such a possibility. Secondly, mean lifetime of thermal neutrons in the infinite ^{208}Pb environment (0.6 s) is longer by three orders of magnitude than that in natural lead (0.8 ms). So, main process in ^{208}Pb reflector is a neutron slowing-down, not neutron absorption, and these slow neutrons, after a diffusion (and time delay), have a probability to come back into the reactor core and sustain the chain fission reaction. Mean lifetimes of slow neutrons and, especially, thermal neutrons are substantially longer than those for fast and slowing-down neutrons. This constitutes a potential for significant extension of mean prompt neutron lifetime in the chain fission reaction.

It is noteworthy that neutron-physical parameters of radiogenic lead extracted from thorium and thorium-uranium ore deposits in Brazil, Australia, USA and Ukraine are inferior to those of ^{208}Pb but they are substantially better than those of natural lead. For comparison, Table IV presents relevant data for heavy water and graphite. Some neutron-physical parameters of these materials are superior to those of ^{208}Pb. However, the use of heavy water or graphite as a neutron reflector in a fast reactor is a doubtful option, at least, because such a neutron reflector can substantially soften neutron spectrum in the reactor core with all negative consequences.

In order to find out to what extent the theoretical prerequisites on potential advantages of ^{208}Pb as a neutron moderator, coolant and reflector are well-grounded, the lifetime of prompt neutrons in the fast reactor core (simplified model) has been estimated.

Neutron-physical calculations have been performed using the software package TIME26[7], where one-dimensional model of fast reactor in 26-group diffusion approximation is considered. Evaluated nuclear data file BNAB-78 was used, which was processed by auxiliary software package ARAMAKO-C1 (preparation of self-shielded micro-constants for every reactor zone).[8] Mean lifetime of prompt neutrons is a bilinear fractional functional of neutron flux and its adjoint function in the reactor as a whole including neutron reflector.

In the course of physical calculations, three reactor models were used that did not differ in the main parameters of the core (fuel type, coolant, fuel cladding, contact layer, fuel assembly materials). They differed only in the diameter of the core, in the thickness of blanket, in it content, also to equalizing the radial heat distribution, they have different enrichments. And so, our models:

First: have the same core as a BN-600 and the same size of blanket (30 cm), but there is no fertile fuel and fuel assembly materials in the blanket, there is only natural lead in it

Second: have the same core as a BN-600, there is no fertile fuel and fuel assembly materials in the blanket, the thickness of it changed from 30 cm to 300 cm and there is only 208Pb

Third: this model is identical to the second model in content, there is only one difference: radius of core changed from 100 cm to 20 cm. We named second and third model, concerning to its sizes of core “large” and “small” reactors respectively.

As indicated above, the core of the first two models is the same, their difference only in the reflector in blanket and in its thickness. To get the effect of slowing down of different reflectors we measured the neutron spectrum in the 5 cm thick layer in the blanket region close to the core. To compare with these two models, BN-600 was also considered as a variant of the "absence" of the reflector (see Hist. 1).

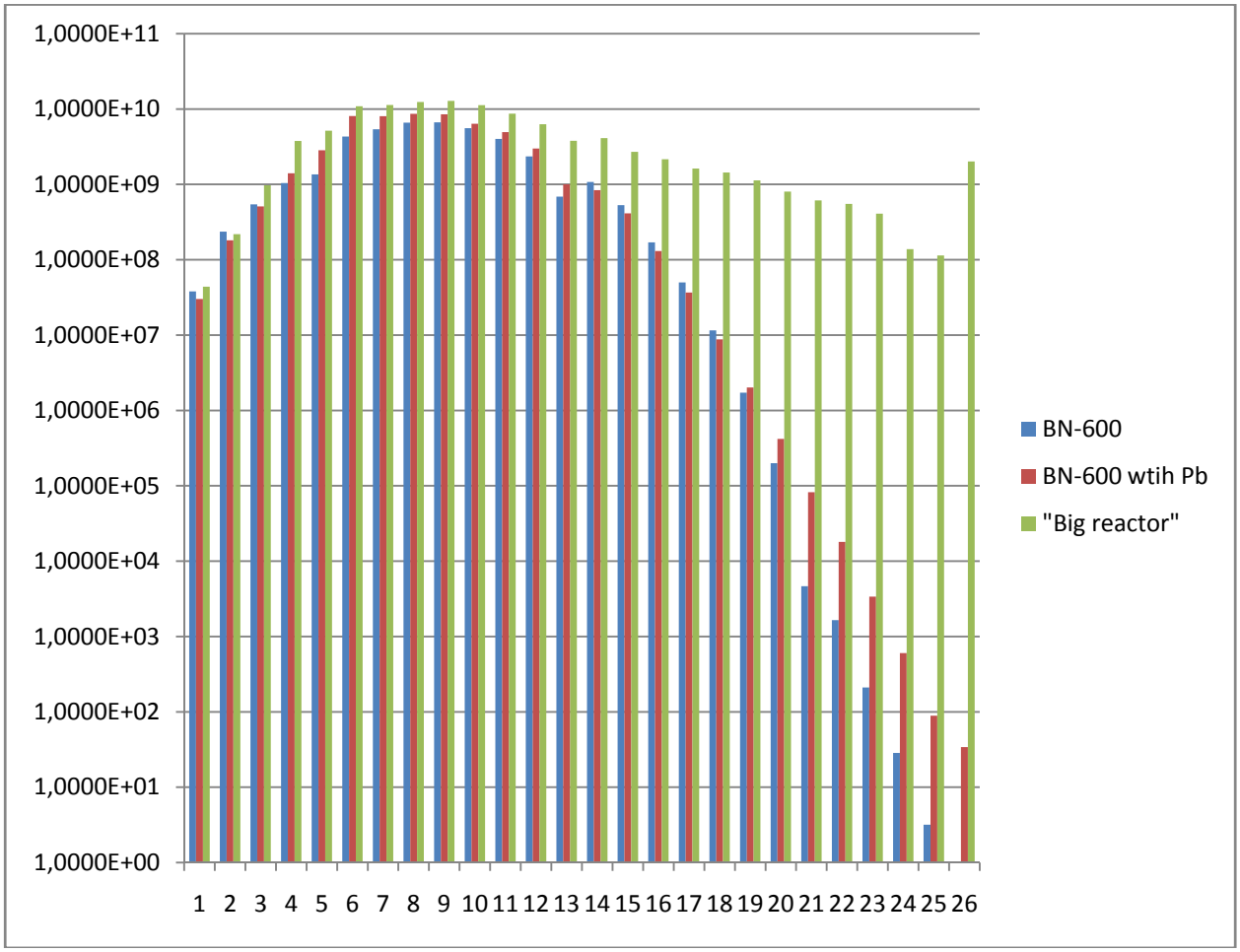

Hist. 1. Neutron spectrum on the edge core-blanket

III.A. Impact of Reflector Parameters on Fission Distribution and Neutron Spectrum

In hist.1 energy of neutrons distributed into 26 groups from fast to thermal spectrum. As can be seen on the histogram, in the blanket layer close to core region of the "large" reactor, the number of epithermal neutrons is much larger than in the same layers of the BN-600 and the reactor with the natural lead reflector. Neutrons can come to this layer from the core and from the depth of the reflector. Neutrons coming into this layer from the core are mostly fast, because they are formed as a result of the fission reaction, when epithermal neutrons in a larger amount may appear here only due to slowing down in the

reflector. Simply put, the same number of neutrons passes from the core to blanket in all three reactors, but only in the "large" reactor their significant number slows down to epithermal energies and come back, due to the good moderating ability of radiogenic lead. This is explained by the fact that in lead-208 the mean distances of thermal neutron diffusion till absorption (835 cm) [9] are larger than the thickness that we have (300 cm) in the reflector.

So, main process in ^{208}Pb reflector is a neutron slowing-down, not neutron absorption, and these slow neutrons, after a diffusion (and time delay), come back into the reactor core and sustain the chain fission reaction.

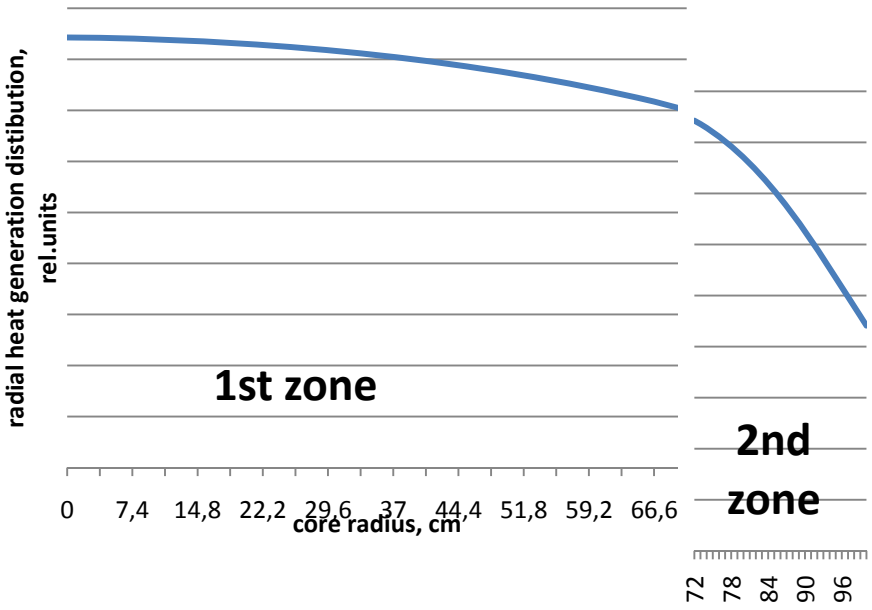

Figrку 4 - Radial heat generation distribution in the core of reactor with natural lead

Thick reflector with effective neutron slowing-down can increase slow neutron flux from reflector to the reactor core and, as a consequence, increase heat generation rate on the core boundary (edge) that can we see in the figures 4,5,6.

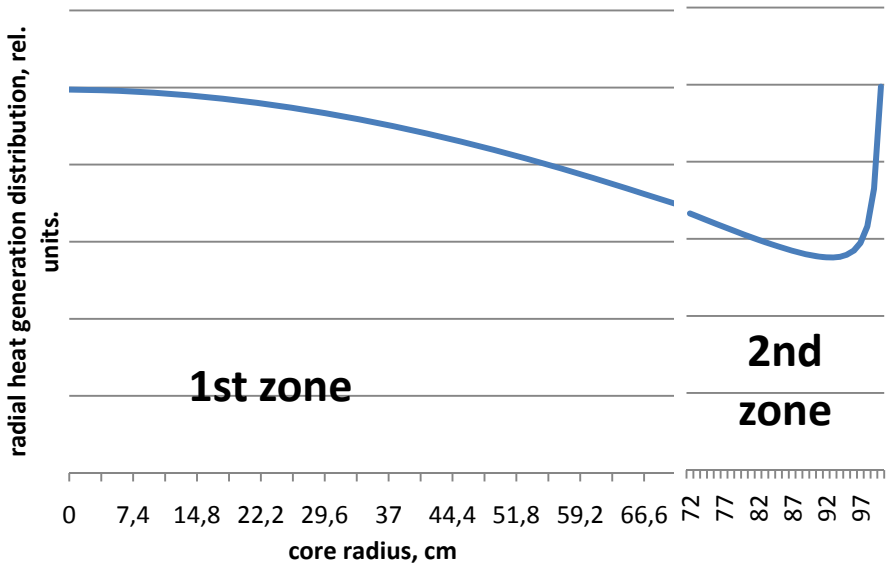

Figrку 5 - Radial heat generation distribution in the core of “big” reactor

This confirms once again that, as is supposed, neutrons coming back from reflector into the reactor core are slow neutrons indeed.

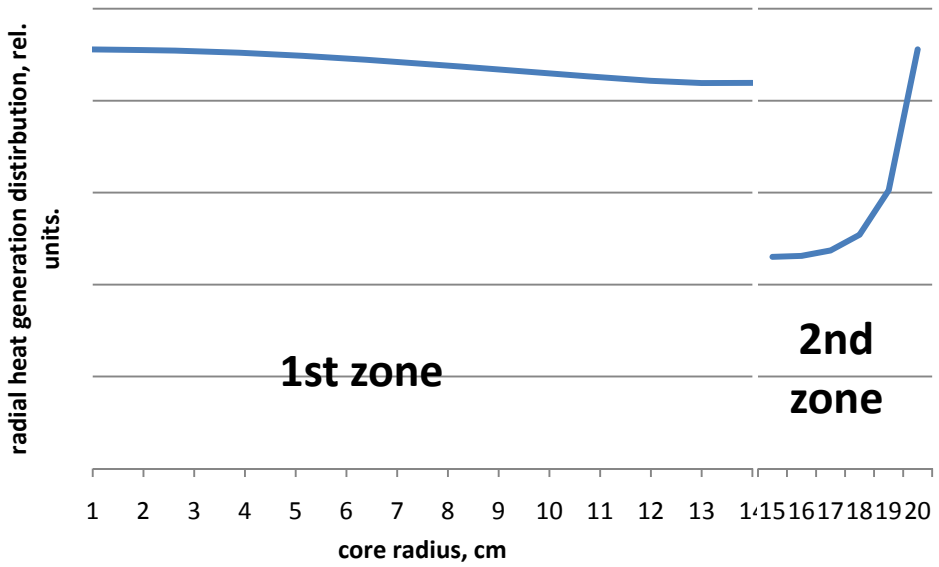

Figure 6 - Radial heat generation distribution in the core of "small" reactor.

Thick (3 m) ^{208}Pb reflector can soften neutron spectrum in center of the fast reactor core. The spectral softening effect can be illustrated by variations of a universal spectral index α(^{239}Pu), i.e. ratio of energy-averaged radiative capture cross-section to energy-averaged fission cross-section, in the core center and on the core edge, that defines, to a large extent, fuel breeding properties of fast reactors. The spectral indices in the core center are equal to 0.243 for thin (30 cm) neutron reflector made of natural lead (1st model) and 0.243 for thick (3 m) neutron reflector made of ^{208}Pb (2nd model), i.e. there is no spectral softening effect in the core center.

More impressive spectral softening effect takes place on the core edge (2nd zone) : α(^{239}Pu) increases from 0.229 to 0.282, i.e. on 23%. Splash of heat generation rate in "large" and "small" reactors weakened by decreasing content of fissile materials in layer of fuel rods adjacent to the core edge.

Table V - Enrichment in zones of reactors with different reflectors

Model of reactor	Content of plutonium fraction, %	
	1st zone	2nd zone
BN-600 with natural Pb	14.30	18.29
«Big» reactor	14.82	13.91
«Small» reactor	30.12	13.91

The spectral softening effect in the core may be regarded insignificant. Hence, application of thick neutron reflector made of heavy material is not able to soften radically neutron spectrum in the reactor core, thus remaining the reactor in the category of fast reactors on its spectral parameters. This is a principal conclusion because the prolongation of prompt neutron lifetime is based, to a large extent, upon deep penetration of neutrons into the reflector, and thermal neutrons are not able to do it

III.B. Dependence of prompt neutron lifetime on thickness of various reflectors

So, with a good reflector and moderator around core we must observe increasing in the value of mean prompt neutron lifetime Λ_{prt}. For example, value of such parameter in BN-600 reactor is about 2,79*10^{-7} s. Replacement of fertile fuel in blanket (0.3m) by natural lead (1st model), changed the prompt neutron lifetime to 2,86*10^{-7} s. Replacement of fertile fuel in blanket by ^{208}Pb (2st model), i.e. use the last one as a neutron reflector and moderator and change thickness of ^{208}Pb reflector from 0.3 m to 3 m , extended prompt neutron lifetime to 1,4*10^{-4}, i.e. by ~500 times.

Such a drastic extension of mean prompt neutron lifetime is caused by the following effect. Fast neutrons from the reactor core penetrated deeply into ^{208}Pb reflector, multiple neutron-nucleus collisions slowed down these neutrons and they came back to the reactor core after an essential time delay (due to small absorption and effective albedo of ^{208}Pb). Since these returning neutrons, in the terms of their origin, are prompt neutrons, it can be spoken about the slowed progression of chain fission reaction on prompt neutrons.

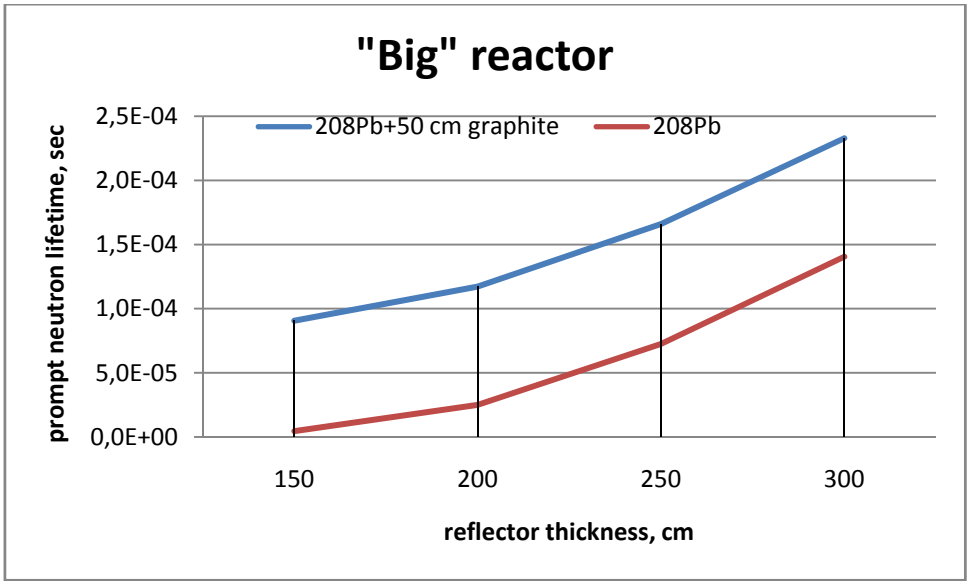

Figure 7 - Dependence of prompt neutron lifetime on thickness of various reflectors in “big” reactor

Dependence of mean prompt neutron lifetime on thickness of neutron reflector from ^{208}Pb is shown on fig 7,8. As neutron reflector thickens from 150 cm to 300 cm, mean prompt neutron lifetime increases approximately 30 times in a “large” reactor and 42 times in a “small” reactors.

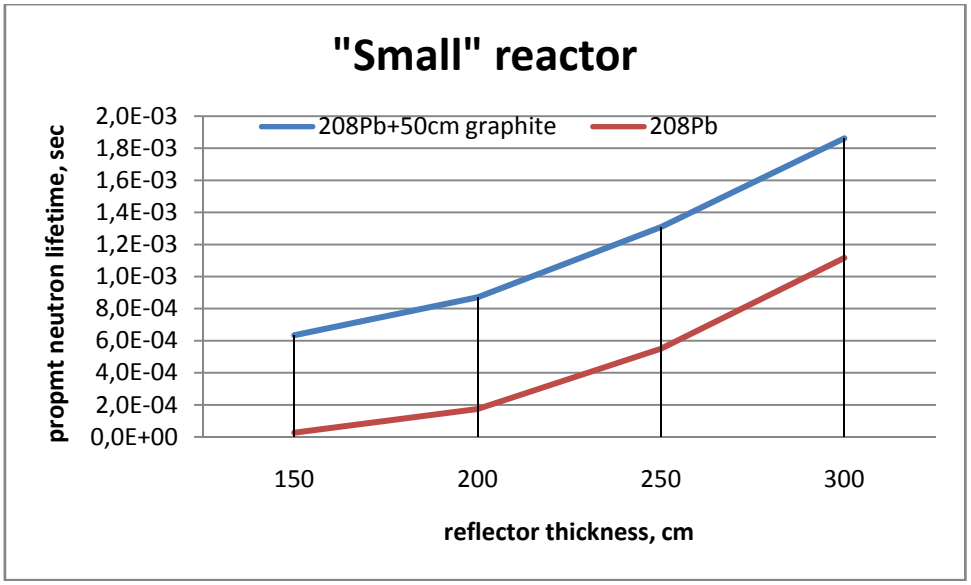

Figure 8 - Dependence of prompt neutron lifetime on thickness of various reflectors in “small” reactor

Noteworthy that mean prompt neutron lifetime becomes longer and doesn’t reach plateau even with noticeably large reflector thicknesses (3m). This is explained by the fact that in lead-208 the mean distances of thermal neutron diffusion till absorption (835 cm), and its mean lifetime longer by several orders of magnitude than mean lifetime of fast and slow neutrons.

III.C. Some other methods for increasing the value of mean prompt lifetime

Also, we can prolong mean prompt neutron lifetime by placing a graphite layer (0,5 m thick) behind ^{208}Pb reflector (3 m) (fig 7,8). In this case, small neutron fraction can diffuse through thick reflector and reach graphite. Graphite, as a good neutron moderator and reflector, provides effective neutron slowing-down, and then slow neutrons can come back to the reactor core. Using only graphite as a reflector in blanket of fast reactors can lead to such a significant softening of the neutron spectrum in the core that it is become thermal. It should be noted that application of the combined neutron reflector (^{208}Pb and graphite) can substantially reduce demands for needed quantity of ^{208}Pb.

On the other hand, to increase prompt neutron lifetime we need that the slow neutrons returning from reflector back to reactor core should be effectively involved in chain reaction through fission. Accordingly, in the core region closed to reflector it's preferable to apply fissile nuclide with small value $\alpha=\sigma_c/\sigma_f$. As such nuclide we placed ^{233}U in that zone of core where we have heat splash. As a result, in a "large" reactor the value of this parameter decreased from 0,338 to 0,103, and in a "small" from 0,337 to 0,105. It certainly influenced on mean prompt lifetime. As you see in a "large" reactor it increased by 14,7%, and in a "small" - by 17,8%.

Besides, soften neutron spectrum in the outer region of reactor core closed to reflector will improve Doppler effect of reactor.

IV. MATHEMATICAL MODELS OF NEUTRON KINETICS IN THE FAST REACTOR WITH THICK REFLECTOR

The longer lifetime of prompt neutrons can substantially improve kinetic response of the fast reactor to insertion of relatively large (about \$1 or even more) positive reactivity. For simplicity, let effective fraction of delayed neutrons β be the same for all the fast reactor models under consideration here and equal to $\beta(^{235}U) = 0.0065$.

As is known, if relatively large positive reactivity jump occurred, then an asymptotic power excursion period is mainly defined by lifetime of prompt neutrons in chain fission reaction. If you consider dependencies of the asymptotic period on the reactivity jump of reactors with different values of lifetime of prompt neutrons. You see the shorter lifetime of prompt neutrons results in the faster power excursion at the same reactivity jump. It means that the reactor safety can be enhanced by making lifetime of prompt neutrons longer.

IV.A. One-Point Model

Dependencies of the asymptotic period on the reactivity jump can be obtained by using one-point model of neutron kinetics with six groups of delayed neutrons, without accounting for any feedback effects. This mathematical model can be described by the following set of differential equations[11]:

$$\frac{dN(t)}{dt} = \frac{\rho-\beta}{\Lambda_{prt}}N(t) + \sum_{i=1}^{6}\lambda_i C_i(t)$$

$$\frac{dC_i(t)}{dt} = \frac{\beta_i}{\Lambda_{prt}}N(t) - \lambda_i C_i(t); \quad (i=1,.,6), \tag{1}$$

where N – neutron population in the reactor core; C_i – quantity of nuclei-emitters for i-th group of delayed neutrons in the reactor core; ρ - reactivity, $\rho=(K_{ef}-1)/K_{ef}$, where K_{ef} – effective neutron multiplication factor in the reactor including neutron reflector; β - effective fraction of delayed neutrons; β_i – effective fraction of delayed neutrons in i-th group; Λ_{prt} – generation time of prompt neutrons in the reactor including neutron reflector; λ_i – decay constant of nuclei-emitters for i-th group of delayed neutrons.

Lifetime τ and generation time Λ_{prt} of prompt neutrons are linked by the following relationship: $\tau=K_{ef}\cdot\Lambda_{prt}$. Since only critical and nearly critical (within some dollars from criticality) states are analyzed here, lifetime and generation time differ insignificantly. These terms are regarded below as equivalent ones.

Within the frames of one-point kinetic model (1), the "inverse-hour" equation that links the asymptotic period of the power excursion T with the inserted positive reactivity ρ may be written in the following form:

$$\rho = \frac{\Lambda_{prt}}{T} + \sum_{i=1}^{6} \frac{\beta_i}{1+\lambda_i T} \quad . \qquad (2)$$

IV.B. Two-Point Model

As it is noted [12], one-point model is not completely applicable for characterization of neutron kinetics in the reactor cores surrounded by neutron reflector. The associated problems are analyzed [12-18] with application of multi-point models or with introduction of some additional (fictive) groups of delayed neutrons. The latter case takes into account the following new parameters: time of neutron staying in the reactor core before leakage, time for neutron transport from the reactor core to neutron reflector, time of neutron staying in the reflector, time for neutron transport from the reflector into the reactor core, time from neutron arrival in the reactor core to initiation of fission reaction by this neutron. In this case, neutron reflector is placed in the immediate vicinity to the reactor core, and the reflector is thick from physical point of view. This means that time of neutron staying in the reflector plays a dominant role in competition with all other times. If one additional group of delayed neutrons, namely slow neutrons coming back from the reflector into the reactor core, is introduced to study the reflector-induced effects on neutron kinetics, then the following set of equations may be written:

$$\begin{aligned}
\frac{dN(t)}{dt} &= \frac{\rho-\beta-\rho_R}{\Lambda_C} N(t) + \sum_{i=1}^{6} \lambda_i C_i(t) + \lambda_R C_R(t) \\
\frac{dC_i(t)}{dt} &= \frac{\beta_i}{\Lambda_C} N(t) - \lambda_i C_i(t), \qquad (i = 1,.,6) \qquad (3) \\
\frac{dC_R(t)}{dt} &= \frac{\rho_R}{\Lambda_C} N(t) - \lambda_R C_R(t), \quad \lambda_R = \frac{1}{\Lambda_R} \ ,
\end{aligned}$$

where:C_R – quantity of fictive nuclei-emitters for additional group of delayed neutrons, i.e. for neutrons coming back from the reflector into the reactor core where they can initiate fission reactions. For brevity, this parameter may be called as a quantity of fictive nuclei-emitters in the reflector;

$\rho_R = (K_{ef} - K_{ef}^C)/K_{ef}$ – reactivity gain caused by the reflector, i.e. increase of reactivity caused by neutrons coming back from the reflector to the reactor core and subsequent initiation of additional fission reactions. For brevity, this parameter may be called as a reactivity gain caused by the reflector;

K_{ef} – effective neutron multiplication factor in the reactor including neutron reflector (like as in one-point model;

K_{ef}^C – effective neutron multiplication factor in the reactor without neutron reflector;

Λ_C – generation time of prompt neutrons in the reactor without neutron reflector;

Λ_R – generation time of prompt neutrons caused by the reflector-induced effects. This generation time is a sum of neutron lifetime in the reactor core, time of neutron staying in the reflector and neutron lifetime in the reactor core after coming back from the reflector. For brevity, this parameter may be called as a generation time of prompt neutrons in the reflector.

According to the set of equations (3), additional group of delayed neutrons, that simulates neutron diffusion in the reflector, can be characterized by its effective fraction, i.e. contribution of the reflector into reactivity, and by its decay constant, i.e. inverse generation time of prompt neutrons in the reflector. The "inverse-hour" equation, that links the asymptotic period T with the inserted positive reactivity ρ, can be written in the following form for the reactor core surrounded by neutron reflector:

$$\rho = \frac{\Lambda_C}{T} + \frac{\rho_R}{1+T/\Lambda_R} + \sum_{i=1}^{6} \frac{\beta_i}{1+\lambda_i T} \quad . \qquad (4)$$

This equation differs from similar "inverse-hour" equation (2) in one-point model (1) by the second summand that describes the role of neutron reflector. Besides, the first summand of the "inverse-hour" in one-point model contains lifetime of prompt neutrons in the reactor as a whole, including neutron reflector, while the first summand of the "inverse-hour" equation in the model with additional group of

delayed neutrons contains generation time of prompt neutrons in the reactor core without neutron reflector. Generation time of prompt neutrons in the reflector Λ_R can be calculated from the following balance relationship [12]:

$$\Lambda_{prt} = (1-\rho_R)\Lambda_C + \rho_R\Lambda_R , \qquad (5)$$

where Λ_{prt} (like one-point model) – generation time of prompt neutrons in the reactor with neutron reflector. The balance relationship defines generation time of prompt neutrons in a system as a sum of generation times of prompt neutrons in all system's components (in the reactor core plus in the reflector, for instance) with the weighing coefficients which characterize contributions of these components into total criticality.

It may be concluded from equation (4) that ρ_R plays here a role of additional fraction of delayed neutrons that is characterized by Λ_R, generation time of prompt neutrons in the reflector. This means, in its turn, that application of such a thick neutron reflector gives a new quality to the reactor – the larger fraction of delayed neutrons and, as a consequence, slowing down of chain fission reaction.

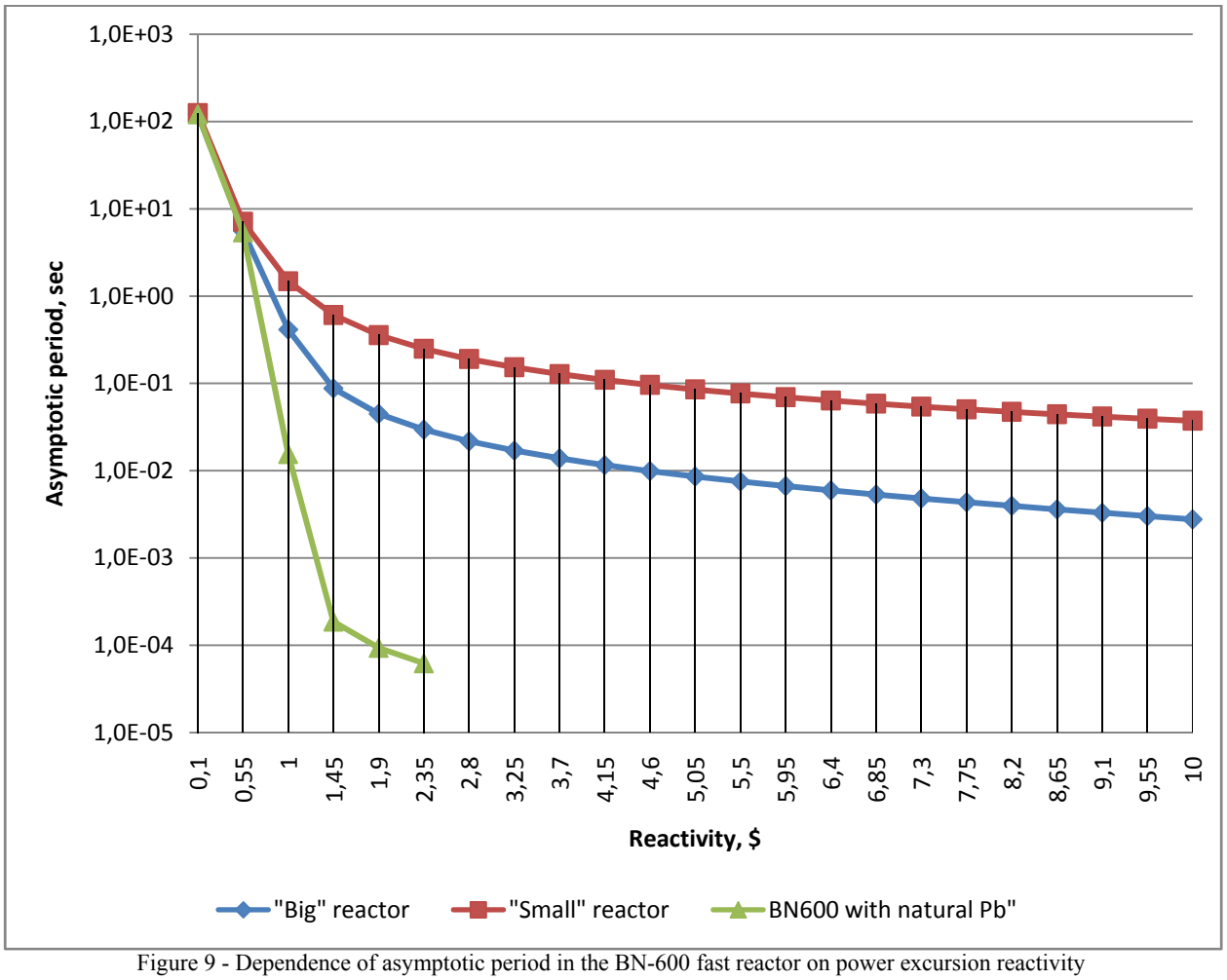

Figure 9 - Dependence of asymptotic period in the BN-600 fast reactor on power excursion reactivity for different sizes of core and different reflectors

One else important circumstance consists in the following fact. The larger fraction of delayed neutrons depends mainly on neutron leakage from the reactor core and, thus, may be chosen as a developer wills, while fraction of nuclei-emitters of delayed neutrons may be chosen only within very stringent constraints. Evidently, generation rate of these "delayed" neutrons substantially depends on

leakage rate of fast and resonance neutrons from the reactor core. That is why application of thick neutron reflector is a reasonable option not only for fast reactors but also for the reactors with resonance and even thermal spectra, i.e. for the reactors with significant leakage of fast and resonance neutrons from the reactor core.

The "inverse-hour" equation (4) for the reactor core surrounded by neutron reflector with additional group of delayed neutrons coincides with the "inverse-hour" equation in two-point model [12]. And we used this equation to consider dependencies of the asymptotic period on the reactivity jump of our three types of reactor . As shown in the figure 9 If reactivity is well below \$1 there is no difference in asymptotic periods of reactors. However, if reactivity approaches or exceeds \$1, difference in the values of an asymptotic periods of reactors that have ^{208}Pb in the blanket ("small" and "large") and do not have (reactor with natural lead in the blanket) reaches several orders of magnitude. For example, when we inserted the same reactivity \$1,45 into the reactor core of all three types of reactor the difference in values of this parameter of "large" reactor and reactor with natural lead in the blanket becomes 2,5 orders of magnitude. For "small" reactor this difference of values becomes 3 orders. This big difference can only be explained by the presence of a three-meter reflector contains ^{208}Pb.

If positive reactivity ρ = \$1 is inserted into the fast reactor BN-600 (neutron reflector – natural lead, 0.3 m thick), then asymptotic power excursion period is equal to 14 ms. If the same reactivity is inserted into the supposed "large" reactor (have the same core as a BN-600, neutron reflector – ^{208}Pb, 3 m thick), then asymptotic power excursion period is equal to 410 ms, if into supposed "small" reactor (have the same core as a BN-600, but radius reduced from 100cm to 20 cm, neutron reflector – ^{208}Pb, 3 m thick) then – 1480 ms! This means that power of the fast reactor BN-600 with natural lead in the blanket increases in a second by 29 orders of magnitude (in fact, this is an explosion) while power of the fast "large" reactor increases in a second eleven-fold and power of the fast "small" reactor increases in a second two-fold only. Such a time interval (one second) may be long enough for partial heat removal from fuel by coolant, and the opportunity arises for actuation of coolant temperature feedback. It may be concluded that the use of thick ^{208}Pb reflector in a fast reactors can upgrade substantially their nuclear safety. The review is stinted with analysis of hypothetical transients without accounting for any feedbacks.

V. SUMMARY AND CONCLUSIONS

All the results presented above allowed us to make the following conclusions:

1. the use thick (3 m) ^{208}Pb reflector in fast reactors can considerably prolong mean lifetime of prompt neutrons (on three orders of magnitude) that can substantially improve nuclear safety even if positive reactivity above \$1 is inserted into the reactor core;
2. the use of combined ^{208}Pb-graphite reflector can shorten ^{208}Pb layer with such spectral parameters that allow to regard the reactor as a fast one;
3. the presence of a three-meter reflector contains ^{208}Pb, leads to the fact that the asymptotic period of reactor with such reflector exceeds the same parameter of reactor with same core and conventional reflector by 2,5-3 orders of magnitude

So, fast reactor with reflector contains ^{208}Pb will be more stable to inserted positive reactivities even above \$1 than it will be without it.

REFERENCES

[1] Shmelev A. N., Kulikov E. G., Kulikov G. G., Apse V. A. Lead Containing Mainly Isotope ^{208}Pb – a Neutron Moderator, Coolant and Reflector of Neutrons. Its Neutron-Physical Properties // Proc. Int. Conf. Physics of Reactors (GLOBAL'2011), Makuhari, Japan, December 11-16, 2011.

[2] Kulikov G. G., Shmelev A. N., Apse V. A., Kulikov E. G., and Artisyuk V. V. Radiogenic Lead with Dominant Content of ^{208}Pb: New Coolant and Neutron Moderator for Innovative Nuclear Facilities // Internet Hindawi journal Science and Technology of Nuclear Installations, Article ID 252903. 2011. doi: 10.1155 /2011/252903.

[3] Godoy J. M., Godoy M.L., Aronne C. C. Application of Inductively Coupled Plasma Quadrupole Mass Spectrometry for the Determination of Monazite Ages by Lead Isotope Ratios // Journal of Brazilian Chemical Society, vol 18, 5, 2007.

[4] Nier A. O., Tompson R. W., Murphey B. F. The Isotopic Constitution of Lead and the Measurement of Geological Time // Physical Review, vol 60**,** 1941.

[5] HOLMES A. The Pre-Cambrian and Associated Rocks of the District of Mozambique // Quarterly Journal of Geological Society, vol 74, 1918.

[6] Sarkar T. C. The Lead Ratio of a Crystal of Monazite from the Gaya District, Bihar // Proc. Indian Academy Sciences, Vol. 13, 1941, pp. 245-248.

[7] Catalog of Isotope Dates for Minerals of Ukrainian Shield // Naukova Dumka, Kiev, USSR. 1978. pp. 90-137.

[8] Shibata K., Iwamoto O., Nakagawa T., et al. JENDL-4.0: a New Library for Nuclear Science and Engineering // Nuclear Science and Technology, vol 48, 1, 2011.

[9] Grigoriev I. S., Meylikhov E. Z. Physical Values. Reference Book // Energoatomizdat, Moscow, USSR, 1991.

[10] Galanin A. D. Introduction to a Theory of Thermal Nuclear Reactors // Energoatomizdat, Moscow, USSR, 1990.

[11] HUMMEL H. H., Okrent D. Reactivity Coefficients in Large Fast Power Reactors // American Nuclear Society, LaGrange Park, 1970.

[12] Kolesov V. F. Aperiodic Pulsed Reactors // Sarov, Russian Nuclear Center-VNIIEF, 2007.

[13] Spriggs G. D., Bush R. D. Reflected Reactors: Point Kinetics and Prompt Critical // Proc. Topl. Mtg. Physics, Safety and Applications of Pulsed Reactors, Washington, USA, November 13-17, 1994. pp. 265-273.

[14] Spriggs G. D., Bush R. D., Williams J .G. Two-Region Kinetic Models for Reflected Reactors // Annals of Nuclear Energy, vol 24, 3, 1996.

[15] Cohn C. E. Reflected-reactor kinetics // Nuclear Science and Engineering, vol 13, 1, 1962.

[16] Gamble D. P. The Effect of Reflector-Moderated Neutrons on the Kinetics of the Kinetic Experiment Water Boiler // Trans. Am. Nucl. Soc., vol 3, 1, 1960.

[17] Coats R. L., Long R. L. Reflector and Decoupling Experiments with Fast Burst Reactors // Proc. National Topl. Mtg. Fast Burst Reactors, Albuquerque, USA, January 28-30, 1969.

[18] Avery R. Theory of decoupled reactors // Proc. 2nd Int. Conf. Peaceful Uses Atomic Energy, Geneva, Switzerland, Vol. 12, 1958. pp. 182-191.

Б.Қ. Қожахмет[1], Г.Г. Куликов[2], Г.С. Нурбакова[1]

[1]Әл-Фараби атындағы Қазақ ұлттық университеті, Алматы, Қазақстан
[2]Ұлттық зерттеу ядролық университеті "МИФИ", Мәскеу, Ресей

^{208}Pb НЕГІЗІНДЕ НЕЙТРОН ШАҒЫЛДЫРҒЫШЫН ҚОЛДАНУ АРҚЫЛЫ БН-600 ШАПШАҢ РЕАКТОРДЫҢ НЕЙТРОНДЫҚ – ФИЗИКАЛЫҚ СИПАТТАМАЛАРЫН ЖАҚСАРТУ

Аннотация. Нейтрон шағылдырғышы және баяулатқышы ретінде әдетте атом салмағы кіші материалдар қолданады (жеңіл және ауыр су, графит және т.с.). Атом салмағы ауыр жаңа баяулатқыш ұсынылуда – ^{208}Pb изотопы бойынша байытылған радиогендік қорғасын. Ол өте кішкентай радиоактивті қармау қимасына (жылулық нейтрон үшін ~0.23 мбарн, яғни дейтерий мен графиттегі көрсеткіштерден де төмен) және жылулық нейтрондар үшн жоғарғы альбедоға ие.

Алдынғы жұмыстарда шапшаң реакторда радиогенді қорғасын қолдану арқылы лездік нейтрондар тізбекті бөліну реакциясын баяулату мүмкіндігі көрсетілген. Бұл шапшаң реактордың қауіпсіздігін арттыруы мүмкін.

Осы жұмыста бұндай шағылдырғыштың БН-600 шапшаң реакторының нейтрондық-физикалық сипат-тамаларына әсері зерттелген.

Еске алармық маңызды мәселе, ^{208}Pb мөлшері көбіректеу радиогенді қорғасынды торий кенорындарынан изотопты бөлінусіз өндіруге болатынын Сан – Пауло университетінде (Бразилия) эксперименталды зерттеулермен дәлелденген.

Түйін сөздер: шапшаң реактор қауіпсіздігінің арттыруы**,** лездік нейтрондар өмір сүру уақытының ұзаруы, ^{208}Pb негізінде нейтрон шағылдырғышы, БН – 600 шапшаң реакторы.

Б.К. Кожахмет[1], Г.Г. Куликов[2], Г.С. Нурбакова[1]

[1]Казахский национальный университет имени аль-Фараби, Алматы, Казахстан
[2]Национальный исследовательский ядерный университет "МИФИ", Москва, Россия

УЛУЧШЕНИЕ НЕЙТРОННО – ФИЗИЧЕСКИХ ХАРАКТЕРИСТИК БЫСТРОГО РЕАКТОРА БН – 600 ПУТЕМ ИСПОЛЬЗОВАНИЯ ОТРАЖАТЕЛЯ НЕЙТРОНОВ НА ОСНОВЕ ^{208}Pb

Аннотация. Как правило, в качестве замедлителей и отражателей нейтронов используются материалы с малым атомным весом (легкая и тяжелая вода, графит и т.д.). Предлагается новый очень тяжелый по атомному весу замедлитель – радиогенный свинец, содержащий главным образом изотоп 208Pb. Он характеризуется чрезвычайно низким сечением радиационного поглощения нейтронов (~0.23 мбарн для тепловых нейтронов, т.е. меньше, чем у графита и дейтерия) и наибольшим альбедо тепловых нейтронов.

В предыдущих работах было оценено, что использование радиогенного свинца позволяет замедлить цепную реакцию деления на мгновенных нейтронах в быстром реакторе. Это может улучшить безопасность быстрого реактора.

В данной работе изучено влияние такого рода отражателя на нейтронно – физические характеристики быстрого реактора БН – 600.

Важно заметить, что радиогенный свинец с большим содержанием в нем свинца-208 может быть добыт в месторождениях ториевых руд (а также торий-урановых руд) без изотопного разделения, что экспериментально подтверждено исследованиями, выполненными в Университете Сан Пауло (Бразилия).

Ключевые слова: улучшение безопасности быстрого реактора, увеличение времени жизни мгновенных нейтронов, отражатель нейтронов на основе ^{208}Pb, быстрый реактор БН – 600.

N E W S
OF THE NATIONAL ACADEMY OF SCIENCES OF THE REPUBLIC OF KAZAKHSTAN
PHYSICO-MATHEMATICAL SERIES
ISSN 1991-346X
Volume 4, Number 320 (2018), 36 – 41

UDC 523.62

G.S. Minasyants[1], T.M. Minasyants[1], V.M. Tomozov[2]

[1]Fesenkov Astrophysical Institute, Almaty, Kazakhstan;
[2] Institute of Solar-Terrestrial Physics, Irkutsk, Russia
E-mail: gennadii_minasya@mail.ru, gennadii_minasya@mail.ru, tom@iszf.irk.ru

FIP EFFECT MANIFESTATION FEATURES IN CORONAL MASS EJECTIONS

Abstract. FIP effect manifestation features in coronal mass ejections are investigated. For the analysis observational data from SC ACE (SWICS device) spacecraft were used in an ion energy range (0.5-100) keV/e. In addition to the values of the relative content of Fe/O, an indicator was obtained that characterizes the degree of ionization of iron and oxygen ions Q(Fe), Q(O). To quantify the values of the parameters Q(Fe) and Fe/O, their mean values were calculated in the six-hour interval during the time period of these indexes. A comparison of the values of Q(Fe) and Fe/O showed that for Fe ions less than +13 there is practically no change in Fe/O with increasing Q(Fe). But with Q(Fe) ≥13, the manifestation of the FIP effect is sharply increased, due to the increase in the relative contents of Fe ions. Probably, due to the penetration of an energetic flare plasma into the body of the outbursts, when they develop together in the corona of the Sun, a significant increase in the degree of ionization of the Q(Fe) ions occurs. As a result, the Fe/O index can be used as an indicator of the possible presence of flare plasma in the coronal mass ejection charge structure.

Keywords: solar activity, coronal mass ejections, energy spectra, FIP effect, Fe/O ratio.

Introduction

Flares and coronal mass ejections (CME) are primary active processes on the Sun which influences on state of interplanetary environment and Earth's magnetosphere. According to a modern conceptions flare and CME may be consider as a unified process connected with an equilibrium violation of magnetic structure owing to free magnetic energy build-up in an active region. While energy releases of accumulated magnetic energy in flare dissipation regions (current sheets) it occurs a fast plasma heating and particle acceleration to a high energy [1-3]. Besides, a high-velocity CME (CME masses can reach up to 10^{15} - 10^{16} g and their velocities can exceed 2000 km/sec) are capable to generate a shock waves which can accelerate of particles effectively, when flare plasma flows move near the Sun and in interplanetary medium.

It is noted that in flare evolution a part of hot flare plasma can to penetrate into CME ejection body and then the observed spectrum of accelerated particles has a composite character. In this connection values of minor element ratio Fe/O play an important role which is consequence of FIP effect manifestations (FIP- first ionization potential) because this particle population accelerated by flare is a highly enriched Fe (Fe/O>1). On the contrary, particles accelerated by shock waves are depleted by Fe (Fe/O<1).

The composition of minor elements in the photosphere, fairly reliably determined by spectroscopic methods, is completely homogeneous over the entire visible solar surface; however, the abundance of admixtures in structural formations of the solar corona and solar wind appears to differently depend on FIP relative to their concentrations in photosphere. It has been established that the admixtures are fractionated according to FIP in the upper solar chromosphere. Elements with low FIP (<10 eV – Fe, Mg, Si, K, etc.) are easily ionized and carried away under driving the ponderomotive force of alfven waves to the upper solar atmosphere [4,5] where these ions are able to accumulate largely in the central parts of closed magnetic structures of active regions. Driving mechanism on minor ions by ponderomotive force of alfvenic waves was proposed by Laming [5] and in a present time it is considered as a most likely mechanism as far as it has ability to explain FIP effect manifestations not only in solar corona but in stars coronae too. Alfven waves are generated at footpoints of loop magnetic field structures under random

plasma motions in photospheric layers and may be generated in magnetic reconnection regions also. Minor elements with a high FIP (>10 eV – C, N, O etc.) remain neutral in chromospheric layers and their abundances does not change because their ionization occurs in high-temperature coronal layers only. Consequently, the ratio value Fe/O in different coronal structures and in solar wind has a various values and it may be considering as an indicator of physical processes in solar plasma. In the first time the FIP effect manifestations in solar corona was established spectroscopically by Pottasch [6].

Recently, new results have been obtained on the evolution and distribution of impurity elements in the structures of solar active regions. Observations from the Hinode/EIS satellite have shown that impurity elements with low FIP potential can accumulate in the upper parts of the loop structures with strong fields in the central zones of active regions [7]. At the periphery of the active regions, the magnetic reconnection process with the emerging small-scale magnetic fields with a photospheric composition prevents the accumulation of elements with a low potential of FIP. As a result of the "exchange" magnetic reconnection, plasma with a reduced composition of elements with a low FIP goes beyond the active regions and can manifest itself in a slow solar wind [8].

Detailed observations also showed that the composition of the elements in the hot plasma evaporating during large X-ray flares is close to the photospheric composition [9]. At the same time, the composition of ions in the plasma of CME emissions associated with such outbursts turns out to be a highly enriched element with a low potential of FIP and a high degree of ionization. Such emissions are called "compositionally hot" CME emissions [8]. It is noted that such CME emissions are injected from the central parts of active regions. In observations of the phenomena of pulsed heating in the solar transition region, a plasma composition close to the photospheric composition was also found. In contrast, the fan of the overlying coronal loops showed enrichment with elements of low FIP potential [10]. These authors concluded that the composition of the plasma can serve as an important sign of coronal heating. Naturally, the FIP effect is also manifested in the composition of energetic particles accelerated by flares and ejections, therefore some characteristics will be described here.

Based on the results of the analysis of 54 solar cosmic ray events (SCL) (November 1994-June 2012) in the energy range of 2-15 MeV/n, Reames [11] concluded that the main cause of variations in the abundances of heavy ions in the interplanetary medium, and, consequently, changes in the ratio of Fe / O is their scattering by Alfven waves, which depends on the magnetic stiffness of the particles. This process occurs during the propagation of particles from the region of acceleration due to shock waves caused by CMEs. Alfven waves in the solar wind are excited by vigorous protons and impurity ions themselves, which are accelerated both in flares and in shock waves from the CME [11]. Fe ions are scattered by Alfven waves less efficiently than oxygen ions, therefore, in the case of propagation in a turbulent medium, iron ions outstrip oxygen ions, which leads to registration of Fe / O> 1 ratios.

Thus, in this paper, some features of the manifestations of the FIP effect in the composition of CME will be described in terms of the characteristics of the ratio of Fe / O in the CME structures and the degree of ionization of Fe.

Processing of the observation data

For the research purposes, 17 CME (1998-2006) were selected, which had a pronounced front shock front with the highest confidence level - Shock4 (according to SOHO classification). All CME emissions belonged to the structural type "halo". In the course of propagation of CMEs in the corona and interplanetary medium, the magnetic structure of the ejection expands after the forward shock wave. The turbulent region of compressed plasma immediately behind the front of the shock wave is characterized by strong variations of the components of the interplanetary magnetic field B, increased values of the proton density N_p, their velocity V_p and temperature T_p [12]. Behind the area of turbulent compression (shell) is the actual "body" of the ejection. The data describing the time boundaries of each of the CME structures were taken in the "Wind ICME Catalog".

In the earlier work Minasyants et al. [13], Fe/O energy spectra were calculated in seven different energy intervals for the CME structures representing magnetic clouds with the help of the Fe and O energy spectra. The value of the Fe/O ratio in the region of turbulent plasma compression in the entire ion energy range remains less than unity, which indicates that the Alfven turbulence of the oxygen ions is weak, which have a high FIP value. In the magnetic cloud region in the energy range (0.2-0.6) MeV/n, the

Fe/O ratio is much higher and in some cases even exceeds unity. This may be due to the amplification of scattering by Alfven waves or to the effect of preferential accumulation of ions with a low ionization potential in a magnetic cloud before ejection.

To investigate the structure of the emissions, in addition to the values of the Fe/O index, an indicator was obtained that characterizes the degree of ionization of elements, including iron and oxygen ions. The hourly average values of these parameters, as well as the velocities of Fe ions (for the charge state Q= +10) and O (for the charge state Q= +6) were taken in the ACE spacecraft database (SWICS device)-all observations refer to the energy interval (0.5-100) keV/e.

To quantify the values of Q(Fe) and Fe/O, their mean values were calculated in the six-hour interval during the period of increase in the time profiles of these parameters (Table 1).

Discussion of results and conclusions

The following figure shows the changes in the O and Fe ion velocities with time, their degree of ionization Q(O), Q(Fe), and the relative Fe/O content for CMEs that resulted from the development of powerful events - solar cosmic ray bursts (GLE). Vertical dashed lines from left to right show: the arrival of the shock wave front (UV) CME, followed by the region of turbulent plasma compression (shell), between the second and third dashed lines - the "body" of ejection.

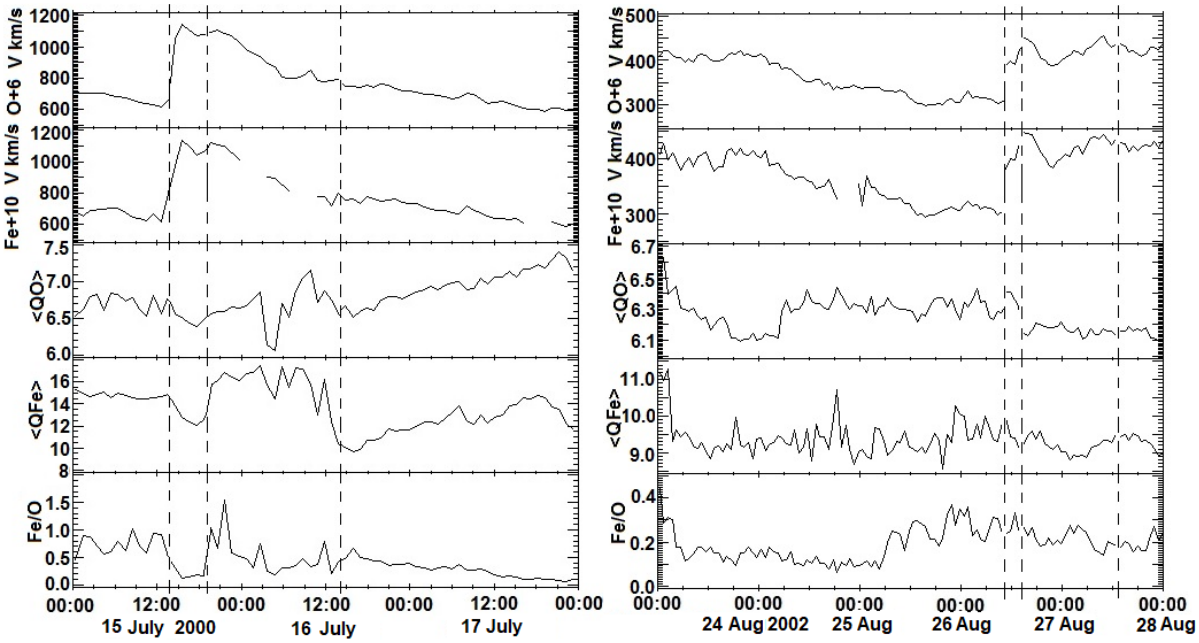

Figure 1 - Time changes with physical parameters in the structures of CMEs on July 15-16, 2000 and August 26-27, 2002

It is noted that the manifestation of the FIP effect associated with an increase in the relative content of Fe ions with respect to O ions is enhanced in those cases when ions with increased charge states Q(Fe) are present in the plasma of the CME emission (July 15-16, 2000). For the CME event, on the 26-27 August 2002, on the contrary, the values of the degree of ionization of the Q (Fe) ions, and, in fact, the lower, actually background values, and, accordingly, the Fe/O ratio does not show such amplification. It is likely that this testifies to the absence of more energetic flare plasma in the structure of the coronal ejection.

Consideration of temporal changes in parameters for all selected CMEs indicates their individual properties associated with the composition of the plasma in the ejection, which manifests itself in different values of the degree of ionization of Q(Fe), Q(O) ions, and their relative Fe/O content. In order to quantify the values of the parameters Q(Fe), Fe/O in each CME, their mean values were calculated over a six-hour interval during the period of increase in the time profiles of these indices.

One more feature in the CME emission structure was noticed. The region of turbulent compression, which is characterized by high values of the plasma parameters V, N_p, B, T, associated with the shock wave of the CME, as a rule, does not show the growth of the parameters Q(Fe), Q(O), Fe/O. This

indicates a weak efficiency of scattering of ions by Alfven turbulence in this region (the turbulence of Alfven waves exist behind the shock wave).

Table 1 shows the time of passage of all structural elements for the CMEs considered: the front of the shock wave, the region of turbulent compression (shell), and the actual ejection body. For the plasma of the considered emissions, in separate columns of the table, the electric field strength is E^-, the charge states of the iron ions are Q(Fe) and the iron ion content with respect to oxygen is Fe/O with error averaging.

Table1 - The passage time of the structural elements of the CME and the values of the electric field parameters, the degree of ionization of iron ions and the ratio of Fe/O in the release plasma

№	Arrival of CME Shock	Shell End/Frontal part of CME body	CME End	E, mV/m	Q(Fe)	Fe/O
1	04:20.08.11.1998	08:00.08.11.	23:31.08.11.	7.09±0.16	13.18±0.18	0.37±0.05
2	14:17.15.07.2000	19:10.15.07.	14:30.16.07.	21.61±6.89	16.80±0.18	0.81±0.17
3	18:19.11.08.2000	06.05.12.08.	05:05.13.08.	14.55±1.19	14.92±0.17	0.63±0.04
4	00:14.31.03.2001	12:00.31.03.	02:00.02.04.	15.47±2.14	15.58±0.19	0.79±0.13
5	23:57.17.04.2001	06:20.18.04.	07:20.19.04.	4.28±1.53	10.35±0.06	0.23±0.02
6	04:28.28.04.2001	17:59.28.04.	04:48.02.05.	-	15.99±0.11	0.88±0.10
7	02:33.28.10.2001	11:00.28.10.	03:17.30.10.	5.92±0.43	14.36±0.89	0.40±0.05
8	05:51.24.11.2001	15:47.24.11.	13:17.25.11.	5.38±3.45	13.26±0.32	0.53±0.06
9	04:08.23.04.2002	07:11.24.04.	23:59.24.04	0.44±0.07	11.37±0.07	0.18±0.01
10	10:20.26.08.2002	14:23,26.08.	13:40.27.08.	2.46±0.41	9.41±0.07	0.27±0.01
11	05:51.29.10.2003	11:16.29.10.	10:00.30.10.	-	16.31±0.25	0.79±0.15
12	16:00.30.10.2003	04:30.31.10.	23:00.02.11.	-	16.77±0.20	1.20±0.23
13	05:53.04.11.2003	14:00.04.11.	12:00.06.11.	0.87±0.05	9.74±0.07	0.16±0.01
14	18:24.09.11.2004	20:38.09.11.	16:47.10.11.	15.80±0.85	13.87±0.18	0.64±0.08
15	16:48.21.01.2005	23:45.21.01.	19:12.22.01.	1.75±0.60	12.23±0.28	0.21±0.07
16	02:19.15.05.2005	04:17.15.05.	22:47.16.05.	22.51±7.16	16.34±0.19	0.89±0.09
17	13:57.14.12.2006	22:36.14.12.	13:40.15.12.	12.43±0.50	16.31±0.10	0.51±0.10

A comparison of the values of the degree of ionization of Q (Fe) ions and the relative content of iron ions to Fe/O oxygen in the CME plasma is shown in Fig. 2. At Fe ions less than 13, practically no Fe/O changes with Q (Fe) increase are observed. But for Q (Fe) ≥ 13, the manifestation of the FIP effect is sharply increased, due to an increase in the relative content of Fe ions. This is probably due to the presence of flare plasma in the body of emissions.

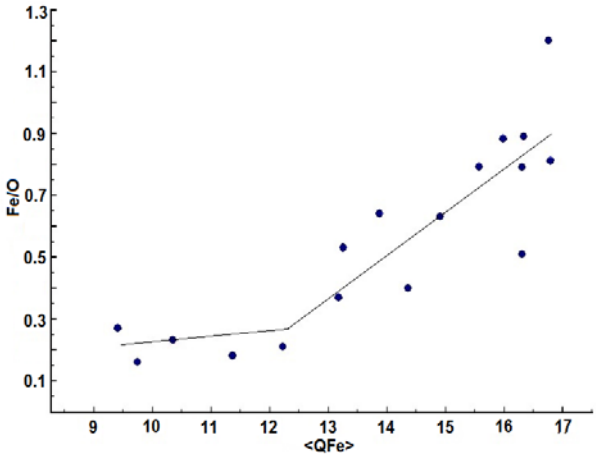

Figure 2 - Degree of Fe ionization versus Fe/O values for considered CME events.

The obtained result agrees well with the conclusions of Zurbuchen et al. [8], devoted to the study of the relative contents of various elements in the structures of a number of CMEs, where a tendency was established to enhance the effect of the FIP effect upon the growth of the charge state of Fe ions.

A special study was devoted to the identification in the CME structure of a correlation relationship between changes in the values of individual physical parameters V, B, N_p, E^-, T^o K and Fe/O, Q(Fe) values. Of all the parameters considered, the best correlation with changes in Q(Fe) and Fe/O in the plasma of coronal discharges is shown by the values of the electric field strength E, which have a natural relationship with the electron density (Fig. 3).

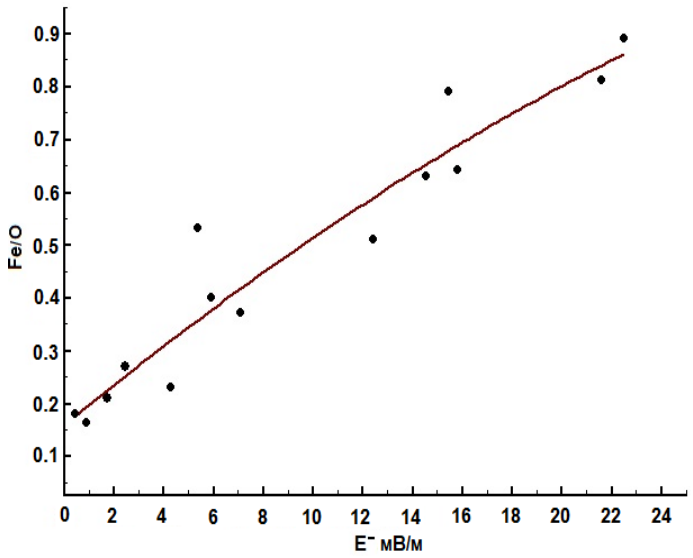

Figure 3 - The dependence of the electric field strength E^- mV/m on the relative content of iron and oxygen ions Fe/O from observations in the plasma of coronal mass ejections

Thus, the most probable reason for the enhancement of the values of Q(Fe) and, respectively, of Fe/O, is the penetration into the body of the ejection of an energetic flare plasma significantly enriched by electrons in the initial phase of their joint development. Based on the observational data described in the Introduction, it can be concluded unambiguously that "composite hot" CME emissions are injected from the central parts of the active regions. It is there, at the tops of the loops, the accumulation of elements with a low potential of FIP. In the process of ejection and associated outbreaks, strong electric fields appear in this region, and hot and dense plasma is produced, with accelerated electrons. Naturally, multiply charged ions are strongly affected by electric fields, so the observed increase in the Fe/O ratio can be explained. As a result, the Fe/O ratio can be used as an indicator of the possible presence of flare plasma in the coronal ejection structure.

Acknowledgements

The authors are grateful to the teams of scientists who supervise the experiments on space vehicles ACE, WIND, SOHO and for providing observational data on the Internet.

The work is supported by the Targeted Financing Program BR05336383 of the Aerospace Committee of the MDAI of the Republic of Kazakhstan. The work of V.M.T. was performed with budgetary funding of Basic Research program II.16.

REFERENCES

[1] Altyntsev A.T., Banin V.G., Kuklin, Tomozov V.M. Solar Flares. Moscow: Science, -1982. P.246.

[2] Prist E.R., Forbes T. Magnetic reconnection. Magneto-hydrodynamic theory and applications. M.: Fizmatlit, 2005. P.591.

[3] Somov B.V. Plasma Astrophys.: Reconnection and Flares // Springer: New York. 2013. P.504. DOI: 10.1016/S02731177(97)00968-X.

[4] Laming J.M. A unified picture of the first ionization potential and inverse first ionization potential effects // Astrophys. J. 2004. V. 614. P. 1063–1072.

[5] Laming J.M. The FIP and inverse FIP effects in solar and stellar coronae. Living reviews in Solar Physics. 2015. V. 12. P. 2.

[6] Pottasch S.R. The lower solar corona: the abundance of iron. MNRAS, 1963. V. 125. P. 543.

[7] Baker D., Brooks D.H., Demoulin P., Yardley S.L., van Driel-Gesztelyi L., Long D.M., Green L.M. FIP bias evolution in a decaying active region. Astrophys. J., 2015. V. 802. P. 104.

[8] Zurbuchen T. H., Weberg M., von Steiger R., Mewaldt R. A., Lepri S. T., and Antiochos S. K. Composition of Coronal Mass Ejections // Astrophys. J., 2016. July 20. 826:10 (8pp),

[9] Warren H.P. Measurements of absolute abundances in solar flares. Astrophys. J. Let. 2014. V. 786. L2.

[10] Warren H.P., Brooks D.H., Doschek G.A., Feldman U. Transition region abundance measurements during impulsive heating events. Astrophys. J., 2016. V. 824, P. 56.

[11] Reames D.V. Element abundances in solar energetic particles and the solar corona // Solar Phys. 2014. V. 289. P. 977-993.

[12] Ermolaev Yu.I., Ermolaev M.Yu. Solar and interplanetary sources of geomagnetic storms: aspects of space weather // Geophysical processes and biosphere. 2009. T.8. № 1. P. 5-35.

[13] Minasyants G.S., Minasyants T.M., Tomozov V.M. The change in Fe/O ratio with the energy of ions in structures of Magnetic Clouds during the development of powerful geomagnetic storms // Selected problems of astronomy. Materials of the All-Russian Astronomical Conference. Irkutsk. 2016. P. 186-196.

Г. Минасянц[1], Т. Минасянц[1], В. Томозов[2]

[1]В.Г. Фесенков атындағы Астрофизикалық институт, Обсерватория-23, Алматы, Қазақстан;
[2]Күн-Жер Физикасы институты, ул. Лермонтова 126-а, Иркутск, Россия

МАССАНЫҢ КОРОНАЛДЫ ШЫҒАРЫЛУЛАРЫНДА FIP-ӘСЕРДІҢ КӨРІНУІНІҢ ЕРЕКШЕЛІКТЕРІ

Аннотация. Массаның короналды шығаруларында FIP-әсердің көрінуінің ерекшеліктері зерттелді. Өңдеулер үшін иондар (0.5-100) кэВ/е энергиясы диапазонында ACE (SWICS аспабы) ғарыш аппараты бақылауларының мәліметтері пайдаланылды. Fe/O салыстырмалы құрамы мәнінен басқа темір және оттегінің Q(Fe), Q(O) иондарының иондану дәрежесін сипаттайтын көрсеткіш тартылды. Q(Fe) және Fe/O параметрлерінің мәнінің сандық бағалауы үшін бұл индекстердің уақытша бағыттарының артуы кезеңінде алты сағаттық интервалда олардың орташа мәні есептелді. Fe иондары зарядтары кезінде Q(Fe) және Fe/O мәндерін салыстыру Q(Fe) өсуімен Fe/O шамасының өзгеруі +13 –ден азырағы бақыланбайды. Бірақ Q(Fe) ≥13 кезінде Fe иондар құрамы салыстырмалы артуымен байланысты FIP-әсердің көрінуі кенет күшейеді. Күн тәжінде олардың бірлескен дамуы кезінде мүмкін шығарулар денесіне энергиялық жарқыл плазманың енуі нәтижесінде, Q(Fe) иондарының иондану дәрежесінің айтарлықтай артуы болады. Нәтижесінде индекс Fe/O индексін короналды шығарулары құрылымында жарқыл плазманың болу мүмкіндігімен индикатор ретінде пайдалануға болады.

Түйін сөздер: күн белсенділігі, массаның короналды шығарылуы, энергия спектрлері, FIP – әсер, Fe/O қатынасы.

УДК 523.62

Г. Минасянц[1], Т. Минасянц[1], В. Томозов[2]

[1]Астрофизический институт им. В.Г. Фесенкова, Обсерватория-23, Алматы, Казахстан;
[2]Институт Солнечно-Земной Физики, ул. Лермонтова 126-а, Иркутск, Россия

ОСОБЕННОСТИ ПРОЯВЛЕНИЯ FIP-ЭФФЕКТА В КОРОНАЛЬНЫХ ВЫБРОСАХ МАССЫ

Аннотация. Изучены особенности проявления FIP-эффекта в корональных выбросах массы. Для обработки использовались данные наблюдений на космическом аппарате ACE (прибор SWICS) в диапазоне энергий ионов (0.5-100) кэВ/е. Кроме значений относительного содержания Fe/O был привлечен показатель, характеризующий степень ионизации ионов железа и кислорода Q(Fe), Q(O). Для количественной оценки значений параметров Q(Fe) и Fe/O были рассчитаны их средние значения в шестичасовом интервале в период повышения временных профилей этих индексов. Сопоставление значений Q(Fe) и Fe/O показало, что при зарядах ионов Fe, меньших +13 практически не наблюдается изменений величины Fe/O с ростом Q(Fe). Но при Q(Fe) ≥13 резко усиливается проявление FIP-эффекта, связанное с увеличением относительных содержаний ионов Fe. Вероятно, благодаря проникновению энергичной вспышечной плазмы в тело выбросов, при их совместном развитии в короне Солнца, происходит значительное увеличение степени ионизации ионов Q(Fe). В результате, индекс Fe/O можно использовать в качестве индикатора возможного присутствия вспышечной плазмы в структуре коронального выброса.

Ключевые слова: солнечная активность, корональные выбросы массы, спектры энергии, FIP – эффект, отношение Fe/O.

Information about authors:
Minasyants Gennady Sergeevich - Fesenkov Astrophysical Institute, Leading Researcher, gennadii_minasya@mail.ru;
Minasyants Tamara Mihailovna - Fesenkov Astrophysical Institute, Senior Researcher, gennadii_minasya@mail.ru;
Tomozov Vladimir Mihailovich - Institute Solar-Terrestrial Physics, Senior Researcher, tom@iszf.irk.ru.

N E W S
OF THE NATIONAL ACADEMY OF SCIENCES OF THE REPUBLIC OF KAZAKHSTAN
PHYSICO-MATHEMATICAL SERIES
ISSN 1991-346X
Volume 4, Number 320 (2018), 42 – 47

UDC 524.31

V. M. Tereschenko

Fesenkov Astrophysical Institute
volter2307@mail.ru

SPECTROPHOTOMETRIC STANDARDS 8^M- 10^M. 1. EQUIPMENT, METHODS AND FIRST RESULTS

Abstract. Justification of the task of creation a network the spectrophotometric of standards 8^m-10^m is given. Standards of this brightness are necessary for calibration of spectral observations using large telescopes. Selection of stars – candidates in spectrophotometric standards and primary standards was made. As candidates in the standards selected stars of spectral classes A and B which are located in the equatorial zone with declination ±3˚. The used equipment - a new CCD spectrograph is briefly described. Dispersing element of a spectrograph is the concave toroidal grating which simultaneously serves as collimator and as camera. The spectrograph operates in the slitless mode. As the receiver of radiation the CCD camera ATIC-490EX was used. The new spectrograph allows to investigate an energy distribution in the spectra of much dimer stars than in case of observations with spectrometers. Observations on the telescopes AZT-8 and Zeiss-600 at Kavenskoe plato carry out. The differential method of observations was used. Processing of CCD-spectrograms and numerical reductions detail is described. The energy distribution in spectral region 340 – 660nm is investigated, spectral resolution of the obtained data be 5 nm, the relative standard deviation - from 3 to 6%. The absolute energy distribution in spectra of two candidates for standards is presented.

Key words: stars, **s**pectrophotometric standards, CCD-spectrograph, method of observations.

Introduction. Study of energy distribution in the spectra of stars is the traditional subject of the Fesenkov Astrophysical Institute. The created in the institute spectrophotometric catalogue of stars [1] continues to be the most voluminous in the world. The spectral energy distribution is used to determine the physical parameters of stars and interstellar medium. In addition, stars with a known distribution of energy are used for standardization of spectrophotometric observations of diverse celestial objects and for calibration of equipment. Usually as the spectrophotometric standards serve stars of the early classes. In their spectra be available the extend ranges that is free from strong spectral lines. Spectrophotometric data is present in two forms: "unbroken" and "porous". In "unbroken" form data about spectral outside atmosphere illumination are presented continuously through a certain interval. This interval equals to interval of the averaging of intensities. Thus illumination was presented in histogram form. In "porous" form data are given for selected wavelengths. At present, unbroken energy distribution (integral spectrum) for more than 1500 stars studied. Almost all of them are brighter 6^m [1-6]. In the literature and in the database SIMBAD, there are several tens stars-standards 7^m - 8^m [7-10] and only a few - weaker.

The standards should be as much as possible, since from their numbers is influenced performance observation and accuracy of data. Obviously, observations at large telescopes require weaker standards. Therefore, adding to the available weak standards of even a few stars makes sense and task of creating weak spectrophotometric standards is relevant. It can be said that their creation is an "eternal" task, since over time weaker standards, more accurate, with higher spectral resolution and in a wider range of the spectrum are required. We decided to expand the list of standards toward weaker ones compared to thouse available in catalogues of stars and create network spectrophotometric standards 8^m-10^m. The present work is the first of a planned series of publications devoted to its creation.

The equipment. Energy distribution in the spectra of stars in the above papers [1-10] was obtained using singlechannel spectrometers, in which photomultipliers served as the radiation. For the study of

energy distribution in the spectra of stars 8m-10m we specially made spectrograph [11], in which the radiation receiver is a CCD camera. We emphasize that we have not encountered special studies of the energy distribution in the spectra of stars with the help of CCD spectrographs.

Apparently, the lack of such studies is due not so much to the loss of their relevance as to the methodological difficulties that arise in their implementation.

It is worth noting that the accuracy of recording the radiation fluxes of a CCD camera is lower compared to photomultipliers. Nevertheless, the binding of spectral observations of a variety of celestial objects obtained with CCD spectrographs to standard stars in certain sections of the spectrum is quite often performed (see, for example, [12-13]). In our spectrograph for absolute measurements (SAM) a dispersive element is a toroidal diffraction grating. The constant of grating - 150 strokes/mm, the size of the shaded part of the grating - 20 * 20mm, the focal length - approximately 242mm. The dispersion of spectrograph is 25nm/mm, field size - 20 mm. Spectrograph runs essentially in a slitless mode. Entrance slit has a width of about 1 mm, which is clearly larger than the image of star in telescope with a focal length less than 20m. A wide slit and diaphragm is required for absolute measurements - so that there is no vignetting of the beam. Since the spectral resolution of the data is only 5 nm, the gapless version is quite acceptable. The main advantage of the grating used is that it provides a flat spectrum in the range from 300 to 800 nm. This property allows us to use the CCD-matrix as a radiation receiver. As the radiation receiver is a CCD camera ATIK-490EX. The main parameters of the matrix of this camera are the following: the number of pixels is 3380 * 2704, the size of pixels is 3.69 * 3.69 microns, the length of the matrix is 12.5 mm. The camera cooling is 25K below the air temperature, the spectral sensitivity range is from 320 to 860mk, the reading noise is 5 e. A detailed description of the spectrograph is given in [11]. Notice, that the SAM was originally designed to operate with 1 Zeiss-1000 telescope (1: 10 aperture light) located in the high-altitude TSAO. In connection with the installation of optical reducers on these telescopes, observations were made on the telescopes AZT-8 and Zeiss-600, located on the Kamenskoye Plateau. On the plateau, the transparency of the atmosphere is worse and, accordingly, the accuracy of the obtained data turned out to be lower than expected. One of the drawbacks of SAM is that the size of the matrix of the camera used does not allow us to simultaneously cover all the available area of the spectrum. When replacing the CCD camera with a larger one, the SAM will be eliminated.

Table 1 - List and characteristics of stars - candidates in weak spectrophotometric standards.

Hip (Tyc)	HD (BD)	α 2000	δ 2000	V	B-V	Sp
1241	1112	$00^h\ 15^m\ 27.3^s$	-03° 39' 15"	9.105^m	-0.066^m	B9V
9152	12021	01 57 56.1	-02 05 58	8.843	-0.071	A0
13917	18571	02 59 16.8	01 14 40	8.632	+0.038	A0V
18243	24520	03 54 07.0	02 11 02	8.626	+0.118	B9
20778	28190	04 27 03.5	04 16 51	9.021	+0.125	B9V
24053	289997	05 10 07.8	-00 16 58	9.964	+0.077	B8V
29258	42334	06 10 08.7	00 42 36	9.327	+0.025	B8III
32634	50087	06 51 40.6	00 19 36	9.084	+0.047	B9III
38123	63367	07 48 44.4	01 56 21	8.990	+0.060	B9V
Tyc210-680	BD+01 2119	08 32 43.6	00 53 49	10.13	-0.07	A0
48704	86027	09 55 59.6	02 47 55	8.356	-0.029	A0V
55011	97917	11 15 48.3	-02 17 58	8.880	-0.145	B9
Tyc281-353	BD+01 2668	12 13 25.3	01 09 22	10.29	-0.09	B5?
66872	BD+02 2711	13 42 19.0	01 30 18	10.263	-0.11	B5
Tyc317-603	BD+02 2790	14 14 25.9	01 47 58	10.11	0.03	A0
74972	136161	15 19 14.7	-02 10 02	8.891	0.330	A3V
82133	151355	16 46 47.0	02 12 34	8.826	-0.092	B4/5V
87417	162628	17 51 52.6	02 53 59	8.258	0.192	B9.5V
92559	174648	18 51 41.0	-01 45 35	8.827	0.118	B9.5V
Tyc479-625	185296	19 38 21.0	01 30 14	9.741	0.210	B9II
101541	BD-03 4950	20 34 43.6	-02 41 44	10.010	+0.141	A0
Tyc 531-232	BD+01 4436	21 10 11.5	02 14 20	9.99	+0.03	A0
112149	215112	22 42 58.0	-02 40 57	8.240	-0.041	B9V
Tyc 581-756	BD+02 4661	23 23 38.20	02 55 57	10.05	0.38	F2

The selection of candidate stars in standards and primary standards. As weak spectrophotometric standards, we selected 24 stars of the early spectral classes of 8^m-10^m , located uniformly along the equator ($\delta = \pm 3^\circ$). This choice is due to two factors: the spectra of these stars have extended spectral regions that are free of strong lines and can be used as standards for observations in both hemispheres of the Earth. Naturally, the basic requirement for any standards must be met - they must be unchanged. The list of candidate stars in the standards is presented in Table 1.

The brightest candidate for standards is the star HD 151355 ($V = 8.25^m$), the weakest one is BD + 02 2711 ($V = 10.37^m$). The absolute majority of the stars in the list meet the requirements. Only one star is located outside the dedicated band and only one star has the spectral class F2. As with the creation of all the catalogs [1-10], observations are performed by a differential method. Stars - candidate in spectrophotometric standards were attached to stars for which the spectral distribution of energy was known in advance (they can be called secondary standards). As the last, 9 A0V stars of 7-8 values from the catalog [1], which are also located in the equatorial region, were taken. Their list and main characteristics are given in Table 2. The absolute distribution for them in the regions occupied by the Balmer lines was preliminarily graphically interpolated. In view of the limited volume of the article, we do not present interpolated data here.

Table 2 - List of the secondary spectrophotometric of standards and their characteristic

№п/п	HD	α_{2000}	δ_{2000}	π(mas)	V	B-V	Sp
1	009716	$01^h\ 35.1^m$	-02° 20'	5.29	7.43^m	0.16^m	A0V
2	023009	03 41.6	-00 10	6.20	8.64	0.21	A0V
3	036117	05 29.5	-00 03	6.09	7.99	0.10	A0
4	075620	08 51.1	00 28	4.01	7.97	0.11	A0V
5	100237	11 32.0	-01 47	3.31	7.34	-0.01	A0V
6	121513	13 55.8	01 31	3.25	8.00	0.11	A0V
7	147470	16 22.9	00 30	7.19	7.67	0.10	A0V
8	185198	19 37.9	01 30	1.60	7.32	0.19	B9.5V
9	216261	22 51.6	-01 49	4.02	8.16	0.16	A0V

Methods of observation and processing. Observations were performed by the method equal heights, which makes it possible to use in the reductions for absorption in the atmosphere the average value of the spectral transparency coefficient for the place of observation. Its values were taken from [11], in which they are given for the summer and winter seasons. The difference of air mass ΔM between the standard records and the candidate for the standards did not exceed 0.10 on the average. Each star was observed from 4 to 7 times. For various reasons (instrumental and atmospheric), some of the spectra records were discarded. The duration of exposures ranged from 100 to 500 seconds. The temperature of the camera and the binning for program and standard stars should be the same. Recording modes of their spectra differ only in exposure.

Stars, for which the absolute energy distribution is obtained by binding to secondary standards, can be called tertiary standards. Briefly describe the procedure for processing frames and the data obtained from them. In detail, it is set out in the instructions that we compiled. The result of observations with SAM are "raw" frames of spectra of stars in the "FIT" format, which must be "brought to the number". An example of one of the received frames is shown in Figure 1. Frames are processed in the "MaxIm DL-6" package in the standard way.

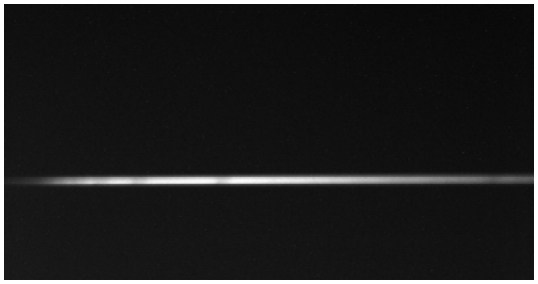

Figure 1 - The spectrogram of HD1112 (9.10^m; B9V)

The first stage of the processing of the captured frames begins with their clearing from the "hot" pixels generated by the matrix defects and cosmic rays. The second stage is the so-called calibration. This is a standard procedure, allowing for the use of additional frames (a flat field, biass and dark) to take into account all the hardware distortions. In our case, a plane field was not recorded because of the uniformity of the matrix used. The third step is subtraction of the background and conversion of frames into a numeric array in the Excel package. As a result, in the computer memory we have a set of numerical values of the charges (impulses) accumulated on the matrix, which are proportional to the fluxes from the stars at the corresponding wavelengths. The Excel program allows you to present it as a graph - a registrogram. The fourth stage is the identification on the register of wavelengths. It is carried out manually, "by eye". The cursor is directed to the center of depression in the spectrum caused by this or that line. For stars of early spectral classes, the Balmer lines of Hα, Hβ and Hγ serve as reference points, for stars of class G - lines H and K. A very important step is the division into 50-angstrom intervals. Dispersion of the spectrograph is practically linear. In our spectrograph 50A corresponds to 25.5 pixels. Due to small spectral shifts at different positions of the spectrograph, the start of the first 50-A interval must be determinate for each frame. A table of numbers of pixel was prepared in advance, corresponding to the beginning and end of the 50-angstrom intervals (template). The monitor marker was exposed to the center of the Hβ line. The number of pixel of center of the line was fixed and the table (template) was shifted to the ultraviolet or red part of the spectrum. The accuracy of the identification is 1-2 pixels (2-5A). For secondary standards, one more operation is required - it is necessary to perform interpolation of the continuous spectrum in the plots of the spectrum occupied by the Balmer lines. Interpolation is carried out after breaking the registrogram into 50-angstrem intervals. Interpolated table values, their values were monitored graphically, "by eye", which requires a certain skill. Because of the shortness of the intervals such an interpolation is carried out quite confidently. Naturally, the manual interpolation method takes considerable time, but in our case this is the best option. An example of a registrogram is shown in Fig. 2.

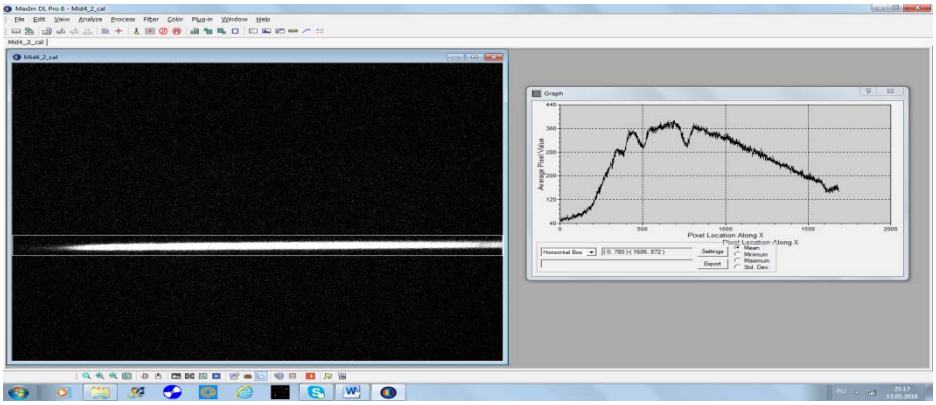

Figure 2 - The registrogram of HD24520 (8.63^{m}; B9)

Numerical reduction. The counts within the 50-angstrom intervals are summed and normalized, that is, the registrogram is converted into a histogram. All calculations and numerical reductions are performed in the Excel package. Reductions for the difference in exposure of the star and the standard and for the different absorption of radiation from them in the Earth's atmosphere are made according to the classical formula of differential spectrophotometry:

$$E^*(\lambda)=E_{st}(\lambda)\times[I^*(\lambda)/I_{st}(\lambda)]\times[\Delta t_{st}/\Delta t^*]\times p_{av}(\lambda)^{-\Delta M}, \quad (1)$$

where $E^*(\lambda)$ and $E_{st}(\lambda)$ are the outside atmospheric values of the spectral densities of the energy illuminations produced by the star and the standard;

$I^*(\lambda)$ and $I_{st}(\lambda)$ are averaged over the 5nm range for the star and the standard (when referenced to two standard entries, the average of the two observations); Δt_{st} and Δt^* - duration of exposures in seconds per standard and star; $p_{av}(\lambda)$ is the average value of the transparency coefficient for the observation site;
$\Delta M = M_{st} - M^*$ - the difference of air masses between the standard and the star.

For secondary standards we took values of monochromatic illumination and corresponding measurements not for the integral spectrum, but for quasi-continuous. For the studied stars, integral readings are taken within the intervals with the same pixel numbers (wavelengths of the centers of 50A intervals).

Table 3 - Распределение энергии в спектрах E(λ) для HD1112 и HD 12021 (единицы - 10^{-7}wt/m^{2}m)

λ, A	1112	12021	λ, A	1112	12021	λ, A	1112	12021
3425	80.5	178	4525	141.6	206	5625	80.1	108
3475	81.8	176	4575	137.0	200	5675	78.7	103
3525	84.9	178	4625	135.0	196	5725	75.2	101
3575	80.5	165	4675	130.6	189	5775	73.5	97
3625	79.9	169	4725	125.4	181	5825	72.0	96
3675	81.8	166	4775	121.9	172	5875	72.4	94
3725	92.8	173	4825	118.0	160	5925	68.8	91
3775	106.1	192	4875	111.3	154	5975	67.4	89
3825	131.0	226	4925	108.8	155	6025	66.4	88
3875	159.6	265	4975	109.3	154	6075	64.7	83
3925	168.1	272	5025	107.0	149	6125	63.2	82
3975	186.1	299	5075	105.2	145	6175	60.4	81
4025	191.3	309	5125	102.2	141	6225	57.5	76
4075	186.8	292	5175	99.7	137	6275	57.8	74
4125	178.6	274	5225	96.3	133	6325	56.2	72
4175	174.2	270	5275	93.6	127	6375	54.8	71
4225	171.6	263	5325	91.0	124	6425	54.5	68
4275	169.2	249	5375	88.4	121	6475	54.4	66
4325	158.8	229	5425	87.7	117	6525	50.5	63
4375	150.0	224	5475	86.9	115	6575	48.0	60
4425	146.4	220	5525	83.5	111	6625	47.0	63
4475	145.0	213	5575	80.5	111	6675	47.5	63

Here we present the results for two stars - the candidates for the standards: HD1112 and HD12021.The outside atmospheric energy distribution in the spectra of these stellar spectrophotometric standards are given in Table 3. The accuracy of the obtained data, characterized by a relative mean-square error, is from 3 to 6%. For stars 9^m-10^m this accuracy of absolute measurements can be considered quite satisfactory.

The work was supported by the funding program BR05236322 of the Ministry of Education and Science of the Republic of Kazakhstan.

REFERENCES

[1] Kharitonov A.V., Tereschenko V. M., Knyazeva L. N. // Spektrofotometrichesky katalog zvezd / Alma-Ata - “Kazak Universiteti”. **2011**. 304 c.

[2] Voloshina I. B., Glushneva I. N., Doroshenko V. T., Kolotilov E. A., Mossakovskaya L.I., Ovchinnikov S.L., Fetisova T.S. Pod red. I.N. Glushnevoy // Spektrofotometriya yarkich zvezd / M. Nauka. **1982**. 256 s.

[3] Alekseeva G. A., Arkharov A. A., Galkin V. D., Hagen-Thorn E. I., Nikanorova I. N., Novikov V. V., Novopashenny V. B., Pakhomov V. P., Ruban E. V., Shchegolev D. E. The Pulkovo spectrophotometric catalog of bright stars in the range from 320 to 1080nm // Baltic astronomy / **1996**. V. 5. № 4. P. 603 - 838.

[4] N. S. Komarov, V. A. Pozigun, S. I. Belik, A. V. Dragunova, V. F. Gopka, N. N. Zakozhurnikova, L. E. Kantsen, V. F. Karamysh, T. V. Mishenina, L. F. Orlova, A.F. Pereverzentsev, T. A. Russo, A. G. Cherkass // Spektrofotometriya zvezd v diapazone λλ550-900nm / Kiev: Naukova dumka. **1983**. 312s.

[5] Komarov N. S., Arkhipov M. G., Basak N. Yu., Belik S. I., Cherkass A.G., Chuprina R. I., Dragunova A.V., Dulapchi I. F., Gorbaneva T. I., Karamysh, V. F., Kantsen L . E., Korotin S. A., Kovtyukh V. V., Orlova L. F., Motrich V.D., Pereverzentsev A.F., Shevchuk T.V., Zakozhurnikova N. N. // The new spectrophotometric star catalogue / Odessa Astronomical Publication. **1998**. V. 11. P. 3 - 48.

[6] Omarov S.Z., Gadzhiev M. S., Goldberg E. P., Omarova G.R., Shestopalov D.I., Shustarev P.N. // Raspredelenie energii v spectrach 425 zvezd / Circular Shamakhinskoy AO im. N. Tusi NAN Azerbaijan. № 104. **2002**. S. 3 - 174.

[7] Hamuy Mario, Walker A. R., Suntzeff N. B., Gigoux P., Heathcote S. R. and Philips M. M. // Southern spectrophotometric standards. I //Publications of the Astronjvical Society of the Pacific. **1992**. V. 104. P. 533 - 552.

[8] Hamuy Mario, Suntzeff N. B., Heathcote S.R.., Walker A.R., Gigoux P., Philips M. M. // Southern spectrophotometric standards. II. // Publications of the Astronomical Society of the Pacific. **1994**. V. 106. P.566 - 589.

[9] Borisov I. N., Glushneva I. N., Shenavrin V. I. // Spectrophotometric standards of 7^m-8^m: suplement 1 //Astrononical and Astrophysical Transactions. **1998**. V. 17. P. 309-320.

[10] Tereschenko V. M. Eqvatorialnye spectrophotometricheskye standarty promezhutochnogo bleska //Astronomichesky zhurnal**. 2002**. T. 79. № 3. S. 249 – 255.

[11] Tereschenko V. M., Shamro A. V. // Spektrograf dlay absoluytnych izmereniy. Skhema i konsrtuktsiay optiko-mekhanicheskogo bloka / Izvestiya NAN RK. **2017**. № 4. C. 152 - 159.

[12] Mironov A.V. // Osnovy fotometriiy / M. Fizmatlit. 2008 - 260s.

[13] Kondrat"eva L. N., Rspaev F. K., Aymuratov E. K. // Rezul"taty spectral"nykh I fotometricheskikh nabluydeniy RS Ophiuchi / Izvestiya NAN RK. - **2015**. - №5. - S. 38 - 43.

[14] Gaysina V.N., Denisyuk E. K., Valiullin R.R. // Zapreschenniye emissionniye liniy v spektrakh Seyfertovskikh galaktik/ Izvestiya NAN RK. **2015**. №5. S. 12-21.

[15] Tereschenko V. M. Spectralny koeffitcient prozrachnosti v rayone Asrofizicheskogo institute v 1970-1971gg // Vestnik AN KazSSR , **1972**, № 3 (324) - S.73 - 76.

УДК 524.31

В. М. Терещенко

«В.Г. Фесенков атындағы Астрофизика институты» ЕЖШС, Алматы, Қазақстан

СПЕКТРОФОТОМЕТРЛІК СТАНДАРТТАР 8^m-10^m. 1. АППАРАТУРА, ӘДІСТЕМЕ ЖӘНЕ АЛҒАШҚЫ НӘТИЖЕЛЕР

Аннотация. 8^m-10^m спектрофотометрлік стандарттардың жүйесін құру міндеттерінің негіздемесі келтірілді. Осы жарқылдың стандарты ірі телескоптарда спектрлік бақылаулардың калибровкасы үшін қажетті. Спектрофотометрлік стандарттардың және алғашқы стандарттардың жұлдыз-кандидаттардың таңдамалары жасалды. Стандарттардың кандидаттары ретінде ±3˚бейімделумен экваторлық аймақта орналасқан А және В спектрлік топтарының жұлдыздары таңдалды. Пайдаланылатын аппаратураның қысқаша сипаттамасы – жаңа ЗБА-спектрограф. Бір уақытта коллиматор және камера болып қызмет атқаратын ойық тороидты тор спектрографтың ыдыратқыш элементі болып табылады. Спектрограф саңылаусыз режимде жұмыс істейді. Сәулелену қабылдағыш ретінде ЗБП-камера ATIC - 490EX пайдаланылады. Жаңа спектрограф энергияның таралуын зерттеуге мүмкіндік береді. Ертеректегі спектрометрмен жұлдыздар спектрлерінде біраз әлсіз. Бақылаулар АЗТ-8 және Цейсс-600 телескоптарында орындалды. Бақылаудың дифференциалдық әдісі пайдаланылды. Спектрограммалармен ЗБА-кадрлар өңдеу процесстері нақтылап суреттелген. Энергияның таралуы 340 - 660нм спектрлік аймақтарда зерттеледі, алынған мәліметтердің спектрлік рұқсаты 5нм құрайды, салыстырмалы с.к.о. - от 3 ден 6% дейін. Стандарттардың екі кандидаттарының спектрлерінде энергияның нақты таралуы ұсынылды.

Түйін сөздер: жұлдыздар, спектрофотометрлік стандарттар, ЗБА-спектрограф, бақылау әдістері.

УДК 524.31

В. М. Терещенко

ДТОО «Астрофизический Институт им Фесенкова», Алматы, Казахстан

СПЕКТРОФОТОМЕТРИЧЕСКИЕ СТАНДАРТЫ 8^m-10^m. 1. АППАРАТУРА, МЕТОДИКА И ПЕРВЫЕ РЕЗУЛЬТАТЫ

Аннотация. Приведено обоснование задачи создания сети спектрофотометрических стандартов 8^m-10^m. Стандарты данного блеска необходимы для калибровки спектральных наблюдений на крупных телескопах. Сделана выборка звезд-кандидатов в спектрофотометрические стандарты и первичных стандартов. В качестве кандидатов в стандарты выбраны звезды спектральных классов А и В, которые расположены в экваториальной области со склонением ±3˚. Кратко описана используемая аппаратура - новый ПЗС-спектрограф. Диспергирующим элементом спектрографа является вогнутая тороидальная решетка, которая одновременно служит коллиматором и камерой. Спектрограф работает в бесщелевом режиме. В качестве приемника излучения используется ПЗС-камера ATIC-490EX. Новый спектрограф позволяет исследовать распределение энергии в спектрах намного более тусклых звезд, чем со спектрометрами. Наблюдения выполнены на телескопах АЗТ-8 и Цейсс-600. Использовался дифференциальный метод наблюдений. Подробно описаны метод обработки ПЗС-спектрограмм и численные редукции. Распределение энергии исследуется в спектральной области 340 - 660нм, спектральное разрешение полученных данных составляет 5нм, относительная с.к.о. - от 3 до 6%. Представлено абсолютное распределение энергии в спектрах двух кандидатов в стандарты.

Ключевые слова: звезды, спектрофотометрические стандарты, ПЗС-спектрограф, методы наблюдений

Information about author:

Tereschenko V.M. - Candidate of Physical and Mathematical Sciences, Fesenkov Astrophysical Institute; volter2307@mail.ru

N E W S
OF THE NATIONAL ACADEMY OF SCIENCES OF THE REPUBLIC OF KAZAKHSTAN
PHYSICO-MATHEMATICAL SERIES
ISSN 1991-346X
Volume 4, Number 320 (2018), 48 – 57

UDC 532.517.4.519.6

***A. Issakhov, A. Abylkassymova, M. Sakypbekova**

al-FarabiKazakh National University,Almaty, Kazakhstan
*e-mail: alibek.issakhov@gmail.com

APPLICATIONS OF PARALLEL COMPUTING TECHNOLOGIES FOR MODELING OF THE WIND FLOW AROUND THE ARCHITECTURAL OBSTACLES WITH THE VERTICAL BUOYANCY FORCES

Abstract. Taking into account the high rate of construction in the modern big cities, it is very important to save the natural aerodynamics between the buildings. It is necessary to explore the ventilation of space between architectural structures, making a preliminary prediction before construction starting. The most optimal way of evaluating is to build a mathematical model of air flow. This paper presents numerical solutions of the wind flow around the architectural obstacles with the vertical buoyancy forces. An incompressible Navier-Stokes equation is used to describe this process. This system is approximated by the control volume methodand solved numerically by the projection method. The Poisson equation that is satisfying the discrete continuity equationsolved by the Jacobi iterative method at each time step.For check correctness of mathematical model and numerical algorithm is solved test problem. The numerical solutions of the backward-facing stepflow with the vertical buoyancy forces, which was compared with the numerical results of other authors. This numerical algorithm is completely parallelized using various geometric domain decompositions (1D, 2D and 3D). Preliminary theoretical analysis of the various decomposition methods effectiveness of the computational domain and real computational experiments for this problem were made and the best domain decomposition method was determined. In the future, a proven mathematical model and parallelized numerical algorithm with the best domain decomposition method can be applied for various complex flows with the vertical buoyancy forces.

Keywords: domain decomposition method, flow around the architectural obstacles, backward-facing step flow, projection method, vertical buoyancy forces, mixed convection.

1 Introduction

The increased pace of construction in modern large cities and, in particular, Almaty, leads to a tightening of architectural structures. Due to the increase in the population of cities and to save space, mostly high-rise multi-storey buildings are being built. As a consequence, this entails such consequences as a violation of the natural aerodynamics of the city, which in turn leads to increased gas contamination of the city, the accumulation of heavy metals in the lower atmosphere, and to the violation of the local climate. The building codes and norms currently used in the construction and design of buildings do not contain aerodynamic criteria and coefficients indicating the optimal distance between buildings of different heights. When determining these standards, various natural and climatic features are taken into account, such as wind loads, insolation, etc. Fire safety requirements are also taken into account. However, the above-mentioned documents do not take into account the factor of natural aerodynamics of space between neighboring buildings. The distance between buildings and structures is considered to be the distance between the outer walls or other structures. As a result, when designing, the distances between building objects are laid, which can not provide free movement of the wind vortex, which leads to a disturbance of the natural air flow. In this thesis, a model of aerodynamics between two high-rise buildings is considered. This mathematical model allows you to accurately calculate the optimal distance between the two buildings, which will take into account the climatic features and will preserve the natural purge.

In many technical flows of practical interest, like flow divisions, with the sudden expansion of geometry or with subsequent re-joining, are a common occurrence. The existence of a flow separation and recirculation area has a significant effect on the performance of heat transfer devices, for example, cooling equipment in electrical engineering, cooling channels of turbine blades, combustion chambers and many other heat exchanger surfaces that appear in the equipment.

Many papers are devoted to the motion of a fluid with separation and reconnection of flows without taking into account the buoyancy forces. The importance of this process is indicative of the number of papers where special attention was paid to building equipment [1-3] and developing experimental and theoretical methods for detailed study of flows with separation regions [4-7]. An extensive survey of isothermal flows in fluid flows is given in papers [10-12]. Heat transfer in the flows has been investigated by many authors, like Aung [11, 12], Aung et al. [13], Aung and Worku [14], Sparrow et al. [15, 16] and Sparrow and Chuck [17]. However, published paperson this topic do not take into account the strength of buoyancy force on the flow stream or the characteristics of heat transfer. These effects become significant in the laminar flow regime, where the velocity is relatively low, and when the temperature difference is relatively high. Ngo and Byon [18] studied the location effect of the heater and the size of the heater in a two-dimensional square cavity using the finite element method. Oztop and Abu-Nada [19] numerically investigated natural convection in rectangular shells, partially heated from the side wall by the finite volume method.

In this paper considered the influence of buoyancy forces on the flow and heat transfer characteristics in individual flows. Numerical solutions for a laminar mixed convective airflow (Pr=0.7) in a vertical two-dimensional channel with a backward-facing step to maintain the buoyancy effect are shown in Figure 1. Numerical results of interest, such as velocity and temperature distributions, re-binding lengths and friction coefficients are presented for the purpose of illustrating the effect of buoyancy forces on these parameters [20].

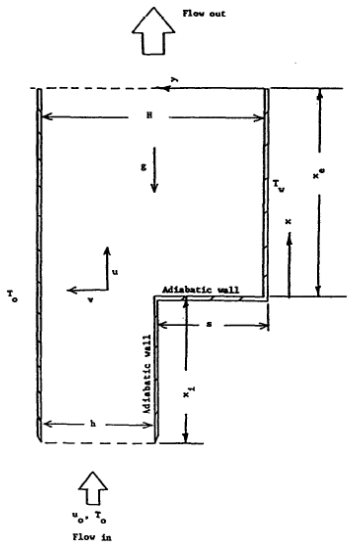

Figure 1 - Schematic representation of the backward-facing step flows.

2. Mathematical formulation of the problem

Consider a two-dimensional laminar convective flow in a vertical channel with a sudden expansion behind the inverse step of height s, as shown in Fig. 1. The straight wall of the channel is maintained at a uniform temperature equal to the temperature of the inlet air T_0. The stepped wall below the stage is heated to a uniform temperature, which can be adjusted to any desired value T_w. The upper part of the stepped wall and the reverse side is installed as an adiabatic surface. The inlet length of the channel x_i and the outlet lower length x_e of the channel are appropriate dimensions. These lengths are assumed to be infinite, but the simulation domain is limited by the length $L_e = x_e + x_i$. The smaller section of the

channel before the projection has a height, and the large section below the stage has a height $H = h + s$. Air flows up the channel with mean velocity u_0 and uniform temperature T_0. The gravitational force g in this problem is considered to act vertically downwards.

To describe this physical problem, was used assumption about constant properties, and was used the Boussinesq approximation. This system of equations in an immense form can be written in the form:

1) $$\frac{\partial U}{\partial X} + \frac{\partial U}{\partial Y} = 0 \tag{1}$$

2) $$\frac{\partial U}{\partial t} + U\frac{\partial U}{\partial X} + V\frac{\partial U}{\partial Y} = -\frac{\partial P}{\partial X} + \frac{1}{\mathrm{Re}}\left(\frac{\partial^2 U}{\partial X^2} + \frac{\partial^2 U}{\partial Y^2}\right) + \frac{Gr}{\mathrm{Re}^2}\theta \tag{2}$$

3) $$\frac{\partial V}{\partial t} + U\frac{\partial V}{\partial X} + V\frac{\partial V}{\partial Y} = -\frac{\partial P}{\partial Y} + \frac{1}{\mathrm{Re}}\left(\frac{\partial^2 V}{\partial X^2} + \frac{\partial^2 V}{\partial Y^2}\right) \tag{3}$$

4) $$\frac{\partial \theta}{\partial t} + U\frac{\partial \theta}{\partial X} + V\frac{\partial \theta}{\partial Y} = \frac{1}{\mathrm{Pr}\,\mathrm{Re}}\left(\frac{\partial^2 \theta}{\partial X^2} + \frac{\partial^2 \theta}{\partial Y^2}\right) \tag{4}$$

The dimensionless parameters in the equations given above are defined by the formula: $U = u/u_0$, $V = \upsilon/u_0$, $X = x/s$, $Y = y/s$, $\theta = (T - T_0)/(T_w - T_0)$, $P = p/\rho_0 u_0^2$, $\mathrm{Pr} = \nu/\alpha$, $\mathrm{Re} = u_0 s/\nu$, $Gr = g\beta(T_w - T_0)s^3/\nu^2$, where α – the temperature diffusion, ν – the kinematic viscosity, and β – the thermal expansion coefficient are estimated at the film temperature $T_f = (T_0 + T_w)/2$.

Boundary conditions:

(a) Inlet conditions: At the point $X = -X_i$ and $1 \le Y \le H/s$: $U = u_i/u_0$, $V = 0$, $\theta = 0$.

where u_i is the local distribution of velocities at the inlet, which is assumed to have a parabolic profile and u_i/u_0 an average inlet velocity, that is, given by formula $u_i/u_0 = 6\left[-y^2 + (H+s)y - Hs\right]/(H-s)^2$

(b) Outlet conditions: At the point $X = X_e$ and $0 \le Y \le H/s$: $\partial U/\partial X = 0$, $\partial^2\theta/\partial X^2 = 0$, $\partial V/\partial X = 0$.

(c) on the top wall:At the point $Y = H/s$ and $-X_i \le X \le X_e$: $U = 0$, $V = 0$, $\theta = 0$.

(d) on the wall of the upper stage: At the point $Y = 1$ and $-X_i \le X < 0$: $U = 0$, $V = 0$, $\partial\theta/\partial Y = 0$.

(e) on the wall of the lower stage: At point $X = 0$ and $0 \le Y \le 1$: $U = 0$, $V = 0$, $\partial\theta/\partial X = 0$.

(f) on the wall below the stage: At the point $Y = 0$ and $0 \le X \le X_e$: $U = 0$, $V = 0$, $\theta = 1$.

The last term on the right-hand side of equation (2) is the contribution of the buoyancy force. The length of the downstream flow from the simulation area was chosen to be 70 steps (X_e=70). The upper length of the design area was chosen to be 5 steps (i.e. X_i=5), and the velocity profile at the input area was set as parabolic profile, like $u_i/u_0 = 6\left[-y^2 + (H+s)y - Hs\right]/(H-s)^2$, and temperature was chosen as uniform T_0.

3. The numerical algorithm

For a numerical solution of this system of equations, the projection method is used [21-24]. The equations are approximated by the finite volume method [21-23]. At the first stage it is assumed that the transfer of momentum is carried out only through convection and diffusion, and an intermediate velocity

field is calculated by the fourth-order Runge-Kutta method [21-23]. At the second stage, according to the found intermediate velocity field, there is a pressure field. The Poisson equation for the pressure field is solved by the Jacobi method. At the third stage it is assumed that the transfer is carried out only due to the pressure gradient. At the fourth stage, the equations for the temperature are calculated by the fourth-order Runge-Kutta method.

$$I. \quad \int_{\Omega} \frac{\vec{u}^* - \vec{u}^n}{\Delta t} d\Omega = -\oint_{\partial\Omega} (\vec{u}^n \vec{u}^* - \frac{1}{\mathrm{Re}} \nabla \vec{u}^*) n_i d\Gamma - \int_{\Omega} \frac{Gr}{\mathrm{Re}^2} \theta d\Omega,$$

$$II. \quad \oint_{\partial\Omega} (\nabla p) d\Gamma = \int_{\Omega} \frac{\nabla \vec{u}^*}{\Delta t} d\Omega,$$

$$III. \quad \frac{\vec{u}^{n+1} - \vec{u}^*}{\Delta t} = -\nabla p,$$

$$IV. \quad \int_{\Omega} \frac{\theta^* - \theta^n}{\Delta t} d\Omega = -\oint_{\partial\Omega} (\vec{u}^n \theta^* - \frac{1}{\mathrm{Re}\,\mathrm{Pr}} \nabla \theta^*) n_i d\Gamma,$$

4. Parallelization algorithm

For numerical simulation was constructed a computational meshby using the PointWise software. The problem was launched on the ITFS-MKM software using a high-performance computing. This numerical algorithm is completely parallelized using various geometric domain decompositions (1D, 2D and 3D). Geometric partitioning of the computational grid is chosen as the main approach of parallelization. In this case, there are three different ways of exchanging the values of the grid function on the computational nodes of a one-dimensional, two-dimensional, and three-dimensional mesh. After the domain decomposition stage, when parallel algorithms are built on separate blocks, a transition is made to the relationships between the blocks, the simulations on which will be executed in parallel on each processor. For this purpose, a numerical solution of the equation system was used for an explicit scheme, since this scheme is very efficiently parallelized. In order to use the domain decomposition method as a parallelization method, this algorithm uses the boundary nodes of each subdomain in which it is necessary to know the value of the grid function that borders on the neighboring elements of the processor. To achieve this goal, at each compute node, ghost points store values from neighboring computational nodes, and organize the transfer of these boundary values necessary to ensure homogeneity of calculations for explicit formulas.

Data transmission is performed using the procedures of the MPI library [25]. By doing preliminary theoretical analysis of the effectiveness of various domain decomposition methods of the computational domain for this problem, which will estimate the time of the parallel program as the time T_{calc} of the sequential program divided by the number of processors plus the transmission time $T_p = T_{calc} / p + T_{com}$. While transmissions for various domain decomposition methods can be approximately expressed through capacity:

$$\begin{aligned} T_{com}^{1D} &= t_{send} 2N^2 x2 \\ T_{com}^{2D} &= t_{send} 2N^2 x4 p^{1/2} \\ T_{com}^{3D} &= t_{send} 2N^2 x6 p^{2/3} \end{aligned} \tag{5}$$

where N^3 – the number of nodes in the computational mesh, p - the number of processors (cores), t_{send} – the time of sending one element (number).

It should be noted that for different decomposition methods, the data transmission cost can be represented as $T_{com}^{1D} = t_{send} 2N^2 xk(p)$ in accordance with the formula (5), where $k(p)$ is the proportionality coefficient, which depends on the domain decomposition method and the number of processing elements used.

At the first stage, one common program was used, the size of the array from start to run did not change, and each element of the processor was numbered by an array of elements, starting from zero. For the test simulation is used well known problem – 3D cavity flow. Despite the fact that according to the theoretical analysis of 3D decomposition is the best option for parallelization (Figure 3), computational experiments showed that the best results were achieved using 2D decomposition, when the number of processes varies from 25 to 144 (Figure 3).

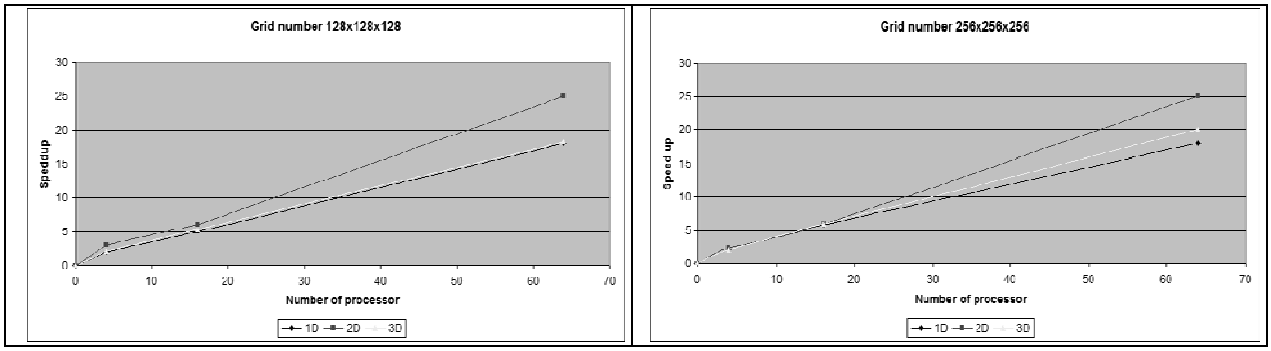

Figure 2 - Speed-up for various domain decomposition methods of the computational domain

Based on the preliminary theoretical analysis of the graphs, the following character can be noted. The simulation time without the interprocessor communications cost with different domain decomposition methods should be approximately the same for the same number of processors and be reduced by T_{calc} / p . In fact, the calculated data show that when using 2D decomposition on different computational grids, the minimal cost for simulation and the cost graphs are much higher, depending on the simulation time, on several processors taken T_{calc} / p .

To explain these results, it is necessary to pay attention to the assumptions made in the preliminary theoretical analysis of efficiency for this task. First, it was assumed that regardless of the distribution of data per processor element, the same amount of computational load was done, which should lead to the same time expenditure. Secondly, it was assumed that the time spent on interprocessorsending's of any degree of the same amount of data is not dependent on their memory choices. In order to understand what is really happening, the following sets of computational simulations test were carried out. For evaluation, the sequence of the first approach was considered when the program is run in a single-processor version, and thus simulates various geometric domain decomposition methods of data for the same amount of computation performed by each processor.

5. Numerical results for test problem

Geometric parameters are indicated in Figure 1: channel length L=75, channel height H=2, step height S=1. Numerical results were obtained for the dimensionless numbers Re=50, Pr=0.7 and Gr=19.1 [20].

Figure 3 shows the comparison of the longitudinal velocity profile with the numerical data of Lin et al. [20] at the point $x/x_f = 0.5$, where $x_f = 2.91$. Figure 4 shows the comparison of temperature profiles with the numerical data of Lin et al. [20] at the point $x/x_f = 0.5$, where $x_f = 2.91$. It can be seen from the figures that the mathematical model and the numerical algorithm which is used in this paper is coincided with the numerical results obtained by Lin et al. [20]. Figure 5 shows the streamlines and the horizontal velocity contour for dimensionless numbers Re=50, Pr=0.7 and Gr=19.1.

Figure 6 shows the temperature profile for dimensionless numbers Re=50, Pr=0.7 and Gr=19.1. For a better understanding of this process from figures 6-8 can be seen the development of the backward-facing step flow with vertical buoyancy force: the initiation and process of the development of the region of flows reconnection with taking into account the buoyancy forces.

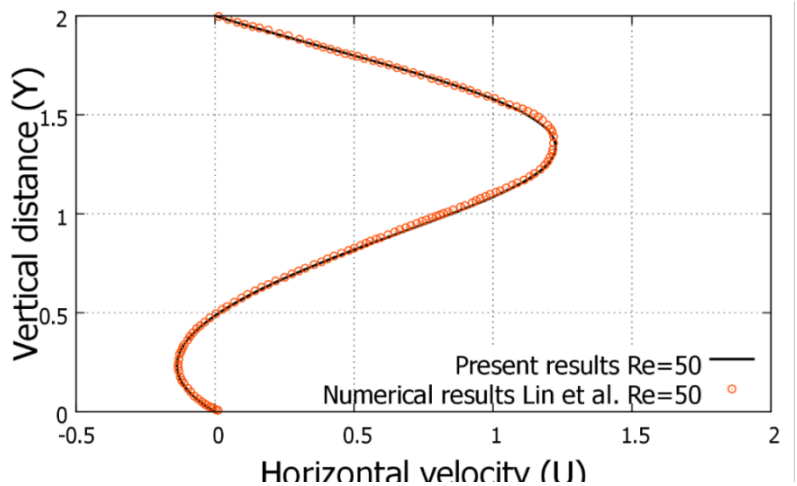

Figure 3 - Velocity profile with vertical buoyancy forces for dimensionless number Re=50, $\Delta T = 1°C$, $x/x_f = 0.5$, where $x_f = 2.91$.

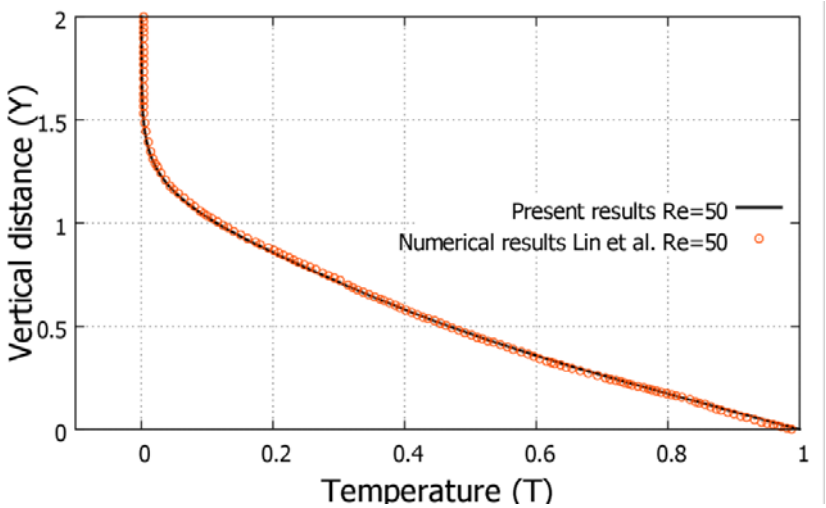

Figure 4 - Temperature profile with vertical buoyancy forces for dimensionless number Re=50, $\Delta T = 1°C$, $x/x_f = 0.5$, where $x_f = 2.91$.

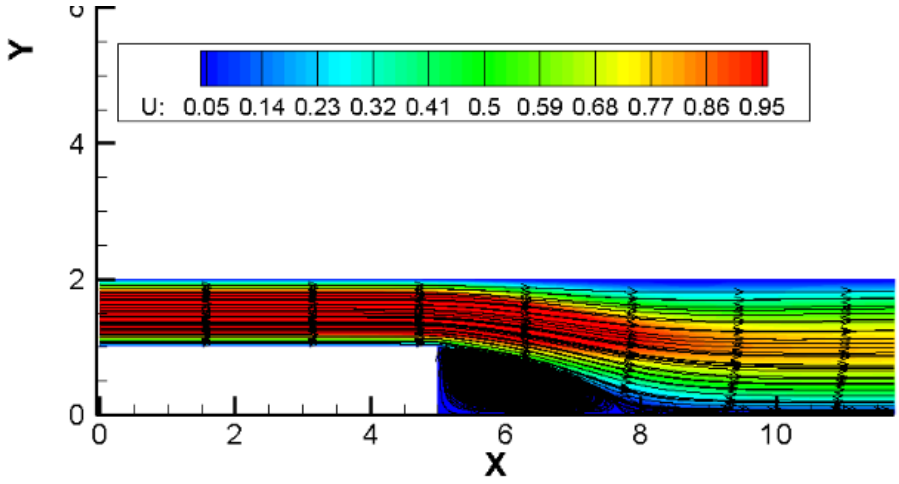

Figure 5 - The contour of the horizontal velocity component with streamlines for dimensionless numbers Re=50, Pr=0.7 and Gr=19.1.

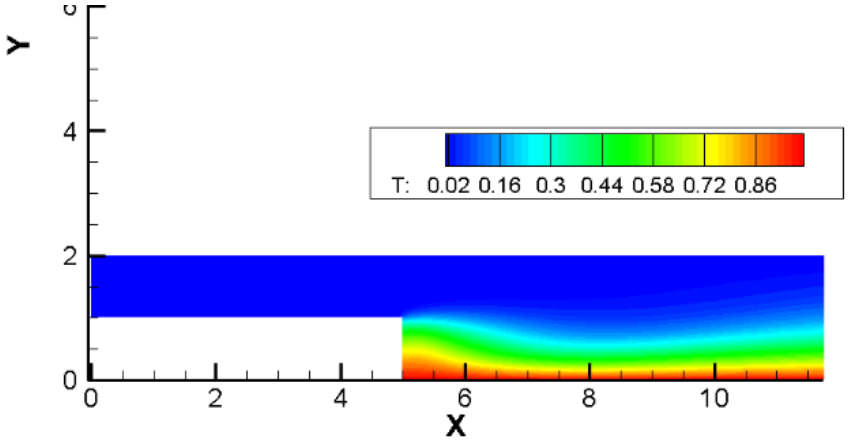

Figure 6 - Temperature contour for dimensionless numbers Re=50, Pr=0.7 and Gr=19.1

6. Numerical results for real problem

For the real problem considered a man-made obstacle 9 floors (27 m) and 5 floors (15 m) buildings. The wind flow is conventionally moving from the high building side to the low one. The following models consider the calm, according to the Beaufort wind speed scale. The speed of wind is in the range from 0 to 0.2 m/s. To find the optimal distance, various parameters prescribed in the above-mentioned standards were used.

According to the fire protection requirements specified in Building norms and regulations of the Republic of Kazakhstan 3.01-01-2002, 2.12 *, the minimum distance between houses with a height of 4 floors or more must be at least 20 meters. However, having constructed this model, a result was obtained, showing that at such a distance between the buildings, there was no wind, therefore, air circulation does not occur in this interval.

After that, the IBC (International Building Code) standard used in the USA was considered, where the distance between two buildings is calculated according to the following formula: $\delta_{MT} = \sqrt{(\delta_{M1})^2 + (\delta_{M2})^2}$, where δ_{MT} - required distance, δ_{M1}, δ_{M2} - height of the first and second buildings, respectively.

For the calculations, the area was divided into the 14 design subareas of different sizes. Each subregion is a grid block, which contains a part of a curvilinear, uneven, unstructured grid. When creating a grid, the number of points is chosen in such a way that no oscillations occur in the solution of the problem and the results are correct for large values of the Reynolds number. Thus, the constructed grid contains more than 100 000 control volumes.

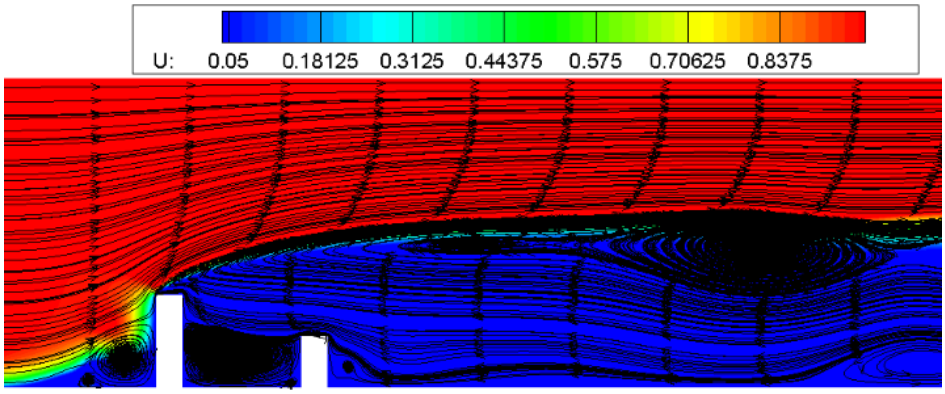

Figure 7 - Horizontal velocity-component and streamlines with buoyancy force for Pr=0.7 and $\Delta T = 1°C$

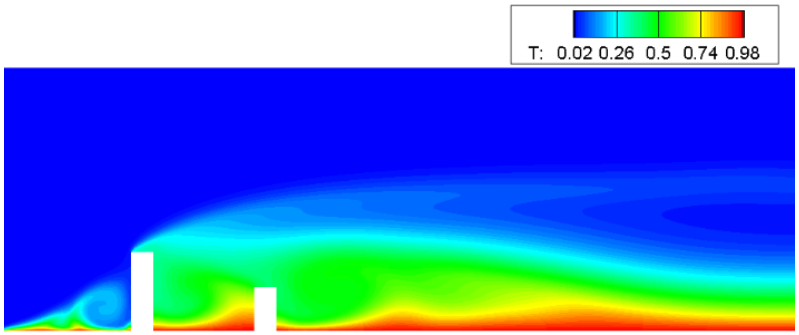

Figure 8 - Temperature component with buoyancy force for Pr=0.7 and $\Delta T = 1°C$

In the interval between the buildings and near the streamlined surfaces of buildings, the grid is thickened, i.e. the sizes of control volumes decrease. This allows for more accurate simulations. As the grid is removed from the vortex zone and the dimensions of the control volumes increase the flow around. Therefore, in areas that are not of great interest in solving a given problem, net catch is smaller. And in the most important zones for the model, the number of nodes is greater, which allows obtaining more accurate results.

In figure 7 shows horizontal velocity-component and streamlines with buoyancy force for Pr=0.7 and $\Delta T = 1°C$. In figure 8 can be seen temperature component with buoyancy force for Pr=0.7 and $\Delta T = 1°C$. The distance obtained for existing buildings was 31 m and satisfied all the standards specified in the republican standards. This model also showed that a vortex does not occur at a given distance. In the following case, the length of extensions to the buildings (balconies, porches, etc.) was added to the previous value and an approximate distance of 35 m was obtained. This model showed that a vortex in the gap occurs and therefore the natural purging between buildings is not broken.

7. Conclusion

Numerical studies of the laminar flow were carried out by the zone of joining the flows behind the backward-facing step with taking into account the buoyancy forces. This gave a deeper insight into the internal flow behind the backward-facing step and the processes of flows reconnection under the influence of temperature effects, which in turn gave an idea of the further appearance of secondary zones. The distance from the ledge to the canal boundary is 4 times the channel height, for a more detailed study of the backward-facing step flows withtaking into account the buoyancy forces [20]. The numerical data of the velocity distribution showed the formation of a primary reattachment zone of backward-facing step flows. To numerically solve the Navier-Stokes equations system, the projection methodwas used. From numerical results can be seen that the realized numerical method gives a small error in comparison with the numerical results of other authors [20] for the dimensionless numbers Re=50, Pr=0.7 and Gr=19.1.

After testing the numerical algorithm with the buoyancy forces, for the real problem considered a man-made obstacle with 9 floors (27 m) and 5 floors (15 m). In this problem, the wind speed was regarded as calm, according to the Beaufort wind speed scale (from 0 to 0.2 m/s). According to the data obtained as a result of the numerical simulation taking into account the buoyancy forces, it can be said that the current standards and rules for construction do not guarantee the required aerodynamics of the terrain.

Also in this paper is used a parallel algorithmto obtain fast numerical results. This parallel algorithm is based on one-dimensional, two-dimensional and three-dimensional domain decomposition method. The numerical results from the 3D cavity flow test problem, which used 1D, 2D and 3D domain decomposition method showed that 3D domain decomposition is not time-consuming compared to 2D domain decomposition, for the number of processors that does not exceed 250, and 3D domain decomposition has more time-consuming software implementation and the use of 2D domain decomposition is sufficient for the scope of the problem. That's why for backward-facing step flow with vertical buoyancy force is used 2D domain decomposition. It should also be noted that setting the boundary conditions is an important process. In the future, this mathematical model and a parallel numerical algorithm can be applied to various complex flows taking into account the buoyancy forces.

REFERENCES

[1] Abbott D.E., Kline S.J. (**1962**) Experimental investigations of subsonic turbulent flow over single and double backward-facing steps,J. Basic Engng. 84:317.

[2] SebanrA. (**1964**) Heat transfer to the turbulent separated flows of air downstream of a step in the surface of a plate,J. Heat Transfer.86:259.

[3] Goldsteinr J., Eriksenv L., Olsonr M., Eckerte R.G. (**1970**) Laminar separation, reattachment and transition of flow over a downstream-facing step,J.Basic Engng. 92:732.

[4] Durst F., Whitelawj H. (**1971**) Aerodynamic properties of separated gas flows: existing measurements techniques and new optical geometry for the laser-Doppler anemometer,Prog. Heat Mass Transfer.4:311.

[5] Gosmana D., Punw M. (**1974**) Lecture notes for course entitled: 'Calculation of recirculating flow, Heat Transfer Rep. 74:2.

[6] Kumara, Yajnikk S. (**1980**) Internal separated flows at large Reynolds number, J. Fluid Mech. 97:27.

[7] Chiang T.P., Tony W.H., Sheu, Fang C.C. (**1999**) Numerical investigation of vortical evolution in backward-facing step expansion flow, Appl. Math. 23:915-932.

[8]. Armaly B. F. and Durst F.(**1980**) Reattachment length and recirculation regions downstream of two dimensional single backward facing step. In Momentum and Hear Transfer Process in Recirculating Flows, ASME HTDVol. 13, pp. l-7. ASME, New York.

[9]. Eaton J. K. and Johnson J. P., (**1981**) A review of research on subsonic turbulent flow reattachment, AIAA J. 19:1093-1100.

[10]. Simpson R. L.(**1981**) A review of some phenomena in turbulent flow separation, J. Fluid Engng 103:528-530.

[11]. Aung W. (**1983**) An experimental study of laminar heat transfer downstream of backsteps, J. Heat Transfer 105:823-829.

[12]. Aung W., (**1983**) Separated forced convection, Proc. ASMEIJSME Thermal Enana Joint Con/.. 2: 499-515. ASME. New York.

[13]. Aung W., Baron A. and Tsou F. K., (**1985**) Wall independency and effect of initial shear-layer thickness in separated flow and heat transfer, Int. J. Hear Mass Transfer, 28:1757-1771.

[14]. Aung W. and Worku G., (**1986**) Theory of fully developed. combined convection including flow reversal, J. Hear Transfer, 108:485-488.

[15]. Sparrow E. M., Chrysler G. M. and Azevedo L. F.(**1984**) Observed flow reversals and measured-predicted Nusselt numbers for natural convection in a one-sided heated vertical channel, J. Heat Transfer, 106:325-332.

[16]. Sparrow E. M., Kang S. S. and Chuck W .(**1987**) Relation between the points of flow reattachment and maximum heat transfer for regions of flow separation. Int. J. Heat Mass Transfer, 30:1237-1246.

[17]. Sparrow E. M. and Chuck W., (**1987**) PC solutions for heat transfer and fluid flow downstream of an abrupt, asymmetric enlargement in a channel, Numer. Heat Transfer, 12:1940.

[18]. Ngo I., Byon C., (**2015**) Effects of heater location and heater size on the natural convection heat transfer in a square cavity using finite element method, J. Mech. Sci. Technol. 29 (7):2995.

[19]. Oztop H. F., Abu-Nada E. (**2008**) Numerical study of natural convection in partially heated rectangular enclosures filled with nanofluids, Int. J. Heat. Fluid Fl., 29(5):1326 - 1336.

[20]. Lin J.T., Armaly B.F., Chen T.S. (**1990**) Mixed convection in buoyancy-assisting, vertical backward-facing step flows, International Journal of Heat and Mass Transfer. 33(10): 2121-2132.

[21]. Issakhov A., (**2015**) Mathematical modeling of the discharged heat water effect on the aquatic environment from thermal power plant // International Journal of Nonlinear Science and Numerical Simulation, 16(5):229–238, doi:10.1515/ijnsns-2015-0047.

[22]. Issakhov A., (**2016**) Mathematical modeling of the discharged heat water effect on the aquatic environment from thermal power plant under various operational capacities // Applied Mathematical Modelling, 40(2):1082–1096 http://dx.doi.org/10.1016/j.apm.2015.06.024.

[23]. Issakhov A. (**2017**) Numerical Study of the Discharged Heat Water Effect on the Aquatic Environment from Thermal Power Plant by using Two Water Discharged Pipes. International Journal of Nonlinear Sciences and Numerical Simulation, 18(6):469–483.

[24]. Chorin A.J. (**1968**) Numerical solution of the Navier-Stokes equations, Math. Comp.22: 745-762.

[25]. Karniadakis G. E., Kirby II R. M. (**2000**) Parallel Scientific Computing in C++ and MPI: A Seamless Approach to Parallel Algorithms and their Implementation. CambridgeUniversityPress, p. 630.

А. Исахов, А. Абылкасымова, М. Сакыпбекова

Казахский национальный университет им. аль-Фараби, Алматы, Казахстан

ПРИМЕНЕНИЕ ТЕХНОЛОГИЙ ПАРАЛЛЕЛЬНЫХ ВЫЧИСЛЕНИЙ ДЛЯ МОДЕЛИРОВАНИЯ ВЕТРОВОГО ПОТОКА ВОКРУГ АРХИТЕКТУРНЫХ ПРЕПЯТСТВИЙ С ВЕРТИКАЛЬНЫМИ СИЛАМИ ПЛАВУЧЕСТИ

Аннотация. Принимая во внимание высокие темпы строительства в современных крупных городах, очень важно сохранить естественную аэродинамику между зданиями. Необходимо исследовать аэродина-

мику между архитектурными сооружениями, сделав предварительное прогнозное исследование перед началом строительства. Наиболее оптимальным способом оценки является построение математической модели воздушного потока. В настоящей работе представлены численные решения ветрового потока вокруг архитектурных препятствий с вертикальными силами плавучести. Для описания этого процесса используется несжимаемое уравнение Навье-Стокса. Эта система аппроксимируется методом контрольного объема и решается численно методом расщепление по физическим параметрам. Уравнение Пуассона, удовлетворяющее уравнению дискретной непрерывности, решаемому итерационным методом Якоби на каждом временном шаге. Для проверки правильности математической модели и численного алгоритма решена тестовая проблема. Численные решения обратного потока с вертикальными силами плавучести, которые сравнивались с численными результатами других авторов. Этот численный алгоритм полностью распараллеливается с использованием различных методов геометрических декомпозиций (1D, 2D и 3D). В работе проделан предварительный теоретический анализ различных методов декомпозиции вычислительной области и реальных вычислительных экспериментов для этой задачи, и был определен наилучший метод разложения доменов. В будущем для различных сложных потоков с вертикальными силами плавучести может быть применена проверенная математическая модель и параллельный численный алгоритм с наилучшим методом декомпозиции доменов.

Ключевые слова: метод декомпозиции доменов, обтекание архитектурных препятствий, обратный поток, метод проецирования, вертикальные силы плавучести, смешанная конвекция.

А. Исахов, А. Абылкасымова, М. Сакыпбекова

әл-Фараби атындағы Қазақ Ұлттық университеті, Алматы, Қазақстан

ПАРАЛЛЕЛЬДІ ЕСЕПТЕУ ТЕХНИКАСЫНЫҢ СӘУЛЕЛЕНУ КЕДЕРГІЛЕРІНІҢ АЙНАЛАСЫНДА ЖЕЛДІҢ АҒЫНЫН ҮЛГІЛЕУ ҮШІН ҚОЛДАНУ

Аннотация. Қазіргі заманғы ірі қалаларда құрылыстың жоғары қарқынын ескере отырып, ғимараттар арасындағы табиғи аэродинамиканы сақтау өте маңызды. Архитектуралық құрылыс арасындағы аэродинамиканысын зерттеу қажет, құрылысты бастамас бұрын алдын-ала болжамды зерттеуді жасау керек.Бағалаудың оңтайлы әдісі ауа ағынының математикалық моделін құру болып табылады. Бұл мақалада тік қозғалыс күштерімен архитектуралық кедергілер айналасында желдің ағынының сандық шешімдері көрсетілген. Бұл процесті сипаттау үшін сығылмайтын Навье-Стокс теңдеуі қолданылады. Бұл жүйе ақырлы көлем әдісімен жуықталып, физикалық параметрлер бөліну әдісімен сандық түрде шешілді. Дискретті үзіліссіз теңдеуін қанағаттандыратын Пуассон теңдеуі әр кезеңде Якоби итеративті әдісімен шешіледі. Тексеру үшін математикалық модельдің дұрыстығын және сандық алгоритмді сынау мәселесі шешіледі. Басқа авторлардың сандық нәтижелерімен салыстырылған тік күшінің күштерімен артқа бағытталған қадамдық ағынның сандық шешімдері қарастылды. Бұл сандық алгоритм әртүрлі геометриялық доменді декомпозиция (1D, 2D және 3D) арқылы толығымен параллельленеді. Сандық доменнің әртүрлі декомпозиция әдістерінің алдын-ала теориялық анализі жәнеосы мәселе бойынша нақты есептеу эксперименттер жасалды және ең тиімді домен декомпозиция әдісі анықталды. Келешекте тік қаттылық күштерімен әртүрлі күрделі ағындар үшін дәлелденген математикалық модель және үздік домен декомпозиция әдісімен параллельді сандық алгоритм қолданылуы мүмкін.

Түйін сөздер: домендідекомпозиция әдісі, архитектуралық кедергілердің ағымы, артқа қарай жүретін қадамдық ағын, проекциялау әдісі, тік күші күші, аралас конвекция.

N E W S
OF THE NATIONAL ACADEMY OF SCIENCES OF THE REPUBLIC OF KAZAKHSTAN
PHYSICO-MATHEMATICAL SERIES
ISSN 1991-346X
Volume 4, Number 320 (2018), 58 – 65

UDC 539.2

K. Askaruly[1] , N.K. Manabayev[2]

The Kazakh National Research Technical University after K.I.Satpaev, Almaty, Kazakhstan
E-mail: k.askaruly@gmail.com infopresskz@gmail.com

TECHNOLOGICAL PROCESSES FOR THE PRODUCTION OF NWS FROM GALLIUM NITRIDE (GaN) BY CVD METHOD

Abstract. Gallium nitride (GaN) is a III-V semiconductor with a direct zone gap of ~3,4 eV. GaN has important potentials in white light-emitting diodes, blue lasers and field-effect transistors due to its superthermal stability and excellent optical properties, playing major roles in future lighting, in order to reduce the cost of energy and sensors to withstand radiation. The article provides an overview of the authors' research on GaN obtained by the CVD method, which is a much more promising material than other traditional materials. The physical properties are compared to improve the material parameters, the methods of obtaining and the results of the research work of different authors for the creation of light diodes, transistors, microwave electronics.

Keywords: GaN, Gallium Nitride, CVD method, semiconductors, review.

Today, compounds of metals with nitrogen, the so-called nitrides, are of particular interest, among which many have high refractoriness, dielectric and semiconducting properties, the ability to transfer to superconductors at relatively high temperatures, and high chemical stability in various corrosive media. Many of the nitrides have already been successfully used in electronics, nuclear industry, semiconductor and dielectric technology, in space technology, modern machine building, metallurgy, electrical engineering and other industries [1-3]. And it is also possible to use nanocarriers to solve such problems as cancer diseases and one of the directions - creation of antitumor drugs - obtaining structures based on boron nitride [4], which has chemical inertness and high resistance to oxidation. Nanoparticles of hexagonal boron nitride 100-150 nm in size with a smooth and developed surface can be obtained by chemical vapor deposition [5].

Due to their unique properties, the nitrides of metals of the third group (III-N) are very promising for the creation of various semiconductor devices. And one of the elements of the III-group is - gallium nitride (GaN). GaN has long been interested in researchers and developers of semiconductor devices. The heterostructure of GaN and its solid solutions possess physical properties that provide electronic devices based on them, optical, power and frequency characteristics that allow them to be used in various fields of semiconductor electronics.

The main advantage of gallium nitride [6-11] over other common electronics materials is a wide forbidden band of 3,5 eV (1.1 eV for silicon). This means that GaN-transistors operate at higher temperatures and are less sensitive to ionizing radiation (which in the literal sense of the word is vital for space and special electronics). In theory, the operating temperature of GaN devices reaches 500 ° C, in practice it is still equal to 150-200 ° C. The maximum electric field strength for GaN is $3,3 \times 10^6$ V/cm - this is 11 times greater than that of silicon. And due to the high density of charge carriers GaN-transistors withstand much higher currents. Table 1 shows the comparison of gallium nitride with other semiconductors.

Table 1 - Comparison of the properties of semiconductor materials. The numbers in the table are approximate

Material	Bandgap, Eg (eV at)	Electron Mobility (cm^2/Vs)	Hole Mobility (cm^2/Vs)	Critical Field *Ec* (V/cm)	Thermal Conductivity бТ (W/m*K)	Coefficient of Thermal Expansion (ppm/K)
GaN	***3,4 300 K***	***100***	***30***	***3 × 10^6***	***100***	***5,4-7,2***
Si	1,12 *300 K*	1350	480	2,5 × 10^5	130	2,6
AlN	6.2 *300 K*	-	-	-	-	-
InN	1,89 *300 K*	-	-	-	-	-
3C-SiC	2,4 *300 K*	1000	40	2 × 10^6	700	2,77
6H-SiC	2,86	400	75	24× 10^5	700	5,12
4H-SiC	3,25	700	-	318× 10^4	700	5,12
InSb	0,17	77000	580	1× 10^3	18	5,37
InAs	0,354	44000	500	4× 10^4	27	4,52
GaSb	0,726	3000	1000	5× 10^4	32	7,5
InP	1,344	5400	200	5× 10^5	68	4,6
GaAs	1,424	5800	400	4× 10^5	55	5,73
Ge	0,611	3900	1900	1× 10^5	58	5,9
GaP	2,26	250	150	1× 10^6	110	4,65
C (diamond)	5,5	2200	1800	6× 10^6	1300	0,8

PERIODIC TABLE

IA	IIA	IIIA	IVA	VA	VIA	VIIA	VIII			IB	IIB	IIIB	IV	VA	VIB	VIIB	O
1 H 1.008																	2 He 4.003
3 Li 6.941	4 Be 9.012											5 B 10.81	6 C 12.01	7 N 14.01	8 O 16.00	9 F 19.00	10 Ne 20.179
11 Na 22.990	12 Mg 24.305											13 Al 26.98	14 Si 28.09	15 P 30.97	16 S 32.07	17 Cl 35.45	18 Ar 39.948
19 K 39.098	20 Ca 40.08	21 Sc 44.956	22 Ti 47.90	23 V 50.942	24 Cr 51.996	25 Mn 54.938	26 Fe 55.847	27 Co 58.933	28 Ni 58.70	29 Cu 63.546	30 Zn 65.39	31 Ga 69.72	32 Ge 72.61	33 As 74.92	34 Se 78.96	35 Br 79.90	36 Kr 83.80
37 Rb 85.468	38 Sr 87.62	39 Y 88.906	40 Zr 91.22	41 Nb 92.906	42 Mo 95.94	43 Tc (99)	44 Ru 101.07	45 Rh 102.905	46 Pd 106.4	47 Ag 107.868	48 Cd 112.4	49 In 114.8	50 Sn 118.7	51 Sb 121.8	52 Te 127.6	53 I 126.9	54 Xe 131.30
55 Cs 132.905	56 Ba 137.33	57 La 138.9	72 Hf 178.49	73 Ta 180.948	74 W 183.85	75 Re 186.2	76 Os 190.2	77 Ir 192.22	78 Pt 195.09	79 Au 196.966	80 Hg 200.59	81 Tl 204.37	82 Pb 207.2	83 Bi 209.0	84 Po (210)	85 At (210)	86 Rn (222)
87 Fr (223)	88 Ra (226)	89 Ac 227.0															

LANTHANIDES	57 La 138.9	58 Ce 140.115	59 Pr 140.1	60 Nd 144.2	61 Pm (145)	62 Sm 150.4	63 Eu 152.0	64 Gd 157.2	65 Tb 158.9	66 Dy 162.5	67 Ho 164.9	68 Er 167.3	69 Tm 168.9	70 Yb 173.0	71 Lu 174.96
ACTINIDES	89 Ac 227.0	90 Th 232.0	91 Pa 231.0	92 U 238.0	93 Np 237.0	94 Pu (244)	95 Am (243)	96 Cm (247)	97 Bk (247)	98 Cf (251)	99 Es (252)	100 Fm (257)	101 Md (256)	102 No (259)	103 Lr (257)

Figure 1 - Periodic table, where the shaded cells indicate the elements that can be deposited using CVD

Another no less important area is the production of a nanotube of gallium nitride. Thanks to the tubular structure, the material must be significantly more sensitive to environmental influences than the already known nanowires, which opens up prospects for its use in filtration, sensorics, biology, etc.

CVD processes occur at much higher temperatures than PVD processes, typically 300 to 900 ° C. This heat is supplied from an oven, radio frequency coil or laser, but it always heats the substrate. Substrates that do not tolerate this temperature should have thin films deposited as a result of the physical form of vapor deposition.

The advantage of substrate temperature in some CVD processes is that they have less waste deposition, especially in cold wall reactors, since only heated surfaces are coated. When using a laser heating system, the process of chemical vapor deposition becomes selective with respect to the laser path; this is a clear advantage over the physical methods of vapor deposition, such as spraying.

In the paper [13] synthesized nanowires and GaN nanotubes by direct reaction of metallic gallium vapor (Ga, 99.99%) with flowing NH_3 in an electric furnace. At different NH_3 flow rates between 50 and 200 centimeters, large-scale nanowires and GaN tubes were formed at a growth temperature of 900 ° C on a Si (111) substrate. GaN grown on a Si (111) substrate at 900 ° C and at a NH_3 flow rate of 50 cccm, the preferred orientation is growth in the (002) direction. When the flow rate of NH_3 increases to 100 centimeters, the products have a much wider diameter, but, the length is shorter. If continue increasing the NH_3 flow to 200 centimeters, available get nanotubes and nanolayers. Hence, the faster the NH_3 flow rate, the greater the GaN surface tension.

The GaN [14] layers were deposited on the CVD-grown h-BN layers using an organometallic CVD. Trimethylgallium and NH_3 were used as precursors, and the V / III ratio was maintained at 2000-4000 during growth. Before the growth of the GaN layer, the substrate was heated to 1100 ° C for 3-20 min only with H_2 gas. The temperature was then lowered to 540-600 ° C for the growth of the GaN nucleation layer. After 3 min growth of the GaN nucleation layer, GaN epitaxial layers were grown at a higher temperature in the range 1000-1100 ° C. No additional intermediate layers or substrate treatments were used to grow the GaN layer on the growth of CVD h-BN.

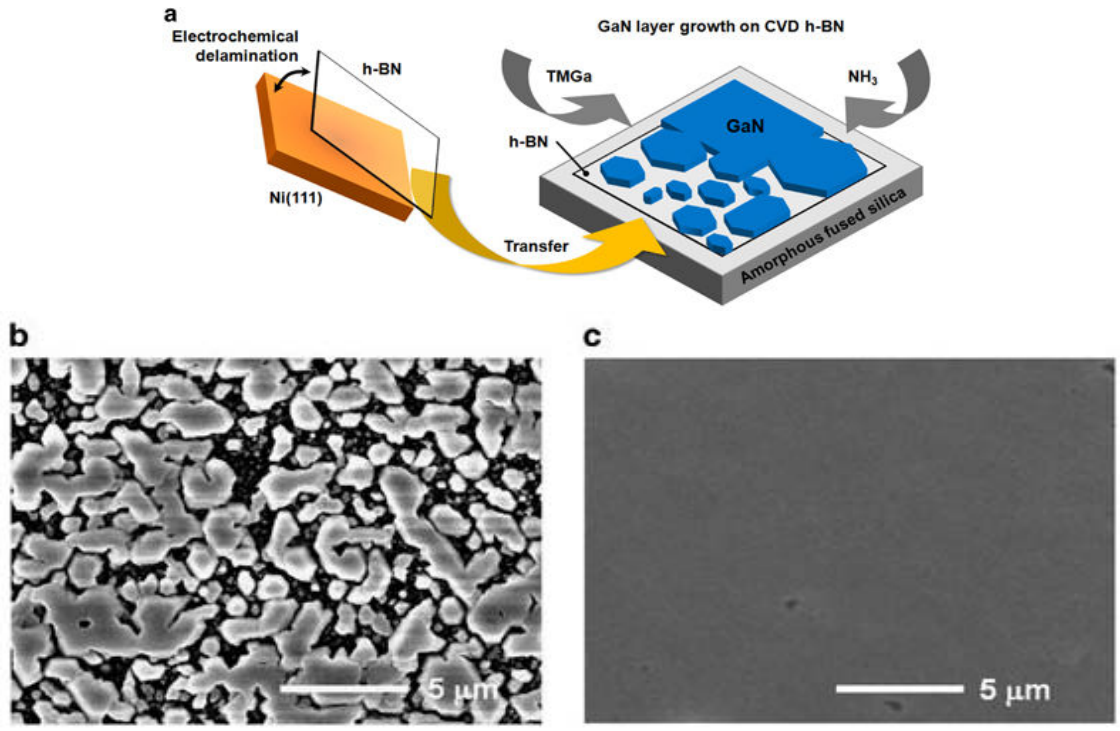

Figure 2 - Growth of GaN films on transferable chemical vapor deposition (CVD) - hexagonal boron nitride (h-BN)

(a) A schematic illustration of the transfer of h-BN grown by CVD from Ni (111) to amorphous fused quartz substrates and the growth of a gallium nitride (GaN) layer using organometallic chemical vapor deposition (MOCVD). Scanning electron microscopy of field radiation (FE-SEM) images

(b) high-density discrete GaN islands that are almost fused into GaN microstructures several microns in size and (c) fully coalesced GaN films grown on CVD-grown h-BN.

Hopefully, h-BN, grown in CVD, has already discovered many atomic rocks, which allowed to increase the high-density GaN islands, which merged to form a flat homogeneous film. In addition, almost single-crystal GaN layers were grown directly on the growth of CVD h-BN without the use of other single crystal substrates. A clear observation of the high-density GaN epitaxial growth on a large-scale scalable single-crystal CVD-grown h-BN opens the way for new applications of h-BN in the development of a number of inorganic semiconductor devices.

Gallium nitride and indium nitride nanotubes [15] were grown using a hot wall chemical vapor deposition (CVD) system. NWs GaN were synthesized by the metal-catalyzed (Ni or Fe) growth of VLS on alumina or oxidized silicon substrates. This process included a solid gallium source (either metallic Ga, or metallic Ga in combination with Ga_2O_3), heated to temperatures between 800 and 1100 ° C, in ammonia flowing at a rate of 2 centimeters to 100 centimeters. This process consistently produced nanowires with similar structural and electrical properties for similar growth parameters, having a high crystalline quality (Table 2).

Table 2 - Growth parameters for NWs GaN

Parameters	***Growth 1***	***Growth 2***
Temperature C	800	950
Ammonia Flow sccm	100	2
Substrate	Si/SiO_2	Si/SiO_2
Gallium Source	$Ga+Ga_2O_3$	$Ga+Ga_2O_3$
Pressure	1 atm	1 atm
Metal Catalyst	Ni	Fe

Both types of nanowires exhibit large carrier concentrations with decreasing mobility with increasing free carrier concentrations, which is consistent with a transport in which dispersion of impurities predominates. In the case of nanowires of gallium nitride, using the feedback between the parameters of growth and electrical characteristics, it was possible to reduce (increase) the concentration of carriers (mobility) by one order. In addition, simple theoretical estimates and annealing experiments show that nanowires of gallium nitride are highly compensated.

Epitaxial layers [16] were grown on an AIX2400G3-HT instrument of MOC-hydride epitaxy. Sources of gallium, nitrogen and dopants (trimethylgallium (TMGa), NH_3 and bis-cyclopentadienyl magnesium (Cp_2Mg), respectively) were delivered to the reactor with a hydrogen stream. 0.5 μm p-GaN epitaxial layers were grown on 2'-Al_2O_3 (1000) substrates with a pre-deposited i-GaN 2 μm buffer layer. Doping-impurity consumption was $5.4 \cdot 10^{-7}$ mol / min. The temperature and growth rate of GaN were the same for all samples. Two methods were used for post-growth thermal annealing. Some of the samples were annealed at 800-1000 ° C in an epitaxy reactor for 7 min under a nitrogen atmosphere. Other samples were annealed at 1000 ° C in an IR-heated unit with rapid thermal annealing at different times from 0.5 to 3 min. Heating to specified temperatures was 5-7 s. The annealing atmosphere was nitrogen at a pressure of 0.1 atm. The same pressure was used for all samples. A significant change in the electrophysical properties of the p-GaN: Mg samples as a result of a change in the annealing temperature. The main observation is a significant (approximately 20-fold) increase in the hole concentration in the samples annealed at 1000 ° C, compared to those that were annealed at 800 ° C, which is probably due to the higher activation of the acceptor.

In the paper [17] talks about the approach to the synthesis of straight and smooth GaN nanowires with catalyzed NiO by the CVD method. The nanorbeters were deposited on a substrate from a $LaAlO_3$ monolayer without the use of a template. Before deposition, the substrate was immersed rapidly in a solution of ethanol Ni (NO_3) 2 and then heated at 900 ° C in a long quartz tube in an Ar flow for 2 hours (h) to decompose Ni (NO_3) 2 into NiO nanoparticles. Then, the growth of the nanoparticles GaN was carried out in a long quartz tube at 920-940 ° C in a NH_3 stream for 5-20 min. The synthesized GaN nanowires had a diameter of 10-40 nm and a maximum length of about 500 μm. And also in work [18] it was demonstrated that using a sapphire substrate it is possible to fabricate long nanowires of GaN using the CVD method. Using gallium and ammonia metals as sources of Ga and N, GaN nanowires were deposited on a sapphire substrate at 900 ° C using a nickel catalyst. The wires they had prepared had a length of several hundred micrometers and diameters from 30 to 150 nm.

The paper [19] describes the photocatalytic activity of GaN nanowires and they have a good ability to photodegrade the organic dye at various pH values even with strong acidity and alkalinity. In addition, the photocatalytic activity of GaN nanowires was compared with the photocatalytic activity of TiO_2 and ZnO nanowires. It was found that the surface area of GaN nanowires was an order of magnitude lower than that of TiO_2 nanowires, the photocatalytic activity of GaN nanowires was slightly higher. Compared to ZnO nanowires, ZnO nanowires were performed better than GaN nanowires at pH 7.0, but in a strong pH range, for example, pH 2.3, the photocatalytic activity of ZnO nanowires rapidly decreased from 70% to 33%, whereas nanowires of GaN increased by 60%.

1D GaN NWs were prepared in a reaction chamber with an air hot reaction with a hot temperature [20]. The growth of 1D GaN was carried out at a growth temperature of 1000 ° C for 1 hour using a Ga_2O3-NH_3 system. NH_3 at a flow rate of 130 cm^3 min-1 was used as the reaction gas and the carrier gas. The substrate was located in the center of the furnace with a series of crucibles mounted on Ga_2O_3. In each experiment, Ga_2O_3 powder was loaded with 0.2 g. For the growth of NW, 100-oriented Si substrates coated with sputtered Au were used. The phase formation of CVD-GaN was analyzed by X-ray diffraction.

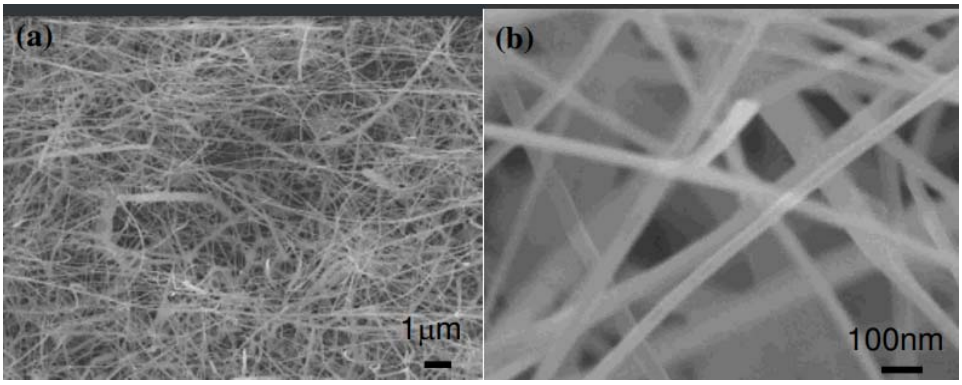

Figure 3 - (a) FESEM images of GaN nanowires synthesized by the CVD method at 1000 ° C on Au / Si substrates for 1 hour with the Ga_2O_3-NH_3 system and (b) magnified image

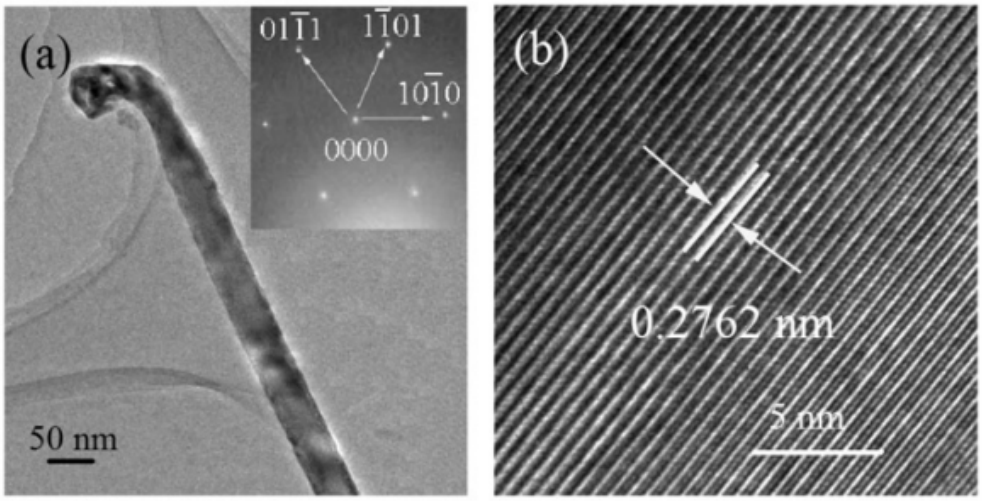

Figure 4 - The TEM, SAED and HRTEM images of GaN nanowires grown at 1150C: (a) TEM and SAED images, and (b) HRTEM images

For the fabrication of GaN nanowires [21] CVD was used. The main materials are powdered Ga_2O_3 (99.99%), a crystal of $NiCl_2$ · 6H2O (99.9%) and NH_3 (99.999%). Thin film of $NiCl_2$ was formed by the immersion method. Unpolished substrate Si (1 1 1) n-type after ultrasonic cleaning was immersed in the $NiCl_2$ · 6H2O ethanol solution with a concentration of about 2%, and dried at 100 ° C. The second step

was to manufacture GaN nanowires in a conventional tube furnace with Ga_2O_3 as a gallium source and NH_3 as a source of nitrogen. When the furnace is increased to a certain temperature (1050 ° C, 1100 ° C and 1150 ° C), 3 g of Ga_2O_3 Si substrate and placed inside a quartz tube in a horizontal tube furnace, and the distance between them was 1 cm, with Ammonia 800 ml min-flow rate 1 was passed into the oven for 40 minutes at a certain temperature. After the ammonia, the gas flow Ar (99.999%) was introduced into the tube for 5 minutes to wash the residual NH_3. After the reaction, the samples were lamellar-light yellow on the surface of the substrate. As the reaction temperature increases, the number of nanowires grows, and the quality improves. Nano drives start to emerge at 1100 ° C and at 1150 ° C have the highest crystallinity with a smooth and clean surface.

HRTEM shows that the distance between crystals nanowires grown at 1150 ° C, corresponds to the (1 0 0) Distance between the crystals of hexagonal GaN monocrystal and that the direction perpendicular to the growth of GaN nanowires (1 0 0).

For the growth of Mn-doped GaN-wires [22] used the metal Ga (purity 99.99%) and powder of Mn (≥99%), with high purity N_2 (99,999%) as the carrier gas and NH_3 (99,9995%) as the reaction gas. For the growth of GaN wires, a substrate of a silicon substrate (100) was used. While the temperature of the tube furnace was increased to reach reaction temperature N_2 (99.999%), NH_3 (99.9995%) and HCl gases (N_2, 10 mole%) were injected. The heating rate was 5 ° C./min, and the holding time was 1 hour. During this time, the temperature and the total flow were regulated in the ranges 950-1400 ° C and 490-625 centimeters, respectively. As the amount of Mn doping increases, the light-emitting wavelength increases to 700 nm (red), the maximum. Moreover, even when the experiment was carried out with the same ratio of the Ga metal to the Mn powder, the light emitting wavelength was 644.4 nm while maintaining the temperature at 1300 ° C.

Carina B. Maliakkal, Azizur Rahman and others [23] were grown GaN NWs using as precursors (Figure 3) organometallic chemical vapor deposition (MOCVD), nickel catalyst and trimethylgallium (TMGa) and ammonia (NH_3).

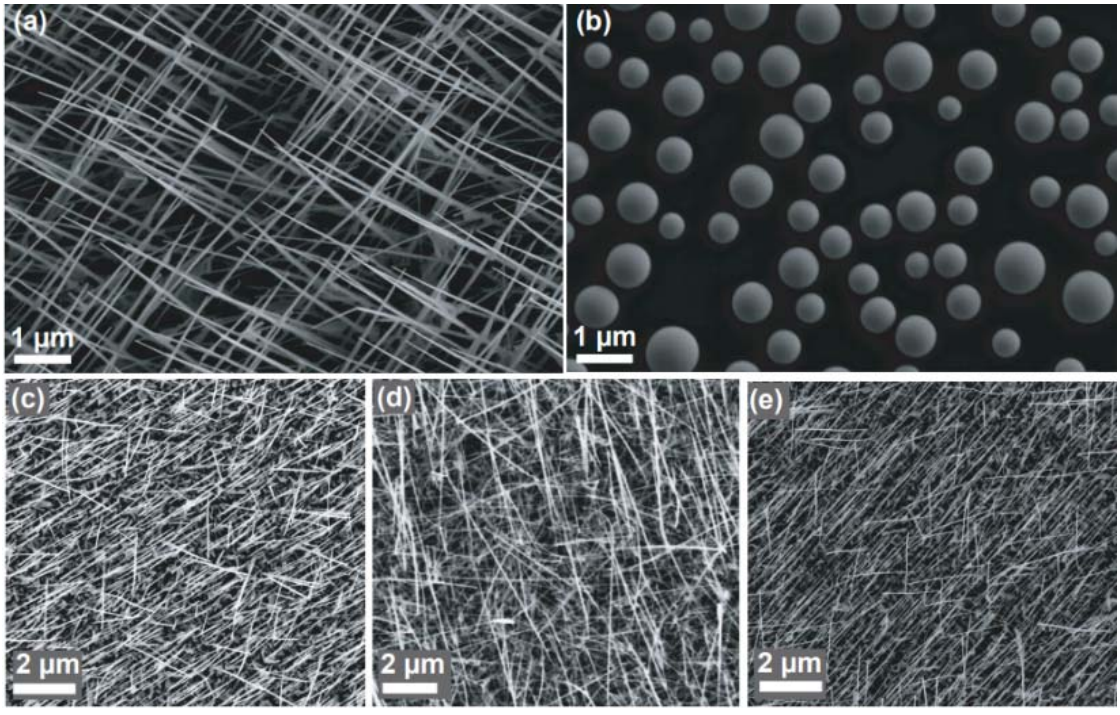

Figure 4 - Growth of GaN-NWs: (a) GaN NWs obtained by growing in medium N_2 (840 ◦C and 150 torr with a flow of 1 cm^3 of NH_3 and a TMGa stream of 2.5 cccm). (b) droplets containing gallium and nickel obtained by growing in an H_2 atmosphere under similar growth conditions. (ce) nickel-catalyzed unsteady GaN NW obtained by rowing under the same conditions (840 ◦C and 150 torr with a flow of 1 cm^3 of NH_3 and a flow of 2 mccm TMGa) in (c) the plane of the c (d) plane and (e) sapphire substrates r-plane [26]. The pressure of 150 torr in medium N_2 and ~840 ° C, with low precursor flow rates and V-III ratio, was optimal for growing thin, not oblique GaN NW.

So, several technologies of the process of growth of GaN obtained by the CVD method were compared. These methods show the progress in the production of GaN. The best way to synthesize nanowires and GaN nanotubes is the direct reaction of metallic gallium Ga vapor with a flowing NH_3 gas. By choosing a gas flow of hydrogen nitride and temperature, it is possible to obtain thinner or thick nanowires and nanotubes.

For semiconductor nanowires, cylindrical geometry and strong two-dimensional retention of electrons, holes and photons make them particularly attractive as potential building blocks for nanoscale electronics and optoelectronic devices [20]. The use of GaN nanowires has been demonstrated by researchers in the following areas: photoelectric devices, light emitting diodes (LED), field effect transistors (FET), lasers, photocatalysts and nano-generators.

The future, GaN will play an increasingly important role in the use of nitride-based semiconductor devices, through the introduction of homoepitaxy and the structure of the device, replacing heteroepitaxy and the currently used device structure. The bulk GaN substrate will grow rapidly over several years, with larger sizes, higher quality and lower cost. To implement mass production and wide application of volumetric GaN substrates, a combination of different growth methods is a possible solution.

REFERENCES

[1] Kul'ment'ev A.I., Kul'ment'eva O.P., Mahmud A.M. Ctruktura i svojstva nanokristallicheskih pokrytij iz nitrida titana, poluchennyh pri nepreryvnom osazhdenii ili ionno-plazmennoj implantacii. UDK 53.06; 621; 62-4.

[2] Othman M.F., Bushroa A.R. Evaluation techniques and improvements of adhesion strength for TiN coating in tool applications: a review// Journal of Adhesion Science and Technology, **2015**, Vol. 29, No. 7, 569–591.

[3] Anna Zaman. Efstathios I. Meletis. Microstructure and Mechanical Properties of TaN Thin Films Prepared by Reactive Magnetron Sputtering/ MDPI journal. Received: 7 October 2017; Accepted: 20 November 2017; Published: 23 November 2017.

[4] Zhitnjak I.Ju. Bychkov I.N. Issledovanie novoj sistemy dostavki himiopreparatov na osnove nanochastic nitrida bora i vozmozhnosti preodolenija s ih pomoshh'ju mnozhestvennoj lekarstvennoj ustojchivosti opuholevyh kletok. Konferencija «Lomonosov 2017». Sekcija «Biofizika i bionanotehnologii».

[5] Sartinska L. L., Frolov a. A., Andreeva a. F., Kasumov a. M., Koval' a. Yu., Urubkov i. V., Timofeeva i. I., and Rud' b. M.. Structure and Optical Properties of Nanosize Boron Nitride Fabricated in Optical Furnace without Catalysts. 1159–1165 (**2008**).

[6] Power GaN Devices. Chapter 1. Properties and Advantages of Gallium Nitride Kyoto Institute of Technology Kyoto. Japan. Daisuke Ueda 20176.

[7] Method of obtaining bulk mono-crystalline gallium-containing nitride, bulk mono-crystalline gallium-containing nitride, substrates manufactured thereof and devices manufactured on such substrates. European patent application 29.12.2010

[8] A two-step method to obtain superplastic silicon nitride with high thermomechanical properties Journal of the European Ceramic Society Volume 17, Issues 2–3, **1997**, Pages 433-437.

[9] HeSun[1] Xiaozhou Zhou[1] Huaizhang Zhang[1] Weixia Tu[1]An. Efficient exfoliation method to obtain graphitic carbon nitride nanosheets with superior visible-light photocatalytic activity. International Journal of Hydrogen Energy Volume 42, Issue 12, 23 March 2017, Pages 7930-7937.

[10] Ryu Hirota, Seiji Nakahata. Group III Nitride Crystal, Method of Its Manufacture, and Equipment for Manufacturing Group III Nitride Crystal. Sumitomo Electric Industries Ltd 2003-10-31.

[11] Bochulia T.V., Sobol O.V. The use of structural engineering for obtaining superhard coatings based of nitrides transition metals. Scientific proceedings xiv international congress "machines. technologies. materials." 2017 - winter session.

[12] Chen X. L., Li J. Y., Cao Y. G. et al., "Straight and smooth GaN nanowires," Advanced Materials, vol. 12, no. 19, pp. 1432–1434, 2000.

[13] Pengan Li, Yihe Liu, and Xianquan Meng . GaN nanowires and nanotubes growth by chemical vapor deposition method at different NH_3 flow rate. Revista Mexicana de F´ısica 62 (**2016**) 219–222.

[14] Kunook Chung, Hongseok Oh, Janghyun Jo, Keundong Lee, Miyoung Kim & Gyu-Chul Yi. Transferable single-crystal GaN thin films grown on chemical vapor-deposited hexagonal BN sheets. NPG Asia Materials volume 9, page 410 (**2017**).

[15] Elena Cimpoiasu, Eric Stern, Guosheng Cheng, Ryan Munden, Aric Sanders, and Mark A. Reed. Electron Mobility Study of Hot-Wall CVD GaN and InN Nanowires. Brazilian Journal of Physics, vol. 36, no. 3B, September, **2006**.

[16] Aleksandr V. Mazalov[a] Damir R. Sabitov[a] Vladimir A. Kureshov[a] Anatoliy A. Padalitsa[a] Aleksandr A. Marmalyuk[ab] Rauf Kh. Akchurin[b]. Research of acceptor impurity thermal activation in GaN: Mg epitaxial layers. Modern Electronic MaterialsVolume 2, Issue 2, June 2016, Pages 45-47.

[17] Chen X. L., Li J. Y., Cao Y. G. et al., "Straight and smooth GaN nanowires," Advanced Materials, vol. 12, no. 19, pp. 1432–1434, **2000**.

[18] Johnson J. C., Choi H. J., Knutsen K. P., Schaller R. D., Yang P., and Saykally R. J. "Single gallium nitride nanowire lasers," Nature Materials, vol. 1, no. 2, pp. 106–110, 2002.

[19] Jung H. S., Hong Y. J., Li Y., Cho J., Kim Y., and Yi G., "Photocatalysis using GaN nanowires," ACS Nano, vol. 2, no. 4, pp. 637–642, 2008.

[20] Dong-Hau Kuoa,*,z and Wun-Hao Wub. Synthesis of Chemical-Vapor-Deposited GaN Nanowires with a „Ga_2O_3 + NH_3 System. Journal of The Electrochemical Society, 156 (1) K1-K3 2009.

[21] Feng Shi, Ying Wang, Chengshan Xue. Synthesis of GaN nanowires by CVD method: effect of reaction temperature. Journal of Experimental Nanoscience Volume 6, 2011 - Issue 3.

[22] Sang-Wook Ui, In-Seok Choi, and Sung-Churl Choi. Optical Properties of One-Dimensional Structured GaN:Mn Fabricated by a Chemical Vapor Deposition Method. Journal of Engineering Volume 2013, Article ID 216259, 6 pages.

[23] Carina B. Maliakkala , A. Azizur Rahmana , Nirupam Hatuia , Bhagyashree A. Chalkea, Rudheer D. Bapata , Arnab Bhattacharyaa. Growth and characterization of GaN NWs on various sapphire substrates. July 7, 2015.

Қ. Асқарұлы[1], Н.К. Манабаев [2]

Қ.И.Сәтбаев атындағы Қазақ ұлттық техникалық зерттеу университеті, Алматы, Қазақстан

CVD ӘДІСІ АРҚЫЛЫ ГАЛЛИ НИТРИДТЕН NWs – АЛУДЫҢ ТЕХНОЛОГИЯЛЫҚ БАРЫСЫ

Аннотация. Галли нитриді, зоналық саңылауы тіке ~3,4 эВ және (GaN) III-V ($A_{III}B_V$) класстағы жартылай өткізгіш болып табылады. GaN өзінің аса жоғары температурада тұрақты және оптикалық қасиеттеріне байланысты өзін ақ жарық шығаратын диодтарда, көк лазерлер мен далалық транзисторларда қолдану және келешекте сәулеленуге қарсы, энергияның, құрылғылардың бағасын түсіруге маңыздылығын көрсетеді. Мақалада дәстүрлі материалдардан қарағанда болашағы мол болып келетін CVD әдісімен алынған GaN - ті зерттреудегі авторландың жұмысына шолу келтіріледі. Материалдардың параметрлерін жақсарту және транзисторлар, жарықдиод және АЖЖ электроникада қолдану үшін материалды алу процесстерін, физикалық қасиеттерін және әр түрлі авторлардың зерттеу нәтижелерін салыстыру жүргізіледі.

Түйін сөздер: GaN, галли нитриді, CVD әдісі, жартылай өткізгіштер, шолу.

Қ. Асқарұлы[1], Н.К. Манабаев [2]

Казахский национальный исследовательский технический университет
им. К.И.Сатпаева, Алматы, Қазақстан

ТЕХНОЛОГИЧЕСКИЕ ПРОЦЕССЫ ПОЛУЧЕНИЯ NWs ИЗ НИТРИДА ГАЛЛИЯ CVD МЕТОДОМ

Аннотация. Нитрид галлия (GaN) представляет собой полупроводник III-V с прямым зонным зазором ~3,4 эВ. GaN имеет важные потенциалы в белых светоизлучающих диодах, синих лазерах и полевых транзисторах из-за его сверхтермической стабильности и превосходных оптических свойств, играя главные роли в будущем освещении, чтобы снизить стоимость энергии и датчики, чтобы противостоять излучению. В статье приводится обзор исследовательских работ авторов по GaN полученнных CVD методом, который гораздо более перспективный материал, чем другие традиционные материалы. Сравниваются физические свойства для улучшения параметров материала, методы получения и результаты исследовательских работ разных авторов для создания светадиодов, транзисторов, СВЧ электронике.

Ключевые слова: GaN, Нитрид галлия, CVD метод, полупроводники, обзор.

Information about authors:

Askaruly KydyR - PhD doctoral student of the 1st academic year for the specialty of 6D072300 - "Technological Physics", the Department of "Technical Physics and Materials Science", Satbayev University. k.askaruly@gmail.com;

Manabaev Nurlan Kasenovich - PhD doctor, the Department of "Technical Physics and Materials Science", Satbayev University. infopresskz@gmail.com

N E W S
OF THE NATIONAL ACADEMY OF SCIENCES OF THE REPUBLIC OF KAZAKHSTAN
PHYSICO-MATHEMATICAL SERIES
ISSN 1991-346X
Volume 4, Number 320 (2018), 66 – 71

UDC 517.927

A.Seitmuratov[1], Z.Seylova[2], S.Tileubay[1], A.Smakhanova[1], M.Serikbol[1], K.Kanibaikyzy[1],

[1]The Korkyt Ata Kyzylorda State University, Kyzylorda;
[2]The Sh.Ualikhanoya Kokshetau State University, Kokshetau
angisin_@mail.ru, stsoias62@mail.ru, Sarsen-00@ mail.ru, Smakanova84@mail.ru,
makpal.serikbol@mail.ru,VIP kundyz@mail.ru

THE USE OF A MATHEMATICAL METHOD OF I. G. FILIPPOVA IN THE SOLUTION OF BOUNDARY VALUE PROBLEMS OF VIBRATIONS OF CYLINDRICAL SHELLS

Abstract: In the present work deals with the questions for problems of torsional and longitudinal vibrations of cylindrical shells of variable thickness in a more general setting that allow to formulate a boundary value problem in the solution of private problems of vibrations of a cylindrical shell under various conditions at the end of the shell. A review of the well-known in the scientific literature studies in the field of vibrations of rods and shells is given in many works. However, these works did not reflect and did not formulate the boundary value problems of oscillation: along with the approximate equations of oscillation, there are no strictly justified boundary conditions at the ends of the rods and shells arising from the developed mathematical approach, and the boundary conditions from the static problems were applied. In addition, the necessary number of initial conditions depending on the order of time derivatives of the required functions was not justified and the areas of applicability of the approximate equations of oscillations were not investigated.

Key words: regional tasks, cylindrical shell, oscillation, torsion vibrations, Bessel function, close equalization, three-dimensional task, variable radius.

Cylindrical shells of variable radius are found in many constructions and buildings. In the scientific literature, the theory of oscillations of cylindrical shells is constructed using the hypothesis of flat sections. Below this problem is solved with the use of a mathematical method used in the works of I. G. Filippov and A. Zh. Seitmuratov.

To derive the equations of oscillation of the rod of variable radius we have the following three-dimensional boundary value problem: equations of motion in potentials

$$N(\Delta\Phi) = \rho\frac{\partial^2\Phi}{\partial t^2};$$

$$M(\Delta\psi_2) = \rho\frac{\partial^2\psi_2}{\partial t^2}; \qquad (1)$$

$$\vec{U}(u_r, u_z) = grad\ \Phi + rot\left[rot(\vec{e}_z), \psi_2\right]$$

boundary conditions on the rod surface

$$\begin{aligned} &F'^2(z)\sigma_{zz} + \sigma_{rr} - 2F'\sigma_{rz} = f_n\Delta_0^2; \\ &(\sigma_{rr} - \sigma_{zz})F'(z) + \sigma_{rz}\left\{1 - \left[F'^2_z(z)\right]^2\right\} = f_{ns_2}\Delta_0^2 \end{aligned} \qquad (2)$$

where $r = F(z)$ - variable radius of the rod; initial conditions are zero. Potentials Φ and ψ_2 let us seek believing

$$\begin{aligned} \Phi &= \int_0^{\infty} \begin{matrix} \sin(kz) \\ -\cos(kz) \end{matrix} \Big\} dk \int_l \Phi_0 \exp(pt) dp; \\ \psi_2 &= \int_0^{\infty} \begin{matrix} \cos(kz) \\ \sin(kz) \end{matrix} \Big\} dk \int_l \psi_{20} \exp(pt) dp \end{aligned} \tag{3}$$

For the values Φ_0, ψ_{20} converted by Fourier and Laplace potentials after substitution (3) in the equation (1) we obtain the ordinary Bessel's differential equations of the imaginary argument

$$\begin{aligned} &\frac{d^2\Phi_0}{dr^2} + \frac{1}{r}\frac{d\Phi_0}{dr} - \alpha^2\Phi_0 = 0; \qquad \alpha^2 = k^2 + \rho p^2 N_0^{-1}(p) \\ &\frac{d^2\psi_{20}}{dr^2} + \frac{1}{r}\frac{d\psi_{20}}{dr} - \beta^2\psi_{20} = 0; \quad \beta^2 = k^2 + \rho p^2 M_0^{-1}(p) \end{aligned} \tag{4}$$

whose solution is limited in the case of $r = 0$, equal

$$\Phi_0 = A_0 I_0(\alpha r); \qquad \psi_{20} = B_0 I_0(\beta r) \tag{5}$$

representing the displacements of u_r, u_z in the form

$$u_\theta = \int_0^{\infty} \begin{matrix} \sin(kz) \\ -\cos(kz) \end{matrix} \Big\} dk \int_{(l)} u_{\theta,0} \exp(pt) dp$$

for $u_{r,0}, u_{z,0}$ obtaining the expression

$$\begin{aligned} u_{r,0} &= \sum_{n=0}^{\infty} \left(A_0\alpha^{2n+2} - kB_0\beta^{2(n+1)}\right) \frac{\left(\frac{r}{2}\right)^{2n+1}}{n!(n+1)!}; \\ u_{z,0} &= \sum_{n=0}^{\infty} \left(kA_0\alpha^{2n} - B_0\beta^{2(n+1)}\right) \frac{\left(\frac{r}{2}\right)^{2n}}{n!} \end{aligned} \tag{6}$$

after decomposition of the Bessel's function in power series of the argument.

Instead of continuous integration A_0, B_0 we introduce a new

$$U_0 = \alpha^2 A_0 - k\beta^2 B_0; \qquad W_0 = kA_0 - \beta^2 B_0 \tag{7}$$

herewith W_0 - the transformed offset of the axis points z of the rod U_0 - s derived from the displacement $u_{r,0}$ along the radial coodinate r also at $r = 0$. In the new variables U_0, W_0 as before $u_{r,0}, u_{z,0}$ will be written in the form

$$u_{r,0}=\sum_{n=0}^{\infty}\left[\left(\alpha^2C_0Q_n^{(0)}+\beta^{2n}\right)U_0-k\alpha^2C_0Q_n^{(0)}W_0\right]\frac{\left(\frac{r}{2}\right)^{2n+1}}{n!(n+1)!};$$
$$u_{z,0}=\sum_{n=0}^{\infty}\left[k^2C_0Q_n^{(0)}U_0-\left(k^2C_0Q_n^{(0)}-\beta^{2n}\right)W_0\right]\frac{\left(\frac{r}{2}\right)^{2n}}{(n!)^2}; \quad (8)$$

By reference (8) to k , p , for displacement u_r, u_z we obtain expressions

$$u_r=\sum_{n=0}^{\infty}\left[\left(\lambda_1^{(1)}CQ_n+\lambda_2^{(n)}\right)U+\frac{\partial}{\partial z}\lambda_1^{(1)}CQ_nW\right]\frac{\left(\frac{r}{2}\right)^{2n+1}}{n!(n+1)!};$$

$$u_z=\sum_{n=0}^{\infty}\left[\frac{\partial}{\partial z}CQ_nU+\left(\frac{\partial^2}{\partial z^2}CQ_n+\lambda_2^{(n)}\right)W\right]\frac{\left(\frac{r}{2}\right)^{2n}}{(n!)^2} \quad (9)$$

где

$$\lambda_1^{(1)}=\rho N^{-1}\left(\frac{\partial^2}{\partial t^2}\right)-\frac{\partial^2}{\partial z^2};\qquad \lambda_2^{(1)}=\rho M^{-1}\left(\frac{\partial^2}{\partial t^2}\right)-\frac{\partial^2}{\partial z^2};$$
$$Q_n=\sum_{q=1}^{n-1}\lambda_1^{(q)}\lambda_2^{(q-n+1)};\qquad Q_0=0;\qquad Q_1=1$$

$\lambda_1^{(1)}$, $\lambda_2^{(1)}$ - describes the propagation of longitudinal and transverse waves along the Z .

Substituting the general solutions of the three-dimensional problem (9) in the boundary conditions (2), to determine U,W we obtain a system of equation

$$L_{1n}(U)+M_{1n}(W)=f_n\Delta_0^2;$$
$$L_{2n}(U)+M_{2n}(W)=f_{ns_2}\Delta_0^2 \quad (10)$$

where operators L_{jn},M_{jn} are equal

$$L_{1n}=\sum_{n=0}^{\infty}\frac{\left(\frac{F}{2}\right)^{2n}}{(n!)^2}\left\{\left[-2CQ_n\frac{\partial^2}{\partial z^2}+(1-C)\lambda_1^{(n)}-\frac{1}{n+1}\left(\lambda_1^{(n)}-CQ_n\frac{\partial^2}{\partial z^2}\right)\right]+\left(F_z'\right)^2\left[2CQ_n\frac{\partial^2}{\partial z^2}-(1+C)\lambda_1^{(n)}\right]+\right.$$
$$\left.+\frac{FF_z'}{n+1}\left[CQ_n\left(\lambda_2^{(1)}-\frac{\partial^2}{\partial z^2}\right)+(1+C)\lambda_1^{(n)}\right]\frac{\partial}{\partial z}\right\};$$

$$L_{2n}=\sum_{n=0}^{\infty}\frac{\left(\frac{F}{2}\right)^{2n}}{(n!)^2}\left\{F_z^{'}\left[2\lambda_1^{(n)}-4CQ_n\frac{\partial^2}{\partial z^2}-\frac{1}{n+1}\left(\lambda_1^{(n)}-CQ_n\frac{\partial^2}{\partial z^2}\right)\right]\frac{F\left(F_z^{'}\right)^2}{2(n+1)}\left[CQ_n\left(\lambda_2^{(1)}-\frac{\partial^2}{\partial z^2}\right)+(1+C)\lambda_1^{(n)}\right]\frac{\partial}{\partial z}\right\}; \quad (11)$$

$$M_{1n}=\sum_{n=0}^{\infty}\frac{\left(\frac{F}{2}\right)^{2n}}{(n!)^2}\left\{\left[-2CQ_n\lambda_1^{(1)}+(1-C)\lambda_1^{(n)}+\frac{1}{n+1}CQ_n\lambda_1^{(n)}\right]\frac{\partial}{\partial z}+\left(F_z^{'}\right)^2\right.$$

$$\left.\times\left[2CQ_n\lambda_1^{(1)}-(1-C)\lambda_1^{(n)}\right]\frac{\partial}{\partial z}+\frac{FF_z^{'}}{n+1}\left[CQ_n\left(\lambda_2^{(1)}-\frac{\partial^2}{\partial z^2}\right)\lambda_1^{(n)}-(1-C)\lambda_1^{(n+1)}\right]\right\}$$

$$f_n^{(1)}=M^{-1}f_n\Delta_0^2; \qquad f_{ns_2}^{(1)}=f_{ns_2}\Delta_0^2;$$

$$\Delta_0^2=1+\left(F_z^{'}\right)^2$$

The equations (10) are the general equations of longitudinal oscillation of a rod of variable radius.

Due to the complexity of the equations (10), we obtain from them the approximate equations of the longitudinal vibration of the rod. Limited to the first summands in the series of operators (11), we obtain a known equation for the constant radius rod

$$\frac{1}{\tilde{n}_{cm}^2}\frac{\partial^2 W}{\partial t^2}-\frac{\partial^2 W}{\partial z^2}=0; \qquad \left(f_n=f_{ns_2}=0\right) \quad (12)$$

in this case, the speed of the longitudinal wave of compression in the rod is equal to

$$c_{cm}^2=b\left(3a^2-4b^2\right)*\left(a^2-b^2\right)^{-1}$$

and is given in various textbooks and books.

If we limit ourselves to the first two terms in the series of operators (11), we obtain a refined equation that generalizes the equation (12).

If the rod of variable radius, then from the general equations of oscillation (10) we obtain the simplest equation of the second order

$$\rho_0(z)W+\rho_1(z)\frac{\partial W}{\partial z}+\rho_2(z)\frac{\partial^2 W}{\partial z^2}=\rho N^{-1}\rho_3(z)\frac{\partial^{2W}}{\partial t^2} \quad (13)$$

where the variable coefficients of the $\rho_j(z)$ in the derivative of W are equal

$$\rho_0(z)=2\left[(1-C)F(z)F^{'''}(z)F^{'}(z)-(1+C)F^{''}(z)\right]$$

$$\rho_1(z)=\left[\frac{1}{2}(1-C)^2F_z^{'}()-(5+C)F_z^{'2}(z)+\frac{1}{2}(1-C^2)F_z^{'5}(z)--(1+C)(3+C)F(z)F_z^{'}(z)F_z^{''}(z)5-\right.$$

$$-\frac{1}{2}(1-C^2)F_z^{''}(z)+(1-C^2)\,F_2^{'2}(z)F_z^{''}(z)\left(FF_z^{'}(z)-\frac{5}{2}F\right)+(1-C^2)\left(F_z^{''2}(z)+F_z^{'}(z)F_z^{'''}(z)\right)$$

$$\rho_2(z)=\left\{-\frac{1}{2}\left[(1+C)^2-C(1-C)\right]F(z)+\frac{1}{2}(3C^2-5C-5)F(z)F_z^{'2}(z)+\frac{5}{2}(1-C)^2F(z)F_z^{'4}(z)+\right.$$

$$\left.+3(1-C^2)F^2(z)F_z^{'2}(z)F_z^{''}(z)\right\}$$

$$\rho_3(z)=\left[\frac{C}{2}(1-C)F(z)-\frac{1}{2}(C^2-3C+1)F(z)F_z'^2(z)-(1-C^2)F(z)F_z'^4(z)-(1-C^2)F^2(z)F_z'^2(z)F_z''(z)\right] \quad (14)$$

REFERENCES

[1] Filippovو I.G., S.I. Filippov, **1995**. Dynamic stability theory of rods. Proceedings of the Russian-Polish seminar. Theoretical Foundations of construction. Warsaw, pp.63 -69.

[2] Filippov, I.G., **1979**. An approximate method for solving dynamic viscoelastic media. – PMM, 43(1): 133 -137.

[3] Filippov, I.G., S.I Filippov, V.I. Kostin, **1995**. Dynamics of two-dimensional composites. - Proceedings of the International Conference on Mechanics and Materials, USA, Los Angeles, pp.75 -79.

[4] Seytmuratov, A.Zh., **2010**. Determination of natural frequencies of the plate. Bulletin Treasury Series mathematics, mechanics, computer science, 4 (67): 120.

[5] Seytmuratov, A.Zh., **2010**. The impact of the moving load on the surface of a layered elastic half-plane. Herald KazNPU., 3: 112-11

[6] Brunelle, E.J., **1977**. Buckling of transversely isotopic Mindlen plates, AIAA, 9(6): 1018-1022.

[7] Bergman, G.G., **1981**. Elastic waves propagation in fluid saturated porous media G. Asoust. Soc. America., 2: 416-424.

[8] Bowen, P.M., **1980**. Incompressible porous media models by use of the theory mixtures. Int. J. Engng. Sci., 18: 1129-1148.

[9] de Boer, R., **2000**. Theory of porous media. Berlin: Springer.

[10] Ellsiepen, P., **1999**. Zeit- und ortsadaptive Verfahren angewandt auf Mehrphasenprobleme poroser Medien. Bericht Nr. II-3, Universitat Stuttgart, Institute for Mechanik, Lehrstuhl II.

[11] Diebels, S., W. Ehlers, **1996**. Dynamic analysis of a fully saturated porous medium accounting for geometrical and material non-linearities. Int. J. Num. Methods Engng 39: 81-97.

[12] Diebels, S., W. Ehlers, B. Markert, **2001**. Neglect of the fluid-extra stresses in volumetrically coupled solid-fluid problems. ZAMM 81, S521-S522.

[13] Umbetov, U., A.Zh. Seytmuratov, **2012**. Decomposition approach to the modeling of seismic resistance of building structures. M., PAE. Modern high technologies, 6: 43.

А.Ж.Сейтмұратов[1], З.Т.Сейлова[2], С.Ш.Тілеубай[1], А.Қ.Смаханова[1], М.С.Серікбол[1] , Қ.Қанибайқызы[1]

[1]Қорқыт Ата атындағы Қызылорда мемлекеттік университеті, Қызылорда қ.
[2]Ш.Уалиханов атындағы Көкшетау мемлекеттік университеті, Көкшетау қ.

ЦИЛИНДІРЛІК ҚАБЫҚШАЛАРДЫҢ ШЕТТІК ТЕРБЕЛІС ЕСЕБІ ҮШІН И.Г.ФИЛИППОВТЫҢ МАТЕМАТИКАЛЫҚ ШЕШУ ӘДІСІН ҚОЛДАНУ

Аннотация: Берілген мақалада айналмалы және көлбеу цилиндірлік қабықшалар есебінен туындайтын сұрақтар жайлы мәселе қозғалады. Негізінен қабықшалар айналасында болатын әр-түрлі шарттарға байланысты шеттік есептерді қалыптастыру мақсатында цилиндірлік қабықшасының айнымалы қалыңдығына байланысты жалпы есебі қарастырылады. Осыған дейінгі жасалған сырықтар мен қабықшалар тербелісі жұмыстарына көз жүгірте отырып, қарастырылған тербеліс шеттік есептерінде нақты қатаң түрде математикалық тұжырымы жеткіліксз көрсетілген. Сондықтан бұл жұмыста белгілі ғалым И.Г.Филипповтың тербеліс есептерін шешудегі математикалық әдісін қолдандып тербеліс теңдеулерінің жуық шамасының қолдану шарттары анықталды.

Түйін сөз: шеттік есеп, цилиндірлік қабықша, тербеліс, айналмалы тербеліс, Бессел функциясы, жуық теңдеу, үш өлшемді есеп, айнымалы радиус.

А.Ж. Сейтмуратов[1], З.Т.Сейлова[2], С.Ш.Тилеубай[1], А.К.Смаханова[1], М.С.Серікбол[1], Қ.Қанибайқызы[1]

[1]Кызылординский государственный университет им.Коркыт Ата, г.Кызылорда
[2]Кокшетауский государственный университет им.Ш.Уалиханова, г.Кокшетау

ПРИМЕНЕНИЕ МАТЕМАТИЧЕСКОГО МЕТОДА И.Г.ФИЛИППОВА ПРИ РЕШЕНИИ КРАЕВЫХ ЗАДАЧ КОЛЕБАНИЯ ЦИЛИНДРИЧЕСКИХ ОБОЛОЧЕК

Аннотация: В настоящей работе рассматриваются вопросы для задач крутильного и продольного колебаний цилиндрических оболочек переменной толщины в более общей постановке, которые позволяют формулировать краевые задачи при решении частных задач колебания цилиндрической оболочки при различных условиях на торце оболочки. Обзор известных в научной литературе исследований в области колебаний стержней и оболочек приведён во многих работах. Однако в этих работах не нашли отражения и не были сформулированы краевые задачи колебания: наряду с приближёнными уравнениями колебания отсутствуют строго обоснованные граничные условия на торцах стержней и оболочек, вытекающие из развиваемого математического подхода, а применялись граничные условия из задач статики. Кроме того, не обосновывалось необходимое число начальных условий в зависимости от порядка производных по времени от искомых функций и не исследовались области применимости приближённых уравнений колебаний.

Ключевые слова: краевые задачи, цилиндрическая оболочка, колебание, крутильная колебания, функция Бесселя, приближенные уравнение, трехмерная задача, переменный радиус.

Information about authors:

Seitmuratov Angisin – Doktor of Physical and Matematical Sciences, Professoz, The Korkyt Ata Kyzylorda State University. Kyzylorda

Seyloya Zoya Tuleubaebna – kandidate of pedagogical sciences,associate professor, The Sh.Ualikhanoya Kokshetau State University, Kokshetau.

Tileubay Sarsenkul Shaykamalqız- kandidate of pedagogical sciences, The Korkyt Ata Kyzylorda State University, Kyzylorda.

Smakhanova Aizhan Korganbekovna- Master degree of mathematical sciences, The Korkyt Ata Kyzylorda State University, Kyzylorda.

Serikbol Makpal Serikbolkyzy- Master degree of mathematical sciences, The Korkyt Ata Kyzylorda State University, Kyzylorda.

Kanibaikyzy Kundyzay – Master degree of pedagogical sciences, The Korkyt Ata Kyzylorda State University, Kyzylorda.

N E W S
OF THE NATIONAL ACADEMY OF SCIENCES OF THE REPUBLIC OF KAZAKHSTAN
PHYSICO-MATHEMATICAL SERIES
ISSN 1991-346X
Volume 4, Number 320 (2018), 72 – 78

UDC 524.31

V. M. Tereschenko

Fesenkov Astrophysical Institute
volter2307@mail.ru

SPECTROPHOTOMETRICAL STANDARDS 8^m-10^m. 1. EQUIPMENT, METHODS AND FIRST RESULTS

Abstract. Justification of the task of creation a network the spectrophotometric of standards 8^m-10^m is given. Standards of this brightness are necessary for calibration of spectral observations using large telescopes. Selection of stars – candidates in spectrophotometric standards and primary standards was made. As candidates in the standards selected stars of spectral classes A and B which are located in the equatorial zone with declination ±3˚. The used equipment - a new CCD spectrograph is briefly described. Dispersing element of a spectrograph is the concave toroidal grating which simultaneously serves as collimator and as camera. The spectrograph operates in the slitless mode. As the receiver of radiation the CCD camera ATIC-490EX was used. The new spectrograph allows to investigate an energy distribution in the spectra of much dimer stars than in case of observations with spectrometers. Observations on the telescopes AZT-8 and Zeiss-600 at Kavenskoe plato carry out. The differential method of observations was used. Processing of CCD-spectrograms and numerical reductions detail is described. The energy distribution in spectral region 340 – 660nm is investigated, spectral resolution of the obtained data be 5 nm, the relative standard deviation - from 3 to 6%. The absolute energy distribution in spectra of two candidates for standards is presented.

Key words: stars, spectrophotometrical standards, CCD spectrograph, methods of observations.

УДК 524.31

В. М. Терещенко

ДТОО «Астрофизический Институт им Фесенкова», Алматы, Казахстан

СПЕКТРОФОТОМЕТРИЧЕСКИЕ СТАНДАРТЫ 8^m-10^m . 1. АППАРАТУРА, МЕТОДИКА И ПЕРВЫЕ РЕЗУЛЬТАТЫ

Аннотация. Приведено обоснование задачи создания сети спектрофотометрических стандартов 8^m-10^m. Стандарты данного блеска необходимы для калибровки спектральных наблюдений на крупных телескопах. Сделана выборка звезд-кандидатов в спектрофотометрические стандарты и первичных стандартов. В качестве кандидатов в стандарты выбраны звезды спектральных классов А и В, которые расположены в экваториальной области со склонением ±3˚. Кратко описана используемая аппаратура - новый ПЗС-спектрограф. Диспергирующим элементом спектрографа является вогнутая тороидальная решетка, которая одновременно служит коллиматором и камерой. Спектрограф работает в бесщелевом режиме. В качестве приемника излучения используется ПЗС-камера ATIC-490EX. Новый спектрограф позволяет исследовать распределение энергии в спектрах намного более тусклых звезд, чем со спектрометрами. Наблюдения выполнены на телескопах АЗТ-8 и Цейсс-600. Использовался дифференциальный метод наблюдений. Подробно описаны метод обработки ПЗС- спектрограмм и численные редукции. Распределение энергии исследуется в спектральной области 340 - 660нм, спектральное разрешение полученных данных составляет 5нм, относительная с.к.о. - от 3 до 6%. Представлено абсолютное распределение энергии в спектрах двух кандидатов в стандарты.

Ключевые слова: звезды, спектрофотометрические стандарты, ПЗС-спектрограф, методы наблюдений.

Введение. Исследование распределения энергии в спектрах звезд - традиционная тематика Астрофизического института им. Фесенкова, а созданный в институте спектрофотометрический каталог [1] продолжает оставаться самым массовым в мире. Спектральное распределение энергии используется для определения физических параметров звезд и межзвездной среды. Кроме того, звезды с известным распределением энергии используются для стандартизации спектрофотометрических наблюдений самых разных небесных тел и для калибровки аппаратуры. Обычно в качестве спектрофотометрических стандартов служат звезды ранних спектральных классов. В их спектрах имеются протяженные участки, свободные от сильных спектральных линий. Спектрофотометрические данные представляют в двух видах: «сплошном» и «скважном». В «сплошном» данные о внеатмосферной освещенности приводятся непрерывно через определенный интервал, равный интервалу усреднения, т.е. в гистограммном виде. В «скважном» виде данные приводятся для избранных длин волн. В настоящее время сплошное внеатмосферное распределение энергии в интегральном спектре изучено в спектрах около полутора тысяч звезд. Практически все они ярче 6 величины [1-6]. В литературе и в базе данных SIMBAD имеется несколько десятков звезд-стандартов 7^m - 8^m [7-10] и всего несколько - более слабых. Стандартов же должно быть как можно больше, так как от их количества зависят производительность наблюдений и точность получаемых данных. Очевидно, что при наблюдениях на крупных телескопах требуются более слабые стандарты. Поэтому добавление к имеющимся в наличии слабым стандартам даже нескольких звезд имеет смысл и задача создания слабых спектрофотометрических стандартов является актуальной. Можно сказать, что их создание – «вечная» задача, так как со временем требуются все более слабые стандарты, более точные, с более высоким спектральным разрешением и охватывающих все более широкий интервал спектра. Мы решили расширить список стандартов в сторону более слабых по сравнению с имеющимися в каталогах звездах и создать сеть спектрофотометрических стандартов 8^m-10^m. Настоящая работа является первой из планируемой серии публикаций, посвященных ее созданию.

Аппаратура. Распределение энергии в спектрах звезд в указанных выше работах [1-10] было получено с помощью одноканальных спектрометров, в которых приемником излучения служили фотоумножители. Для исследования распределения энергии в спектрах звезд 8^m-10^m нами специально был изготовлен спектрограф [11], в котором приемником излучения является ПЗС-камера. Подчеркнем, что специальных исследований распределения энергии в спектрах звезд с помощью ПЗС-спектрографов мы не встречали. По-видимому, отсутствие таких исследований связано не столько с потерей их актуальности, сколько с методическими трудностями, возникающими при их осуществлении. Стоит отметить, что точность регистрации потоков излучения ПЗС-камерой по сравнению с фотоумножителями более низкая [12]. Вместе с тем, стандартизация спектральных наблюдений различных небесных объектов, полученных с ПЗС-спектрографами, в отдельных участках спектра выполняется довольно часто (см., например, [13-14]).

В нашем спектрографе для абсолютных измерений (САИ) диспергирующим элементом служит тороидальная дифракционная решетка. Постоянная решетки – 150 штрихов/мм, размер заштрихованной части решетки - 20*20мм, фокусное расстояние - около 242 мм. Дисперсия спектрографа составляет 25нм/мм, размер поля - 20мм. Спектрограф работает, по сути, в бесщелевом режиме, входная щель имеет ширину около 1 мм, что заведомо больше размеров изображений звезд для телескопов с фокусным расстоянием менее 20м. Широкие щель или диафрагма требуются для абсолютных измерений – чтобы не было виньетирования пучка. Так как спектральное разрешение данных составляет всего 5нм, то бесщелевой вариант вполне приемлем. Главное достоинство используемой решетки в том, что она обеспечивает плоский спектр в области от 300 до 800нм. Это ее свойство позволяет использовать в качестве приемника излучения ПЗС-матрицы. В качестве приемника излучения служит ПЗС-камера ATIK-490EX. Основные параметры матрицы данной камеры следующие: число пикселей - 3380*2704, размер пикселов - 3.69*3.69 мкм, длина матрицы - 12.5мм. Охлаждение камеры - на 25К ниже температуры воздуха, спектральная область чувствительности – от 300 до 800мк, шум считывания - 5е.

Подробное описание спектрографа приведено в работе [11]. Заметим, что светосила САИ равна 1:10 и первоначально он был рассчитан на работу с 1-метровыми телескопами «Цейсс-1000»,

расположенных на высокогорной ТШАО. В связи с установкой на этих телескопах оптических редукторов, наблюдения выполнены на телескопах АЗТ-8 и Цейсс-600, которые находящихся на Каменском плато. На плато прозрачность атмосферы хуже, что снизило точность полученных данных. К недостаткам САИ можно отнести то, что размер матрицы используемой камеры не позволяет одновременно охватить всю доступную измерениям область спектра. При замене ПЗС-камеры на более крупную, этот недостаток САИ устранится.

Выборка звезд-кандидатов в стандарты и первичных стандартов. В качестве слабых спектрофотометрических стандартов мы выбрали 24 звезды ранних спектральных классов 8-10 величины, расположенных равномерно вдоль экватора ($\delta = \pm 3^{\circ}$). Данный выбор обусловлен двумя факторами. Во-первых, спектры A-B- звезд имеют протяженные участки, которые свободны от сильных линий. Их удобно использовать для стандартизации наблюдений и калибровки аппаратуры. К тому же, результаты стандартизации и калибровки практически не зависят от спектрального разрешения используемого спектрографа. Во-вторых, стандарты в экваториальной зоне можно использовать при наблюдениях в разных полушариях Земли. Естественно, что при выборке должно соблюдаться основное требование к любым стандартам - они должны быть непеременными. Список звезд-кандидатов в стандарты представлен в таблице 1.

Таблица 1 - Список и характеристики звезд-кандидатов
в спектрофотометрические стандарты 8^m - 10^m

Hip (Tyc)	HD (BD)	α 2000	δ 2000	V	B-V	Sp
1241	1112	$00^h\ 15^m\ 27.3^s$	-03° 39' 15"	9.105^m	-0.066^m	B9V
9152	12021	01 57 56.1	-02 05 58	8.843	-0.071	A0
13917	18571	02 59 16.8	01 14 40	8.632	+0.038	A0V
18243	24520	03 54 07.0	02 11 02	8.626	+0.118	B9
20778	28190	04 27 03.5	04 16 51	9.021	+0.125	B9V
24053	289997	05 10 07.8	-00 16 58	9.964	+0.077	B8V
29258	42334	06 10 08.7	00 42 36	9.327	+0.025	B8III
32634	50087	06 51 40.6	00 19 36	9.084	+0.047	B9III
38123	63367	07 48 44.4	01 56 21	8.990	+0.060	B9V
Tyc210-680	BD+01 2119	08 32 43.6	00 53 49	10.13	-0.07	A0
48704	86027	09 55 59.6	02 47 55	8.356	-0.029	A0V
55011	97917	11 15 48.3	-02 17 58	8.880	-0.145	B9
Tyc281-353	BD+01 2668	12 13 25.3	01 09 22	10.29	-0.09	B5?
66872	BD+02 2711	13 42 19.0	01 30 18	10.263	-0.11	B5
Tyc317-603	BD+02 2790	14 14 25.9	01 47 58	10.11	0.03	A0
74972	136161	15 19 14.7	-02 10 02	8.891	0.330	A3V
82133	151355	16 46 47.0	02 12 34	8.826	-0.092	B4/5V
87417	162628	17 51 52.6	02 53 59	8.258	0.192	B9.5V
92559	174648	18 51 41.0	-01 45 35	8.827	0.118	B9.5V
Tyc479-625	185296	19 38 21.0	01 30 14	9.741	0.210	B9II
101541	BD-03 4950	20 34 43.6	-02 41 44	10.010	+0.141	A0
Tyc 531-232	BD+01 4436	21 10 11.5	02 14 20	9.99	+0.03	A0
112149	215112	22 42 58.0	-02 40 57	8.240	-0.041	B9V
Tyc 581-756	BD+02 4661	23 23 38.20	02 55 57	10.05	0.38	F2

Самый яркий кандидат в стандарты - звезда HD 151355 ($V=8.25^m$), самый слабый – BD+02 2711 ($V=10.37^m$). Абсолютное большинство звезд списка удовлетворяет поставленным требованиям. Только одна звезда расположена вне выделенной полосы и только одна звезда имеет спектральный класс F2.

Как и при создании всех каталогов [1-10], наблюдения выполнены дифференциальным методом. Звезды-кандидаты в спектрофотометрические стандарты привязывались к звездам, для которых было заранее известно спектральное распределение энергии (их можно назвать

вторичными стандартами). В качестве последних было взято 9 A0V-звезд 7^m-8^m из каталога [1], которые также расположены в экваториальной области. Их список и основные характеристики приведены в таблице 1. Абсолютное распределение для них в областях, занимаемых бальмеровскими линиями, было предварительно графически интерполировано. Ввиду ограниченного объема статьи мы здесь не приводим интерполированных данных.

Таблица 2 - Список вторичных спектрофотометрических стандартов и их характеристики

№п/п	HD	α_{2000}	δ_{2000}	π(mas)	V	B-V	Sp
1	009716	$01^h\ 35.1^m$	-02° 20'	5.29	7.43^m	0.16^m	A0V
2	023009	03 41.6	-00 10	6.20	8.64	0.21	A0V
3	036117	05 29.5	-00 03	6.09	7.99	0.10	A0
4	075620	08 51.1	00 28	4.01	7.97	0.11	A0V
5	100237	11 32.0	-01 47	3.31	7.34	-0.01	A0V
6	121513	13 55.8	01 31	3.25	8.00	0.11	A0V
7	147470	16 22.9	00 30	7.19	7.67	0.10	A0V
8	185198	19 37.9	01 30	1.60	7.32	0.19	B9.5V
9	216261	22 51.6	-01 49	4.02	8.16	0.16	A0V

Методы наблюдений и обработки. Наблюдения выполнены методом равных высот, который позволяет использовать в редукциях за поглощение в атмосфере среднее значение коэффициента спектральной прозрачности для места наблюдений. Его значения были взяты из работы [11], в которой они приводятся для летнего и зимнего сезонов. Разность воздушных масс ΔM между записями стандарта и кандидатом в стандарты в среднем не превышала 0.10. Каждая звезда наблюдалась от 4 до 7 раз. По разным причинам (аппаратурным и атмосферным) часть записей спектров была выброшена. Длительность экспозиций составляла от 100 до 500 секунд. Температура камеры и биннинг для программных и стандартных звезд должны быть одинаковыми. Режимы записей их спектров отличаются только экспозицией. Звезды, для которых получено абсолютное распределение энергии путем привязки к вторичным стандартам, можно назвать третичными стандартами.

Кратко опишем процедуру обработки кадров и полученных по ним данных. Подробно она изложена в составленной нами инструкции. Результатом наблюдений с САИ являются «сырые» кадры спектров звезд в формате “FIT”, которые необходимо «довести до числа». Пример одного из полученных кадров приведен на рисунке 1. Кадры обрабатываются в пакете «MaxIm DL– 6» стандартным способом. Первый этап обработки отснятых кадров начинается с их очистки от «горячих» пикселов, порождаемых дефектами матрицы и космическими лучами. Второй этап - так называемая калибровка. Это стандартная процедура, позволяющая с помощью дополнительных кадров (плоского поля, биасов и дарков) учесть все аппаратурные искажения. В нашем случае плоское поле не записывалось ввиду однородности используемой матрицы. Третий этап – вычитание фона и преобразование кадров в числовой массив в пакете Excel. В итоге в памяти компьютера мы имеем набор численных значений накопившихся на матрице зарядов (импульсов), которые пропорциональны потокам от звезд в соответствующих длинах волн. Программа Excel позволяет его представить в виде графика - регистрограммы. Четвертый этап - отождествление на регистрограмме длин волн. Оно осуществляется вручную, «на глаз». Курсором наводимся на центр депрессии в спектре , вызванной той или иной линией. Для звезд ранних спектральных классов реперами служат бальмеровские линии Hα, Hβ и Hγ, для звезд класса G - линии H и K. Очень ответственным является следующий этап - разбиение на 50-ангстремные интервалы. Дисперсия спектрографа - практически линейная. В нашем спектрографе 50A соответствует 25.5 пиксела. Из-за небольших сдвигов спектра при разных положениях спектрографа начало первого 50-A интервала необходимо вычислять для каждого кадра. Заранее была заготовлена таблица из номеров пикселей, соответствующая началу и концу 50-ангстемных интервалов (шаблон). Маркер монитора выставлялся на центр линии Hβ. Номер пикселя центра линии фиксировался и таблица (шаблон) соответственно целиком сдвигалась в ультрафиолетовую или красную область спектра. Точность отождествления - 1-2 пикселя (2-5A). Для вторичных стандартов требуется еще одна операция - необходимо выполнить интерполяцию непрерывного спектра в участках спектра

занимаемых бальмеровскими линиями. Интерполяция осуществляется после разбивки регистрограммы на 50-ангстемные интервалы. Интерполировались табличные значения, их значения контролировались графически, - «на глаз», что требует определенного навыка. Ввиду краткости интервалов такая интерполяция проводится достаточно уверенно. Естественно, что ручной способ интерполяции требует значительного времени, но в нашем случае это оптимальный вариант. Пример регистрограммы приведен на рисунке 2.

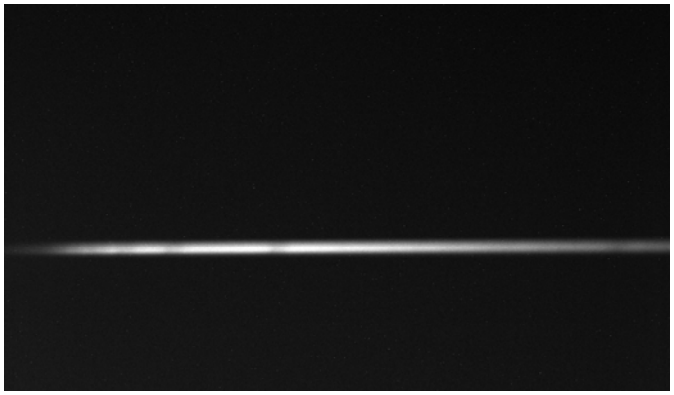

Рисунок 1 - Спектрограмма HD1112 (9.10^{m}; B9V)

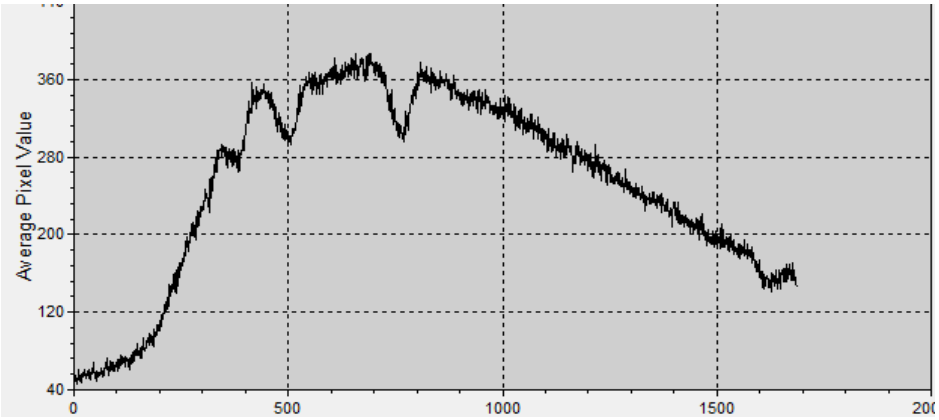

Рисунок 2 - Регистрограмма HD24520 ((8.63^{m}; B9)

Численные редукции. Отсчеты внутри 50-ангстремных интервалов суммируются и нормируются, то есть усредняются и регистрограмма превращается в гистограмму. Все вычисления и численные редукции выполняются в пакете Excel.

Редукции за различие экспозиций звезды и стандарта и за разное поглощение излучения от них в атмосфере Земли выполнены по классической формуле дифференциальной спектрофотометрии:

$$E_*(\lambda) = E_{st}(\lambda) \cdot [I_*(\lambda) / Ist(\lambda)] \cdot [\Delta t_{st} / \Delta t_*] \times p_{cp}(\lambda)^{-\Delta M}, \quad (1)$$

где $E_*(\lambda)$ и $E_{st}(\lambda)$ – внеатмосферные значения спектральных плотностей энергетических освещенностей, создаваемых звездой и стандартом;

$I_*(\lambda)$ и $I_{st}(\lambda)$ - усредненные в интервале 5нм отсчеты на звезду и стандарт (при привязке к двум записям стандарта – среднее из двух наблюдений); Δt_{st} и Δt_* - длительность экспозиций в секундах на стандарт и звезду; $p_{cp}(\lambda)$ – среднее значение коэффициента прозрачности для места наблюдения; $\Delta M = M_{st} - M_*$ - разность воздушных масс между стандартом и звездой.

В редукциях для вторичных стандартов мы брали значения освещенностей и отсчетов не для интегрального спектра, а для квазинепрерывного. Для исследуемых звезд берутся интегральные

отсчеты внутри интервалов с теми же номерами пикселей (длин волн центров 50А интервалов). Результаты наблюдений для двух спектрофотометрических стандартов промежуточного блеска HD1112 и HD 12021 приведены в таблице 3. Точность полученных данных, характеризуемая относительной среднеквадратичной ошибкой, составляет от 3 до 6%. Для звезд 9-10 величины такую точность абсолютных измерений можно считать вполне удовлетворительной.

Таблица 3- Распределение энергии в спектрах E(λ) для HD1112 и HD 12021 (единицы - 10^{-7}wt/m^{2}m)

λ, A	1112	12021	λ, A	1112	12021	λ, A	1112	12021
3425	80.5	178	4525	141.6	206	5625	80.1	108
3475	81.8	176	4575	137.0	200	5675	78.7	103
3525	84.9	178	4625	135.0	196	5725	75.2	101
3575	80.5	165	4675	130.6	189	5775	73.5	97
3625	79.9	169	4725	125.4	181	5825	72.0	96
3675	81.8	166	4775	121.9	172	5875	72.4	94
3725	92.8	173	4825	118.0	160	5925	68.8	91
3775	106.1	192	4875	111.3	154	5975	67.4	89
3825	131.0	226	4925	108.8	155	6025	66.4	88
3875	159.6	265	4975	109.3	154	6075	64.7	83
3925	168.1	272	5025	107.0	149	6125	63.2	82
3975	186.1	299	5075	105.2	145	6175	60.4	81
4025	191.3	309	5125	102.2	141	6225	57.5	76
4075	186.8	292	5175	99.7	137	6275	57.8	74
4125	178.6	274	5225	96.3	133	6325	56.2	72
4175	174.2	270	5275	93.6	127	6375	54.8	71
4225	171.6	263	5325	91.0	124	6425	54.5	68
4275	169.2	249	5375	88.4	121	6475	54.4	66
4325	158.8	229	5425	87.7	117	6525	50.5	63
4375	150.0	224	5475	86.9	115	6575	48.0	60
4425	146.4	220	5525	83.5	111	6625	47.0	63
4475	145.0	213	5575	80.5	111	6675	47.5	63

Работа выполнена при поддержке программы целевого финансирования BR05236322 Министерства Образования и науки РК.

ЛИТЕРАТУРА

[1] Харитонов А. В., Терещенко В. М., Князева Л. Н. // Спектрофотометрический каталог звезд / Алма-Ата. - «Казак Универсітеті». - 2011. - 304 с.

[2] Волошина И. Б., Глушнева И. Н., Дорошенко В. Т., Колотилов Е.А., Моссаковская Л. И., Овчинников С.Л., Фетисова Т.С. Под ред. И. Н. Глушневой // Спектрофотометрия ярких звезд / М. Наука. 1982. - 256 с.

[3] Alekseeva G. A., Arkharov A. A., Galkin V. D., Hagen-Thorn E. I., Nikanorova I. N., Novikov V. V., Novopashenny V. B., Pakhomov V. P., Ruban E. V., Shchegolev D. E. // The Pulkovo spectrophotometric catalog of bright stars in the range from 320 to 1080nm / Baltic astronomy - 1996. - V. 5. - № 4. - P. 603-838.

[4] Н.С. Комаров, В.А. Позигун, С.И.Белик, А. В. Драгунова, В.Ф. Гопка, Н.Н. Закожурникова, Л.Э. Канцен, В.Ф. Карамыш, Т.В. Мишенина, Л.Ф. Орлова, А.Ф. Переверзенцев, Т.А. Руссо, А.Г. Черкас // Спектрофотометрия звезд в диапазоне λλ550-900нм / Киев: Наукова думка - 1983 - 312с.

[5] N.S. Komarov M.G., Arkhipov N. Yu., Basak S.I., Belik,A.G., Cherkass, R.I., Chuprina, E.A. Depenchuk, A.V. Dragunova, I.F. Dulapchi, T.I. Gorbaneva, V.F. Karamysh, L.E. Kantsen, S.A. Korotin, V.V. Kovtyukh, L.F. Orlova, V.D. Motrich, A.F. Pereverzentsev, T.V. Shevchuk, N.N. Zakozhurnikova // The New Spectrophotometric Star Catalogue / Odessa Astronomical Publication - Vol. 11 - 1998 - P. 3 – 48.

[6] Омаров С.З., Гаджиев М. С., Гольдберг Е. П., Омарова Г. Р., Шестопалов Д.И., Шустарев П.Н. // Распределение энергии в спектрах 425 ярких звезд / Циркуляр Шамахинской АО им. Н. Туси НАН Азербайджана. № 104. 2002. С. 3-174.

[7] Hamuy Mario, Walker A. R., Suntzeff N. B., Gigoux P., Heathcote S. R. and Philips M. M. // Southern spectrophotometric standards. I / Publications of the Astronjvical Society of the Pacific - 1992 - V. 104. - P. 533 - 552.

[8] Hamuy Mario, Suntzeff N. B., Heathcote S.R.., Walker A.R., Gigoux P., Philips M. M. // Southern spectrophotometric standards. II. / Publications of the Astronomical Society of the Pacific - 1994 - V. 106. - P.566 - 589.

[9] Borisov I. N., Glushneva I. N., Shenavrin V. I. // Spectrophotometric standards of 7^m-8^m: suplement 1 / Astrononical and Astrophysical Transactions - 1998. - V. 17. - P. 309-320.

[10] Терещенко В. М. Экваториальные спектрофотометрические стандарты промежуточного блеска //Астрономический журнал. - 2002. - Т. 79. - № 3. - С. 249 – 255.

[11] Терещенко В.М., Шамро А.В. // Спектрограф для абсолютных измерений. Схема и конструкция оптико-механического блока / Известия НАН РК. – 2017 - № 4 – С. 152 - 159.

[12] Миронов А.В. // Основы астрофотометрии / М. - Физматлит - 2008 - 260с.

[13] Кондратьева Л.Н., Рспаев Ф. К., Аймуратов Е. К. //Результаты спектральных и фотометрическеих наблюдений RS Ophiuchi / Известия НАН РК - 2015. - №5. - с. 38 - 43.

[14] Гайсина В.Н., Денисюк Э.К., Валиуллин Р.Р. //Запрещенные эмиссионные лигнии в спектрах Сейфертовских галактик / Известия НАН РК, 2015. - №5.- с. 12-21

[15] Терещенко В.М. Спектральный коэффициент прозрачности в районе Астрофизического института в 1970-1971гг // Вестник АН Каз. ССР, 1972, - № 3 (324) - с.73 - 76.

УДК 524.31

В. М. Терещенко

«В.Г. Фесенков атындағы Астрофизика институты» ЕЖШС, Алматы, Қазақстан

СПЕКТРОФОТОМЕТРЛІК СТАНДАРТТАР 8^m-10^m . 1. АППАРАТУРА, ӘДІСТЕМЕ ЖӘНЕ АЛҒАШҚЫ НӘТИЖЕЛЕР

Аннотация. 8^m-10^m спектрофотометрлік стандарттардың жүйесін құру міндеттерінің негіздемесі келтірілді. Осы жарқылдың стандарты ірі телескоптарда спектрлік бақылаулардың калибровкасы үшін қажетті. Спектрофотометрлік стандарттардың және алғашқы стандарттардың жұлдыз-кандидаттардың таңдамалары жасалды. Стандарттардың кандидаттары ретінде ±3˚бейімделумен экваторлық аймақта орналасқан А және В спектрлік топтарының жұлдыздары таңдалды. Пайдаланылатын аппаратураның қысқаша сипаттамасы – жаңа ЗБА-спектрограф. Бір уақытта коллиматор және камера болып қызмет атқаратын ойық тороидты тор спектрографтың ыдыратқыш элементі болып табылады. Спектрограф саңылаусыз режимде жұмыс істейді. Сәулелену қабылдағыш ретінде ЗБП-камера ATIC - 490EX пайдаланылады. Жаңа спектрограф энергияның таралуын зерттеуге мүмкіндік береді. Ертеректегі спектрометрмен жұлдыздар спектрлерінде біраз әлсіз. Бақылаулар АЗТ-8 және Цейсс-600 телескоптарында орындалды. Бақылаудың дифференциалдық әдісі пайдаланылды. Спектрограммалармен ЗБА-кадрлар өңдеу процесстері нақтылап суреттелген. Энергияның таралуы 340 - 660нм спектрлік аймақтарда зерттеледі, алынған мәліметтердің спектрлік рұқсаты 5нм құрайды, салыстырмалы с.к.о. - от 3 ден 6% дейін. Стандарттардың екі кандидаттарының спектрлерінде энергияның нақты таралуы ұсынылды.

Түйін сөздер: жұлдыздар, спектрофотометрлік стандарттар, ЗБА-спектрограф, бақылау әдістері.

Информация об авторе:

Терещенко В.М. - кандидат физ.-мат. наук, в.н.с. Астрофизического института им. В.Г.Фесенкова; volter2307@mail.ru

N E W S
OF THE NATIONAL ACADEMY OF SCIENCES OF THE REPUBLIC OF KAZAKHSTAN
PHYSICO-MATHEMATICAL SERIES
ISSN 1991-346X
Volume 4, Number 320 (2018), 79 – 84

A.F. Yakovets, G.I. Gordienko, B.T. Zhumabayev, Yu.G. Litvinov,

«Institute of Ionosphere» JSC «National Center of Space Research and Technology», Almaty
artyak40@mail.ru

COMPARISON OF ALTITUDE PROFILES OF AMPLITUDE OF TWO TYPES OF *F*2- LAYER IONOSPHERIC DISTURBANCES

Abstract. Based on the data of vertical sounding of the ionosphere in Almaty in 2000-2012, the altitude profiles of amplitude of nighttime enhancements in the electron concentration of the *F*2 layer were obtained and compared with the altitude profiles of amplitudes of large-scale traveling ionospheric disturbances (LSTIDs). A scattering diagram is calculated between the height (h_{Am}) corresponding to the amplitude maximum and the height of the maximum of the (h_mF2) layer. Similar diagrams are calculated for the amplitudes of the LSTIDs. It is shown that h_{Am} is always below h_mF2, between h_{Am} and h_mF2 there is a good correlation relation, and the difference between h_{Am} and h_mF2 increases linearly with increasing h_mF2. If for h_mF2 = 280 km the difference is ~ 38 km, then for h_mF2 = 380 km the difference is ~ 54 km. A similar behavior of the altitude corresponding to the maximum amplitudes was also obtained for plasma disturbances formed by the LSTIDs, with the average distance between altitudes varying from ~ 45 km for h_mF2 = 280 km to ~ 80 km for h_mF2 = 380 km.

Key words: ionosphere, vertical sounding, electron concentration in the *F*2 layer maximum.

УДК 550.383

А.Ф. Яковец, Г.И. Гордиенко, Б.Т. Жумабаев, Ю.Г. Литвинов

ДТОО «Институт ионосферы» АО «НЦКИТ», Алматы,

СРАВНЕНИЕ ВЫСОТНЫХ ПРОФИЛЕЙ АМПЛИТУД ДВУХ ТИПОВ ВОЗМУЩЕНИЙ *F*2- СЛОЯ ИОНОСФЕРЫ

Аннотация. На основе данных вертикального зондирования ионосферы в Алматы в 2000-2012 гг получены высотные профили размаха ночных увеличений электронной концентрации *F*2-слоя, и проведено их сравнение с высотными профилями амплитуд крупномасштабных перемещающихся ионосферных возмущений (КМ ПИВ). Рассчитаны диаграммы рассеяния между высотой h_{Am}, соответствующей максимальному размаху увеличений, и высотой максимума h_mF слоя. Аналогичные диаграммы рассчитаны для амплитуд КМ ПИВ. Показано, что h_{Am} всегда находится ниже h_mF, между h_{Am} и h_mF существует хорошая корреляционная связь, а разница между h_{Am} и h_mF линейно возрастает с ростом h_mF. Если для h_mF= 280 км разница равна ~38 км, то для h_mF= 380 км разница равна ~54 км. Подобное поведение высоты, соответствующей максимальному размаху, получено также для возмущений плазмы, образованных КМ ПИВ, при этом среднее расстояние между высотами изменяется от ~45 км для h_mF = 280 км до ~80 км для h_mF = 380 км.

Ключевые слова: ионосфера, вертикальное зондирование, высотные профили в *F*2-слое.

Введение. В литературе описан обширный класс возмущений *F*2-слоя ионосферы, которые накладываются на регулярные суточные вариации электронной концентрации. Разные типы возмущений характеризуются отличающимися механизмами их генерации. Крупномасштабные перемещающиеся ионосферные возмущения (КМ ПИВ), по-видимому, являются наиболее характерными особенностями неоднородной структуры ионосферы. КМ ПИВ представляют собой

отклик ионосферы на распространение атмосферных гравитационных волн (АГВ), генерируемых в полярных районах во время геомагнитных возмущений [1] и в нижней атмосфере независимо от уровня магнитной активности [2]. Результаты теоретического и экспериментального изучения распространения АГВ в нейтральной атмосфере и их ионосферного проявления сведены в ряде обзорных работ [1, 3]. Типичные параметры КМ ПИВ представляют следующие величины: периоды занимают диапазон 40 мин – 3 ч; горизонтальные длины волн – 1000–3000 км; фазовые скорости – 400–1000 м/с.

Другой тип ионосферных возмущений представляет собой ночные увеличения электронной концентрации в максимуме *F*2-слоя ионосферы (N_mF2). Этот тип неоднородностей описан в многочисленных работах [4, 5, 6, 7, 8], в которых наряду с морфологией явления рассматривается механизм его образования, включающий: *а*) амбиполярную диффузию ионосферной плазмы; *б*) дрейф плазмы вдоль магнитных силовых линий, обусловленный меридиональным нейтральным ветром; *в*) плазменный обмен между плазмосферой и ионосферой и *г*) рекомбинацию. Анализ частоты возникновения ночных увеличений *NmF*2 по данным вертикального зондирования в Алматы за 2000–2014 гг. показал, что существует хорошо выраженная сезонная зависимость частоты возникновения увеличений [9]. Одинаковыми чертами распределений для высокой и низкой солнечной активности являются высокие вероятности формирования увеличений в зимние месяцы.

В работе [10] были получены высотные профили амплитуд КМ ПИВ, которые дают возможность ввести дополнительные параметры, характеризующие распространение возмущений. Одним из таких параметров является высота максимума амплитуды КМПИВ (h_{Am}), а также ее соотношение с высотой максимума *F*2-слоя ($h_{\mathrm{m}}F$). Целью настоящей работы явилось получение высотных профилей размаха ночных увеличений электронной концентрации *F*2-слоя, и сравнение их с высотными профилями амплитуд КМ ПИВ.

Описание аппаратуры и анализ результатов наблюдений.

Ночные наблюдения ионосферы проводятся в Институте ионосферы (Алма-Ата, 76°55' E, 43°15' N) на цифровом ионозонде, сопряженном с компьютером “Pentium-166”, который предназначен для сбора, хранения и обработки ионограмм в цифровом виде. Информация считывается с ионограмм полуавтоматическим методом. Длительность сеансов наблюдения, осуществляемых в 5-минутном режиме, в зависимости от сезона составляет 10−14 ч, 10−15 ночей каждый месяц. Первичная обработка ионограмм включает считывание значений действующих высот ($h'(t)$) отражения радиосигнала на ряде фиксированных рабочих частот зондирования и значений критической частоты (f_oF2). Ионозонд обеспечивает точность считывания $h'(t) \sim 2.5$ км и точность считывания $f_oF2 \sim 0.05$ МГц. Дальнейшая обработка включает получение из ионограмм *N(h)*-профилей, используя программу пересчета POLAN [11] действующих высот в истинные высоты. В этом методе *N(h)*-профиль аппроксимируется перекрывающимися полиномами, при этом участок профиля вблизи N_mF2 аппроксимируется параболой.

Для получения количественных оценок параметров ночных увеличений электронной концентрации слоя *F*2 строилось поведение электронной концентрации на ряде фиксированных высот (рис. 1) (расстояние между соседними высотами составляет 10 км, а нижняя кривая соответствует высоте h = 190 км). Жирной кривой представлены вариации электронной концентрации (N_mF2) в максимуме слоя. Критическая частота слоя (в МГц) связана с электронной концентрацией в максимуме слоя (N_mF2), выражаемой количеством электронов в кубическом сантиметре, соотношением $N_mF2 = 1.24 \cdot 10^4 \, (f_oF2)^2$.

На рисунке 1 представлен пример поведения параметров ночного *F*2-слоя, которое представляет последовательность первого ($t \sim$ 20:40–22:25), второго ($t \sim$ 23:10 –02:00) и третьего ($t \sim$ 03:15–04:15) увеличений. Падение электронной концентрации в начале сеанса измерения обусловлено выключением ионизирующего излучения Солнца после его захода и химическими потерями, обусловленными рекомбинацией плазмы. Быстрое увеличение электронной концентрации утром после 06:00 обусловлено восходом Солнца. Поведение электронной концентрации на ряде фиксированных высот позволяет получить высотную зависимость (профиль) размаха увеличения. На рисунке 2 представлены высотные профили размаха увеличений электронной концентрации для первого (левая панель) и второго (правая панель) увеличений и

$N(h)$-профили для начала и конца увеличений, рассчитанные из вариаций $N_e(t)$, представленных на рис. 1. В сеансе измерений, представленном на рис. 1, высота, соответствующая максимальному размаху, как для 1-го, так и для 2-го увеличения, оказалась равной 260 км. Анализ всего объема наблюдений показал, что рассмотренные на рис. 1 особенности сохраняются во время формирования увеличений и в другие даты, приходящиеся на разные сезоны и годы с разным уровнем солнечной активности.

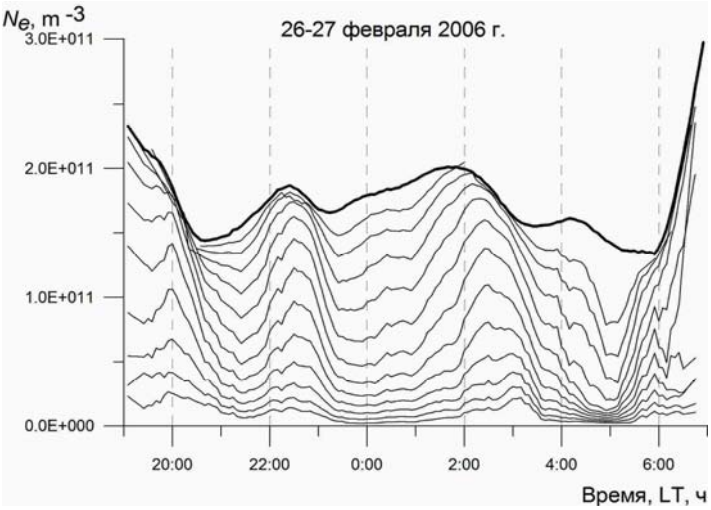

Рисунок 1 – Поведение электронной концентрации *F*2-слоя на ряде фиксированных высот при формировании ночных увеличений электронной концентрации.

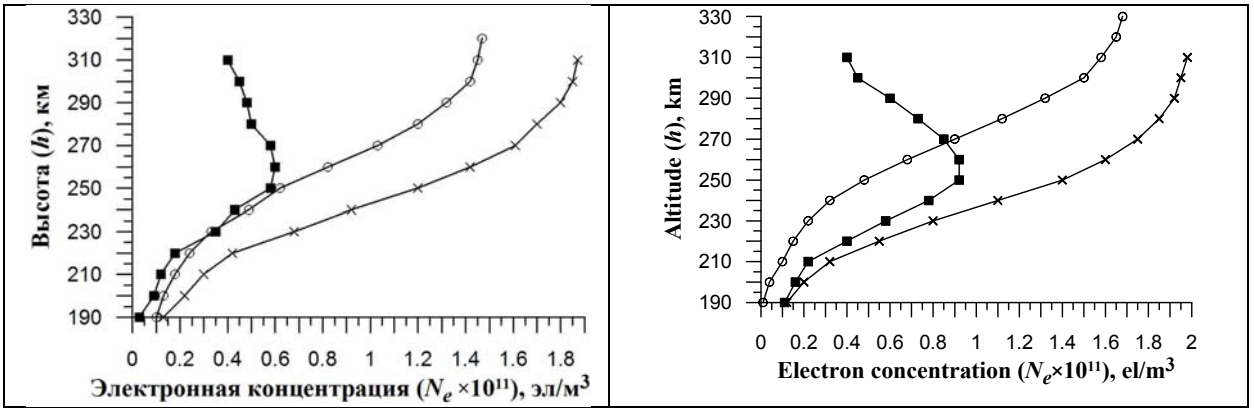

Рисунок 2 – Высотные профили размаха увеличений электронной концентрации (■) и $N(h)$-профили для начала (о) и конца (х) увеличений, имевших место 26-27 февраля 2006 г. *а* – первое увеличение ($t_{нач}$ ~ 20:40, $t_{кон}$ ~ 22:25); *б* – второе увеличение ($t_{нач}$ ~ 23:10, $t_{кон}$ ~ 02:00).

Для исследования высотных профилей амплитуд КМПИВ за период 2000– 2007 гг. были выбраны сеансы наблюдений, во время которых были зарегистрированы возмущения с относительной амплитудой (δ_h), превышающей 25%, на высоте, соответствующей A_m. Здесь $\delta_h = A(h)/N(h)$, где $A(h)$ – абсолютная амплитуда волны на высоте h и $N(h)$ – величина невозмущенной электронной концентрации на данной высоте. Выбор сеансов наблюдений, в течение которых были зарегистрированы КМ ПИВ с большими абсолютными и относительными значениями амплитуд, обеспечивал высокую точность построения высотных профилей амплитуд даже вблизи высот основания слоя, которые характеризуются малыми значениями $A(h)$ и $N(h)$. Всего таких сеансов оказалось 63. На рисунке 3 (левая панель) представлен пример вариаций электронной концентрации $N_h(t)$ для ночи 30 – 31 августа 2004 г. на серии высот с расстоянием между

соседними высотами 10 км. Нижняя кривая соответствует высоте основания слоя (h = 190 км). Верхняя (жирная) кривая соответствует вариациям $N_mF(t)$ в максимуме слоя h_mF. На рисунке представлены сглаженные вариации плотности с отфильтрованными высокочастотными флуктуациями.

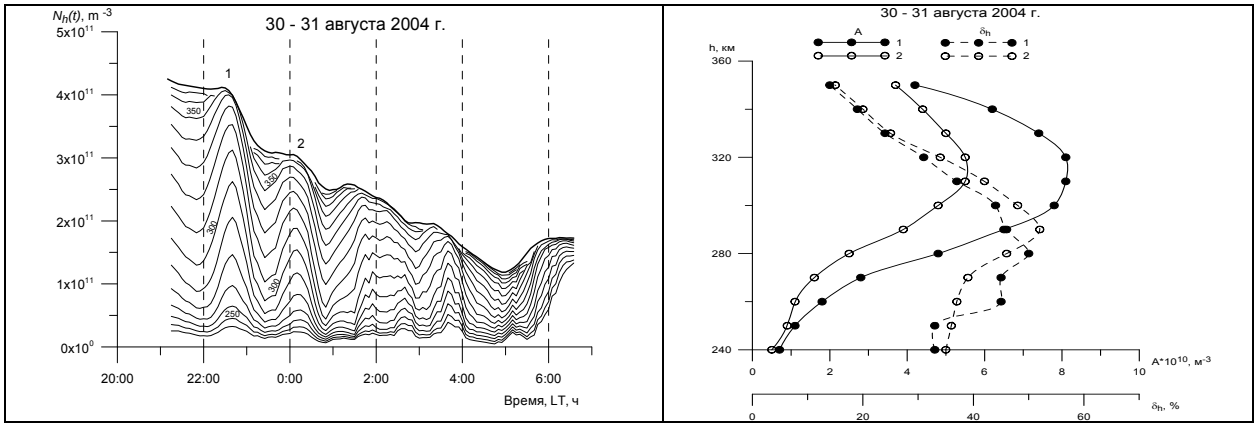

Рисунок 3 – Вариации электронной концентрации $N_h(t)$ для ночи 30 – 31 августа 2004 г. на серии высот с расстоянием между соседними высотами 10 км (левая панель) и соответствующие высотные профили абсолютных (непрерывные линии) и относительных (штриховые линии) амплитуд возмущений *1* (точки) и *2* (кружки) для КМ ПИВ. Репродукция рис. 1 и 2 из статьи [10]

Для удаления из первичных данных $N_h(t)$ высокочастотных составляющих как ионосферного происхождения, так и вызванных шумом, возникающим в процессе обработки данных, осуществлялась низкочастотная фильтрация рядов с применением скользящего окна длительностью T = 30 мин. Вариации электронной концентрации, представленные на рисунке, демонстрируют особенность, характерную для большинства сеансов, в которых наблюдались КМ ПИВ. Особенность заключается в том, что КМ ПИВ в вариациях $N_mF(t)$ проявляются значительно слабее, чем в вариациях $N_h(t)$ на фиксированных высотах, расположенных ниже высоты максимума слоя. Причины такой высотной зависимости реакции ионосферы на прохождение АГВ рассмотрены в работе [12]. На рисунке 3 (правая панель) представлены высотные профили абсолютных и относительных амплитуд возмущений 1, 2, рассчитанные из вариаций $N_h(t)$. Высотные профили амплитуд возмущений строились для каждой периодической волны, зафиксированной в течение сеанса измерений. На рисунке 3 (левая панель) отчетливо видны по две волны, которые обозначены цифрами 1 и 2. В этом сеансе наблюдений высоты, соответствующие максимальной абсолютной амплитуде, как для волны 1, так и для волны 2, составляли 310 – 320 км, при этом средняя высота максимума слоя составляла 370 км. Видно, что профили для волн 1, 2 различаются как для относительных, так и абсолютных амплитуд. Общим свойством для волн, представленных на рис. 3 и для всех остальных проанализированных сеансов, является то, что высоты, соответствующие максимальным значениям абсолютных амплитуд**,** превышают высоты, соответствующие максимальным значениям относительных амплитуд**.** При этом интервал изменения высот максимума профилей для всего массива анализируемых сеансов весьма широк.

Для количественного анализа параметров ночных увеличений нами были отобраны за период 2001−2012 гг. 20 ночей, характеризующихся низкой магнитной активностью (Dst> −50 нТл) и выраженными проявлениями ночных увеличений N_e. Рисунок 4 (левая панель) представляет диаграмму рассеяния между высотой h_{Am}, соответствующей максимальному размаху увеличений, и высотой максимума h_mF слоя. Интервал высот, на которых наблюдались максимальные размахи для всего массива анализируемых сеансов, оказался весьма широк. Рассчитанная методом наименьших квадратов линия регрессии изображена сплошной линией. Выражение для этой линии и значение коэффициента корреляции r=0.9 представлены в верхней части рисунка.

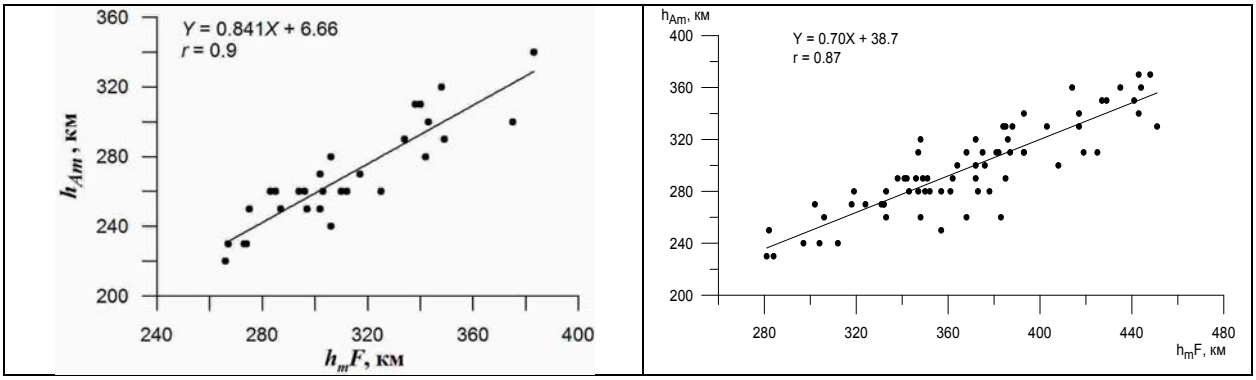

Рисунок 4 – Диаграмма рассеяния между высотами h_{Am} и h_mF, полученная по всему массиву анализируемых данных (20 ночей) для ночных увеличений (левая панель) и КМПИВ (правая панель).

Из рисунка следует, что разница между h_{Am} и h_mF линейно возрастает с ростом h_mF. Если для h_mF= 280 км разница равна ~38 км, то для h_mF= 380 км разница равна ~54 км. Подобное поведение высоты, соответствующей максимальному размаху, получено также для возмущений плазмы, образованных КМ ПИВ (правая панель). Видно, что h_{Am} всегда находится ниже h_mF, между h_{Am} и h_mF существует хорошая корреляционная связь, среднее расстояние между высотами изменяется от ~45 км для h_mF = 280 км до ~80 км для h_mF = 380 км при низкой магнитной активности. Такое поведение высотного профиля амплитуд КМ ПИВ было интерпретировано в работе [10] на основе пространственно-временной картины их распространения, представляющей периодические осцилляции термосферного меридионального ветра, которые приводят к периодическим колебаниям высоты F2-слоя. Поэтому высотный профиль амплитуд возмущений в основном определяется формой $N(h)$-профиля слоя.

Выводы. Проведено сравнение высотных зависимостей (профилей) размаха ночных увеличений электронной концентрации F2- слоя и амплитуд крупномасштабных перемещающихся ионосферных возмущений. Найдены количественные соотношения между параметрами вариаций размаха увеличений N_mF2 в максимуме слоя и на высоте, характеризующейся максимальной скоростью нарастания концентрации. Показано, что высотные профили размаха увеличения N_mF2 и амплитуд КМПИВ обладают одинаковыми свойствами: высота максимума профилей лежит ниже высоты максимума слоя, при этом расстояние между высотами максимумов растет с увеличением h_mF.

Работа выполнена по РБП-008 «Развитие космических технологий мониторинга и прогнозирования природных ресурсов, техногенных изменений окружающей среды, создание космической техники и наземной космической инфраструктуры, исследования объектов дальнего и ближнего космоса» в рамках темы «Создание системы диагностики и прогноза космической погоды для анализа и прогнозирования условий функционирования космических аппаратов, систем навигации и связи (2018-2020гг.»), регистрационный номер (РН) 0118РК00800.

ЛИТЕРАТУРА

[1] *Hunsucker R.D.* Atmospheric gravity waves generated in the high latitude ionosphere: A review // Rev. Geophys. V. 20. N 2. P. 293–315. 1982.

[2] *Vadas S.L., Liu H.* Generation of large scale gravity waves and neutral winds in the thermosphere from the dissipation of convectively generated gravity waves // J. Geophys. Res. V. 114. N A10310, doi:10.1029/ 2009JA014108. 2009.

[3] *Hocke K., Schlegel K.* A review of atmospheric gravity waves and traveling ionospheric disturbances: 1982–1995 // Ann. Geophysicae. V. 14. N 9. P. 917–940. 1996.

[4] *Farelo A.F., Herrais M., Mikhailov A.V.* Global morphology of nighttime *NmF*2 enhancements // Ann. Geophysicae. V. 20. N 11. P. 1795–1806. 2002.

[5] *Bailey G.J., Sellek R., Balan N.* The effect of interhemispheric coupling on nighttime enhancement in ionospheric total electron content winter at solar minimum // Ann. Geophysicae. V. 9. N 9. P. 738–747. 1991.

[6] *Mikhailov A.V., Leschinskaya T.Yu., Förster M.* Morphology of *NmF*2 nighttime increases in the Eurasian sector // Ann. Geophysicae. V. 18. N 6. P. 618–628. 2000a.

[7] *Mikhailov A.V., Förster M., Leschinskaya T.Yu.* On the mechanism of the postmidnight winter *NmF*2 enhancements: dependence on solar activity // Ann. Geophysicae. V. 18. N 11. P. 1422–1434. 2000b.

[8] *Pavlov A.V., Pavlova N.M.* Mechanism of the postmidnight winter nighttime enhancement in the *NmF*2 over Millstone Hill during 14–17 January 1986 // J. Atmos. Solar-Terr. Phys. V. 67. N 4. P. 381–395. 2005.

[9] *Yakovets A.F., Vodyannikov V.V., Gordienko G.I., and Yu.G. Litvinov*. Some Features of Nighttime Enhancements in the Electron Concentration in the F2-Layer Maximum of the Midlatitude Ionosphere // Geomagnetism and Aeronomy. 2014. V. 54. No.6, pp. 791-801.

[10] *Yakovets A.F., Vodyannikov V.V., Gordienko G.I., and Yu.G. Litvinov*. Height Profiles of the Amplitudes of Large Scale Traveling Ionospheric Disturbances. Geomagnetism and Aeronomy, 2013, Vol. 53, No. 5, pp. 655–662.

[11] *Titheridge J.E.* Ionogram analysis with the generalized program POLAN. Boulder. CO USA: National Data Center. 189 p. 1985.

[12] *Yakovets A.F., Vodyannikov V.V., Gordienko G.I., Ashkaliev Ya. F., Litvinov Yu. G., and S. B. Akasov*. Response of the Nighttime Midlatitude Ionosphere to the Passage of an Atmospheric Gravity Wave. Geomagnetism and Aeronomy, 2008, Vol. 48, No. 4, pp. 511–517.

УДК 550.383

А.Ф. Яковец, Г.И. Гордиенко, Б.Т. Жумабаев, Ю.Г. Литвинов

Ионосфера институты, Ұлттық ғарыштық зерттеулер мен технологиялар орталығы,
Қазақстан Республикасы, Алматы, Каменское плато

ИОНОСФЕРАНЫҢ F2-ҚАБАТЫНЫҢ ҰЙЫТҚУЛАРЫНЫҢ ЕКІ ТҮРІНІҢ АМПЛИТУДАСЫНЫҢ БИІКТІК ПРОФИЛЬДЕРІН САЛЫСТЫРУ

Аннотация. Ионосфераны тігінен зондтау деректері бойынша Алматыда 2000-2012 жылдар аралығында F2-қабатының электрондардың концентрациясында түнгі уақытта артуының биік серпілу профильдері алынды, және оларды кең ауқымды қозғалмалы ионосфералық бұзылулар (КА ҚИБ) амплитудасының биіктік профильдерімен салыстыру жүргізілді. Биіктігі h_{Am} арасындағы шашырау диаграммалары, серпілудің максималды ауқымына сәйкес келетін, және h_mF-қабатының максималды биіктігі есептелген. Ұқсас диаграммалар (КА ҚИБ) амплитудалары үшін есептелген. Көрсетілгендей, h_{Am} әрқашан h_mF-ден төмен орналасады, h_{Am} және h_mF арасында жақсы корреляциялық қатынас бар, ал h_{Am} мен h_mF арасындағы айырмашылық h_mF артуымен сызықты түрде артады. Егер h_mF = 280 км үшін айырмашылық ~ 38 км болса, ал h_mF = 380 км үшін айырмашылық ~ 54 км. Биіктіктің мұндай мінез-құлқы максималды серпілуге сәйкес келеді сондай-ақ, (КА ҚИБ) құрылған плазманың бұзылуы, сонымен қатар биіктік арасындағы орташа қашықтық h_mF = 280 км-ден ~ 80 км-ге дейін h_mF = 380 км үшін 45 км-ден ауытқуы үшін алынған.

Түйін сөздер: ионосфера, тік зондтау, F2-қабатындағы биіктік профильдері

Сведения об авторах:

Яковец Артур Федорович - канд. физ.-мат. наук, СНС, Алматы, Каменское плато, Институт ионосферы, ДТОО «Институт ионосферы» АО «НЦКИТ», artyak40@mail.ru;

Гордиенко Галина Ивановна - канд. физ.-мат. наук, СНС, Алматы, Каменское плато, Институт ионосферы, ДТОО «Институт ионосферы» АО «НЦКИТ», ggordienko@mail.ru;

Жумабаев Бейбит Тенелович - канд. физ.-мат. наук, СНС, Алматы, Каменское плато, Институт ионосферы, ДТОО «Институт ионосферы» АО «НЦКИТ», beibit.zhu@mail.ru;

Литвинов Юрий Георгиевич - канд. физ.-мат. наук, Алматы, Каменское плато, Институт ионосферы, ДТОО «Институт ионосферы» АО «НЦКИТ», yurii-litvinov@mail.ru.

МАЗМҰНЫ

* * *

СОДЕРЖАНИЕ

* * *

CONTENTS

* * *

Publication Ethics and Publication Malpractice
in the journals of the National Academy of Sciences of the Republic of Kazakhstan

For information on Ethics in publishing and Ethical guidelines for journal publication see http://www.elsevier.com/publishingethics and http://www.elsevier.com/journal-authors/ethics.

Submission of an article to the National Academy of Sciences of the Republic of Kazakhstan implies that the described work has not been published previously (except in the form of an abstract or as part of a published lecture or academic thesis or as an electronic preprint, see http://www.elsevier.com/postingpolicy), that it is not under consideration for publication elsewhere, that its publication is approved by all authors and tacitly or explicitly by the responsible authorities where the work was carried out, and that, if accepted, it will not be published elsewhere in the same form, in English or in any other language, including electronically without the written consent of the copyright-holder. In particular, translations into English of papers already published in another language are not accepted.

No other forms of scientific misconduct are allowed, such as plagiarism, falsification, fraudulent data, incorrect interpretation of other works, incorrect citations, etc. The National Academy of Sciences of the Republic of Kazakhstan follows the Code of Conduct of the Committee on Publication Ethics (COPE), and follows the COPE Flowcharts for Resolving Cases of Suspected Misconduct (http://publicationethics.org/files/u2/New_Code.pdf). To verify originality, your article may be checked by the Cross Check originality detection service http://www.elsevier.com/editors/plagdetect.

The authors are obliged to participate in peer review process and be ready to provide corrections, clarifications, retractions and apologies when needed. All authors of a paper should have significantly contributed to the research.

The reviewers should provide objective judgments and should point out relevant published works which are not yet cited. Reviewed articles should be treated confidentially. The reviewers will be chosen in such a way that there is no conflict of interests with respect to the research, the authors and/or the research funders.

The editors have complete responsibility and authority to reject or accept a paper, and they will only accept a paper when reasonably certain. They will preserve anonymity of reviewers and promote publication of corrections, clarifications, retractions and apologies when needed. The acceptance of a paper automatically implies the copyright transfer to the National Academy of Sciences of the Republic of Kazakhstan.

The Editorial Board of the National Academy of Sciences of the Republic of Kazakhstan will monitor and safeguard publishing ethics.

Правила оформления статьи для публикации в журнале смотреть на сайтах:

www:nauka-nanrk.kz

http://www.physics-mathematics.kz

ISSN 2518-1726 (Online), ISSN 1991-346X (Print)

Редакторы *М. С. Ахметова, Т.А. Апендиев, Д.С. Аленов*
Верстка на компьютере *А.М. Кульгинбаевой*

Подписано в печать 08.06.2018.
Формат 60x881/8. Бумага офсетная. Печать – ризограф.
5,5 п.л. Тираж 300. Заказ 4.

Национальная академия наук РК
050010, Алматы, ул. Шевченко, 28, т. 272-13-18, 272-13-19